OAK RIDGE
NATIONAL LABORATORY
MANAGED BY UT-BATTELLE
FOR THE DEPARTMENT OF ENERGY

ORNL/TM-2001/100

Dynamic Particle Growth Testing: Phase I Studies

June 18, 2001

Prepared by
Michael Z. Hu, David W. DePaoli, and Debra T. Bostick

UT-BATTELLE
ORNL-27 (4-00)

ORNL/TM-2001/100

Chemical Technology Division

DYNAMIC PARTICLE GROWTH TESTING: PHASE I STUDIES

Michael Z. Hu
David W. DePaoli
Debra T. Bostick

June 2001

Prepared by
OAK RIDGE NATIONAL LABORATORY
Oak Ridge, Tennessee 37831-6285
managed by
UT-BATTELLE, LLC
for the
U.S. DEPARTMENT OF ENERGY
under contract DE-AC05-00OR22725

CONTENTS

LIST OF FIGURES

ACRONYMS AND NOMENCLATURE

a.u.	arbitrary units
d_H	hydrodynamic diameter
DLS	dynamic light scattering
DOE	U.S. Department of Energy
E	activation energy for aluminosilicate particle formation
ICP	inductively coupled plasma
ODU	optical density unit
ORNL	Oak Ridge National Laboratory
R	universal gas constant
RI	refractive index
SEM	scanning electron microscopy
SRS	Savannah River Site
SRTC	Savannah River Technology Center
T	temperature
t_I	induction period, defined as time of reaction when particles are first detected by DLS
TEM	transmission electron microscopy
TTP	Technical Task Plan
WSRC	Westinghouse Savannah River Company
XRD	X-ray diffraction

EXECUTIVE SUMMARY

This report presents results obtained in experimental studies aimed at assisting to develop the knowledge base needed for understanding the causes of scale formation in the 2H evaporator at the Savannah River Site (SRS) and for enabling prevention of future occurrences of evaporator scaling in U. S. Department of Energy (DOE) waste evaporators. The report covers experimental activities conducted during the first half of fiscal year 2001 related to Subtask A.4, "WSRC Evaporator Plugging," of TTP OR-16WT41 and to Phase I of Savannah River Technology Center (SRTC) Activity, "Dynamic Particle Growth Testing." This report constitutes the deliverable for milestone A.4.1-1 of TTP OR-16WT41 and for SRTC Activity ID 2HEVP2O17.

Scale formation in the evaporator system at SRS is a significant and immediate concern. The 2H high-level waste evaporator at SRS has been shut down since October 1999 because of the formation of scale deposits that contain enriched uranium. Sampling and analysis have indicated that the scale is primarily an insoluble sodium aluminosilicate. The presence of ^{235}U in the solid scale is a significant safety concern. Visual internal inspection of the evaporator pot showed a significant buildup of solids on nearly all of the exposed internal surfaces. The deposits were nonuniformly distributed in the pot, indicating that scale formation results from the interplay of heat and mass transfer with complex reaction mechanisms and kinetics.

Data are included for initial experiments aimed at engineering questions about the formation, growth, and transport of solids. The work was undertaken to investigate the dynamics of particle formation and growth in bulk solution and to obtain preliminary results relative to the dynamics and mechanisms of solid growth at surfaces. Two types of experiments were conducted: (1) dynamic-light-scattering DLS experiments and (2) surface-solids-formation tests. DLS experiments provide a means for detecting the formation and growth of particles in simulant solutions in the size range of 5 nm to 1 μm. The surface-solids-formation tests involved the deposition and growth of solids from simulant solutions onto surfaces of stainless steel foil and allowed the investigation of the effects of solution concentration, temperature, and fluid flow on the transient growth of solids on the metal surfaces.

Several sets of DLS experiments were performed. These sets are characterized by: (1) varying the temperature (40°C through 105°C) with constant aluminum and silicon concentrations; (2) varying the silicon concentration while holding the aluminum concentration constant at 80°C and at 105°C; and (3) varying the aluminum concentration while holding the silicon concentration constant 80°C and at 105°C. The results indicate that the rate of particle-forming reactions varied over a wide range, depending on the temperature and reactant concentrations. Also, the presence of seed particles was found to significantly reduce the onset time for particle growth. Extrapolating the results to the normal operating temperature of the evaporator, particle formation could be relatively rapid (less than 10 min) with significant silicon and aluminum concentrations. Under such rapid-reaction conditions, the mixing in the evaporator would be expected to play a role in the position and form of solids produced.

Results of the surface-solids-formation tests confirmed that, for the experimental conditions examined, solids can grow on steel surfaces both by direct growth at the surface and by particle deposition. Fluid flow was found to have a significant effect on the position, amount, and form of the resulting solids. It appears that more of the strongly adhered solids deposited in high-shear than in low-shear zones. In addition, experiments verified that solids can form on top of solids that had previously formed on a metal surface. Such findings indicate that it is important to further investigate (1) particle-particle and particle-surface interaction forces and (2) the effect of hydrodynamics (flow and shear) on deposition of solids. These topics will be addressed in the Phase II studies.

1. INTRODUCTION

There is clearly a great need to understand the processes of crystallization and solid scale formation that led to the shutdown of 2H evaporator operation at the Savannah River Site (SRS) and could possibly cause similar problems in the future in other evaporators. Waste streams from SRS operations that enter the evaporators generally contain alkaline, sodium nitrate/nitrite–based solutions with various changing concentrations of silicates and aluminates. It has been determined that the silicates and aluminates served as precursor reactants for forming unwanted minerals during solution evaporation, upon transport, or upon storage. Mineral forms of the Zeolite Linde A group—sodalites and cancrinite— along with gibbsite, have often been identified as contributing to deposit (scale) formation on surfaces of the 2H evaporator[1] as well as to the formation of solid plugs in the gravity drain line[2] and lift line. Meanwhile, solids (amorphous or crystalline minerals) are believed, without direct evidence, to form in the bulk solutions in the evaporator. In addition, the position of deposits in the 2H evaporator suggests that scale formation depends on the interplay of heat and mass transfer, hydrodynamics, and reaction mechanisms and kinetics.

The origin of solid scale formation on walls could be due to heterogeneous nucleation and/or to homogeneous nucleation followed by cluster/particle deposition. Preliminary laboratory tests at the Savannah River Technology Center (SRTC) with standing metal coupons seem to support the latter mechanism for initial deposition;[3] that is, the solid particles form in the bulk solution first and then deposit on the metal surfaces. Further buildup of deposits may involve both mechanisms: deposition and crystal growth. Therefore, there may be a direct linkage between the solid particle growth in bulk solution and the scale buildup on the wall surfaces. On the other hand, even if scale formation is due solely to a heterogeneous mechanism, particle growth in the bulk would still affect scale formation by consuming a portion of the scale-forming precursor materials. In either case, solid-particle-formation data must be obtained to understand the problem.

Previous and ongoing testing based on the measurement of [Al] and [Si] consumption kinetics have indicated that the formation of aluminosilicate may be rapid under evaporator conditions.[4,5] However, the kinetics of particle formation (both in bulk solution and on surfaces) has not been studied. Conditions that cause extremely rapid particle formation are of particular interest, because in that case the solids-formation reactions in the evaporator would be sensitively dependent on process conditions such as chemical composition, temperature, fluid flow, and heat transfer.

1.1 OBJECTIVE

This effort was designed to collect experimental data that provide a *direct measure* of solid-phase (particle) formation in the bulk solutions (as well as on surfaces) under various compositions and conditions of interest. This type of data is fundamentally essential and will guide the practical evaporator operation by suggesting (1) whether and (2) how rapidly the solid particles could form in the tank solution under the conditions of evaporator operation and/or feeding/storage.

1.2 ANTICIPATED BENEFITS

Results from this task, focusing on solid-phase formation studies in bulk solution, when coupled with three other complementary, parallel efforts at ORNL and SRTC (i.e., Formation Chemistry, Formation Kinetics, and Evaporator Scale Dynamics), will help us to

(1) understand the dynamic particle growth in bulk solution (in the evaporator or under feed-tank conditions),
(2) probe the mechanisms of deposit (scale) formation, and
(3) clarify the nature of the solids.

2. EXPERIMENTAL APPROACHES AND PROCEDURES

2.1 APPROACHES TO STUDYING SOLID FORMATION IN SOLUTIONS

2.1.1 Dynamic Light Scattering

Dynamic light scattering (DLS) is a powerful technique to monitor the dynamics of solid-phase formation in bulk solutions. DLS instruments are commercially available for determination of particle sizes ranging from 5 to 1000 nm. In these studies, a specially constructed, *real-time* dynamic-light-scattering setup at ORNL (see Fig. 2.1) was used to study the solid particle evolution and growth in real time. This setup utilizes the same principles as commercial instruments, and it is thermostatically controlled to allow monitoring of in-situ particle growth processes at temperature. A detailed description of the equipment is given in a recently published paper.[6] Briefly, a quiescent reaction solution is placed in a thermally controlled cell (ranging from room temperature up to 130°C), allowing particle growth to be observed in situ while the precursor solution is held at the desired temperature. A 10-mW He-Ne laser (632.8 nm) generates a beam that is directed through the liquid sample. Detection of light scattered at 90° provides information on the Brownian motion of the nanoparticles in the liquid, which allows a calculation of the average particle size by applying the Stokes-Einstein equation. The sensitivity of DLS depends not only on the number of particles, but also on the particle size, refractive index, particle shape, aggregation state, etc. Typically, DLS can detect particles as small as 5 nm when the sample generates a scattering intensity as small as 3000–5000 counts per second, and for monodispersed particle samples, the average relative error is within 5%.

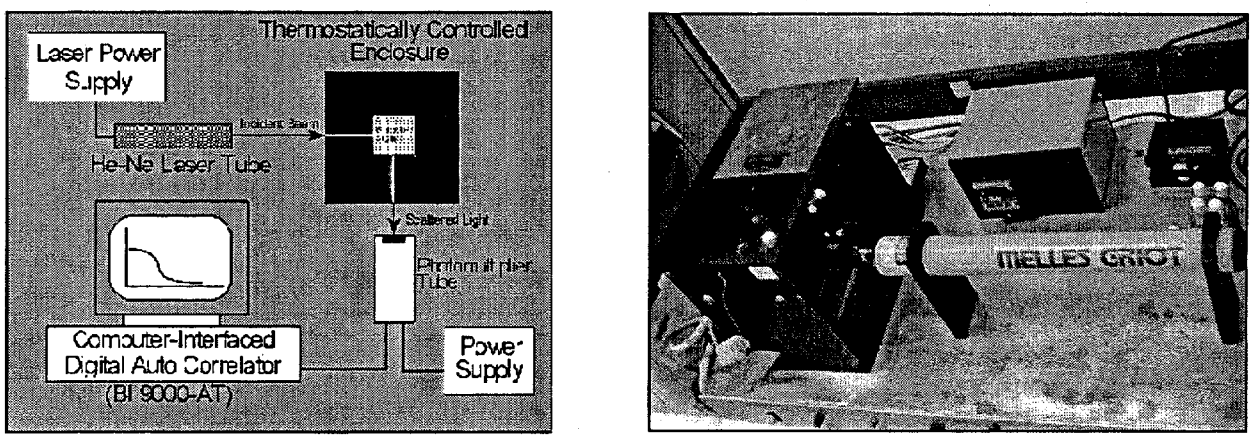

Fig. 2.1. DLS setup at ORNL for real-time monitoring of particle formation and growth.

Figure 2.2 shows illustrative growth curves (typically from 10 nm to 1 μm in hydrodynamic diameter) monitored by real-time DLS. Depending on the growth mechanisms, the particle growth shape will change. If the dispersed particles form first and then aggregate, an S-J type of growth curve is observed. If the solid phase in bulk solution is formed through gelation, usually a J-shaped growth curve is observed.[6,7] The minimum information from this kind of measurement is the determination of induction period, t_I, the time required to nucleate a solid phase of greater than a few nanometers in dimension. For a relatively dilute system, the complete particle-growth kinetics could be monitored.

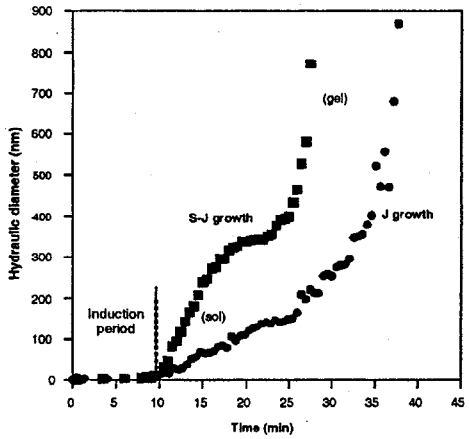

Fig. 2.2. Example of growth curves obtained by real-time DLS.

In comparison with other experimental methods for particle size determination, such as sedimentation, scanning electron microscopy (SEM), and transmission electron microscopy (TEM), DLS has several advantages:

(1) DLS measurements can be made while nanoclusters evolve and nanoparticles form in situ. Other techniques (e.g., TEM) require solutions to be quenched, diluted, etc., introducing uncertainties as to whether the results apply to actual synthesis conditions.
(2) DLS autocorrelation function curves can be accumulated quickly enough (periods as short as 10 s) to track the kinetics of particle growth over the time scales of a typical particle synthesis.
(3) DLS is sensitive to the evolution and size variation of nanosized solid particles (either amorphous or crystal particles).
(4) In addition to allowing a characteristic nanoparticle size to be obtained, over certain concentration ranges DLS can also provide a value of particle concentration from the intensity of scattered light.

A scoping study was conducted initially to ensure that the existing DLS system could be appropriately modified and thus could be used to collect particle dynamic data. Special attention was paid to the following aspects:

- *Materials compatibility.* Selection of cells compatible with the high alkalinity of solutions. Quartz, polycarbonate, and polystyrene cuvette cells were tested for suitability for in situ monitoring.
- *Multiple scattering effects.* The testing simulant solutions are highly concentrated electrolyte solutions. Multiple scattering effects due to the high concentration of solid particles formed may not allow accurate determination of particle sizes and data of size vs time for all growth ranges.

2.1.2 Solid Particle Analysis

DLS does not directly distinguish between individual "primary" colloid particles and similar-sized clusters of particles (or crystals). In aged solutions, an apparent increase in the size of the particles could be attributed either to growth or to aggregation of primary particles. This can be addressed experimentally by analysis of extracted solid-particle samples with complementary analytical tools such as SEM and powder X-ray diffraction (XRD) (Fig. 2.3). SEM allows us to see the size as well as the morphology of solid particles. XRD identifies the crystalline phases of solid particle samples, provides an understanding of the phase transformation during the dynamic particle formation, and permits us to determine the size of crystallites (if any).

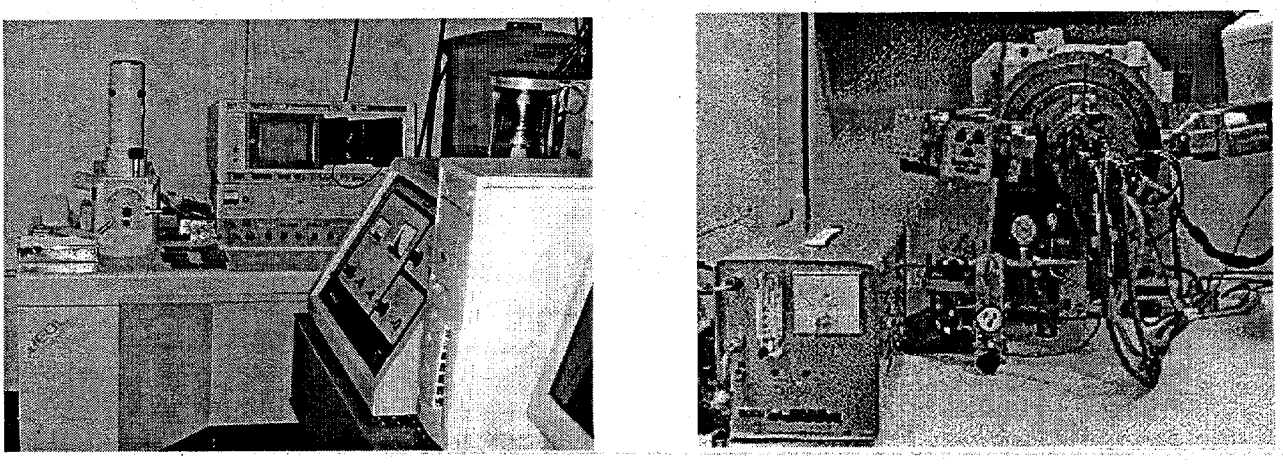

Fig. 2.3. SEM (left) **and in situ XRD** (right) **for characterization of particle solids.**

2.2 APPROACH TO STUDYING "SURFACE SOLID" FORMATION

While the DLS technique is useful for monitoring solids formation in bulk solutions, an additional method is needed to study the formation of solids on surfaces. In the "surface solid" formation tests, horizontally positioned 304 stainless steel (304SS) foils were used to probe such surface solid formation (via either growth or deposition).

The 304SS foils were held horizontally by a Teflon support and then submerged in reactive solutions in capped Teflon containers (Fig. 2.4). By SEM examination of the solid on the top side of a foil, we obtained information on the morphology and the size of bulk particles settled from solution, while the solid layer at the bottom side of the foil provided information on "surface particle" growth on the stainless steel surfaces.

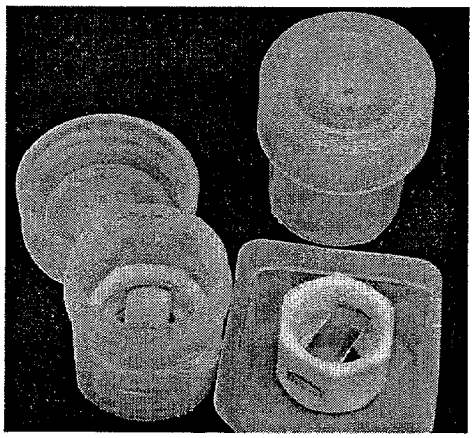

Fig. 2.4. Setup for "surface solid" formation tests.

The surface solids formed under various controlled conditions (varying concentration, temperature, reaction time, and flow) were studied by visual inspection and by SEM examination of deposited/grown solid material. The purpose of the "surface-solid-formation" studies was to understand the mechanisms of solid formation on stainless steel surfaces.

2.3 EXPERIMENTAL PROCEDURES

The compositions, conditions, and procedures for the preparation of the simulant solutions were based on information provided by W. R. Wilmarth and L. O. Dworjanyn at SRTC. Simulant solutions were prepared in two parts, based on the procedures provided by SRTC (see Appendix A for formulation of Solutions A, 2A, and B as well as Solutions D, 2D, and E), with silicate in one and aluminate in the other. Frit 200 dissolved in sodium hydroxide was used as the silicon source and aluminum nitrate as the aluminum source.

Generic simulant solutions at various [Si], [Al], and ratios of aluminum to silicon were used. Temperatures of solutions ranged from 40°C, representative of the feed tank, to near the boiling point of the solutions, ~110°C. See Appendix B for details of the boiling-point determination of simulant solutions. Appendix D shows measurements of viscosities and refractive index values for various solutions; these values are used for DLS data processing. During the course of the reaction and particle-growth processes, the viscosities of the solutions change significantly, while the refractive indexes generally does not. For the convenience of data processing, we chose an averaged viscosity for particle-size calculations for each solution composition.

2.3.1 Dynamic-Light-Scattering Experiments

The DLS method was used to obtain size-vs-time and intensity-vs-time data, as well as to determine the induction period for particle formation. Three sets of experiments, as shown in Table 2.1, were designed to study the effects of temperature, [Si], and [Al] on the bulk particle growth dynamics (i.e., induction period). Specific solution compositions can be found in Appendix A.

Two simulant aliquots were heated in separate containers in a temperature-controlled water bath until they came to the desired temperature, and the solutions were then mixed in the preheated DLS cell at the start of the test. For temperatures up to 80°C, polystyrene cuvettes having a 1-cm square cross section were used as DLS cells; for temperatures above 80°C, translucent Teflon test tubes with caps were used. Particle formation dynamics were monitored in situ. The data acquisition and sampling frequency depended on temperature, partly based on the experience of others and partly by initial trials.[2] At the higher temperatures, less than 8 h was necessary for completion of the reactions, while 2 days or more was required for tests at the lowest

temperatures/concentrations. Complementarily, for representative samples collected at different times and experimental conditions, SEM was used to examine the solid-particle morphology and XRD was used to determine the crystalline phases present.

Table 2.1. Experimental conditions for DLS studies

Experiment	Fixed parameters	Variables studied
DLS Set 1	[Si] = 0.1 *M*; [Al] = 0.133 *M*	Temperature: 40, 50, 60, 70, 80, 107°C
DLS Set 2	80 and 105°C; [Al] = 0.133 *M*	[Si]: 0.004, 0.01, 0.025, 0.05, 0.075, 0.1, 0.133, 0.15 *M*
DLS Set 3	80 and 105°C; [Si] = 0.05 *M*	[Al]: 0.03, 0.04, 0.05, 0.1, 0.15, 0.2, 0.25, 0.3 *M*

2.3.2 Surface-Solid-Formation Tests with Stainless Steel Foils

A series of tests was conducted in which cleaned stainless steel foils were placed into batches of simulant solutions at a given temperature for specified periods of time. Photographs and SEM images of the foil samples were taken and examined to investigate the effects of reactant concentration, reaction time, fluid flow, and nature of the substrate surface on the formation of surface solids.

2.3.2.1 Scoping Test

A scoping test was conducted to investigate the formation of solids on horizontal and vertical stainless steel surfaces in various solutions at 80°C. These tests were conducted by cutting 304SS foil samples obtained from SRTC into small (approximately 1-cm-wide) strips, cleaning them, folding them with a 90° bend, and placing them vertically in quiescent solution in polystyrene test tubes in an oven for 41 h. The strips were cleaned by using the following steps:

(1) sonication for 10 min in 5% Micro 90 cleaner in distilled water at room temperature,
(2) rinsing with distilled water,
(3) sonication for 5 min in 4–6 *M* NaOH,
(4) rinsing with deionized water,
(5) soaking in 4–6 *M* NaOH in a Teflon vessel at 80°C in an oven for at least a few hours, and
(6) draining out the NaOH solution before submerging the foils into the test solution.

The four solutions tested were distilled water, 4 *M* NaOH, solution 2A (no silicon present), and solution 2A + B for the reactive mixture of 0.1 *M* Si–0.133 *M* Al overall.

2.3.2.2 Horizontal Foil Experiments

The foil strips were held horizontally in solution by Teflon supports fabricated from tubing fittings (see Fig. 2.4). The foils were positioned horizontally, with one side facing up and the other side facing down, in 10-mL Teflon containers with seal-tight screw caps. The foil and Teflon internals of the containers were prepared for the experiments by sonication in 5% Micro 90 cleaner followed by rinsing with distilled water, then exposure to caustic solution at temperature for several hours followed by rinsing with heated deionized water. After the containers were prepared, preheated reactive solutions were mixed, and 9-mL aliquots of the mixture were added to each container. The containers were sealed and held quiescent at temperature for a set period of time. For sampling, containers were removed from heat, the solutions were gently poured off into polystyrene test tubes that were promptly quenched in cold water, and the foil supports were gently dipped into distilled water several times, followed by similar rinsing in deionized water. The upper and lower surfaces of the foil were examined using SEM. Several tests were conducted, as described in the paragraphs that follow.

Effect of [Si] on surface solid formation. Four nitrate/nitrite-containing solutions having an initial NaOH concentration of 4 *M* and containing different silicon concentrations were prepared:

(a) 0.0 *M* Si–0.136 *M* Al
(b) 0.05 *M* Si–0.133 *M* Al
(c) 0.133 *M* Si–0.133 *M* Al
(d) 0.15 *M* Si–0.133 *M* Al

These containers were heated in an oven at 80°C for 64 h.

Effects of reaction time and temperature on surface solid formation. Several sets of experiments were conducted at 80°C and 100°C using 0.133 *M* Si–0.133 *M* Al (reactive mix in 4 *M* NaOH plus NO_3^- and NO_2^-) to investigate the effects of reaction time and temperature on surface solid formation.

Effect of fluid flow on surface solid formation. A test similar to the 80°C test described above was conducted using 0.133 *M* Si–0.133 *M* Al (reactive mix in 4 *M* NaOH plus NO_3^- and NO_2^-) to determine if fluid flow could have a significant effect on solids formation. In this test, a small magnetic stir bar was placed in the bottom of each Teflon container, and the sealed containers were positioned in a water-filled beaker placed on top of a heated magnetic stirrer. The rotational speed of the stirrer was measured to be approximately 850 rpm. This moderate rate created significant fluid motion but did not cause the formation of a vortex that would pull air from the headspace into the solution when the holder and foil were in position.

Effect of substrate surface on surface solid formation. Because the tests described above were conducted batchwise with finite volumes of reactive solution, they did not allow determination of the capability of solids to form on top of a previously deposited solid layer. To verify that solids can continue to form on top of an existing aluminosilicate layer as well as on a metal surface, an additional test was conducted at 100°C in which foils were contacted with two batches of reactive solution. This experiment was conducted by first depositing a layer of aluminosilicate by holding foil samples overnight in five containers containing 0.1 *M* Si–0.133 *M* Al in 6 *M* Na^+ at 100°C. One foil sample was collected as a "control" to characterize the initial film, while the remaining four foil samples were placed again in new 9-mL batches of solution (0.133 *M* Si–0.133 *M* Al in 6 *M* Na^+) in separate vessels for a second deposition. These containers were held at 100°C, and foil samples were removed from solution after 36, 72, and 150 min, and after 2 days.

3. RESULTS AND DISCUSSION

Clarification of terminology is needed to describe the aluminosilicate solids accumulated on the internal surfaces of the evaporator. Formation of these solids (generally called *solid deposits* or *solid scale* on walls) could be due to (a) *deposition* of particles from bulk solution or (b) surface (heterogeneous) *growth*. Here, particle *deposition* refers to the transport (via settling or flow) and attachment of particles from bulk solution onto surfaces (stainless steel, solid, or particle surface), while *growth* refers to the nucleation and growth of particles directly on the metal surface or to the growth of deposited particles. Such growth consumes the soluble precursor species available in bulk solution. *Primary particles* (or *particles* or *colloids*) refer to those individual spherical polycrystalline particles or single-crystal particles fully dispersed in solution. *Bulk solids* are referred to as *aggregated particles* (i.e., particles that are fused/connected to each other). The *attached particles* could be redispersed again into solution. Further growth of attached particles causes the fusion/connection between particles. *Fused particles* are "glued" by their own material and cannot be redispersed in solution except when a crushing force is applied to break the connecting materials. In summary, all these various types of solid particles (i.e., surface-grown particles, primary particles, attached particles, and fused particles) were observed in this study during solid aluminosilicate formation in bulk solution or on the surface. Solids on the wall were either "deposited" or "surface grown" in nature.

The results summarized in the subsections that follow were used not only to study the dynamics of bulk solid formation but also to understand the mechanisms of solid formation on tank walls or pipeline inner walls.

3.1 MATERIALS COMPATIBILITY OF DLS CELLS AND CONTAINERS FOR REACTIONS

The solutions that simulate Savannah River 2H evaporator liquid wastes are highly caustic and thus are incompatible with regular laboratory glassware and conventional optical cells for DLS studies. We started with quartz cuvette cells that are typically used for DLS. Various solutions were added in the quartz cuvettes that were then heated to 80°C and monitored by real-time DLS:

(1) silicon-containing frit Solution B (0.2 *M* Si; 6.00 *M* NaOH),
(2) aluminum-containing Solution A (0.133 *M* aluminum nitrate; 4.00 *M* NaOH; 1.00 *M* $NaNO_3$; 1.00 *M* $NaNO_2$), and
(3) mixed A and B solution containing 0.004 *M* Si, 0.133 *M* Al, and 4 *M* OH^-.

The silicon-containing Solution B prepared by dissolving Frit 200 remained clear at the testing temperature for more than 2 days (see Fig. 3.1; no colloidal particles were observed because DLS did not pick up any scattering signals). However, heating the aluminum-containing Solution A resulted in the formation of a white solid coating on the inner walls of the cuvette cell (see Fig. 3.2), while the bulk solution was clear at the end of the experiment. It is important to observe that the DLS captured an intermediate colloid formation process in the bulk solution (see Fig. 3.3, the peak evolution). The colloidal particles formed during the process were eventually deposited on the cuvette cell walls since no particles were left in the bulk solution at the end of the experiment (Fig. 3.3, peak diminishing). As shown in Fig. 3.4, in the presence of silicon in solution, the *induction period* (time required for the colloid to nucleate and grow larger than a few nanometers—the lower bound for detection by DLS, corresponding to the beginning point of the size increase from zero) became shorter. Obviously, after the initial nucleation, fluctuated sizes as shown in later stages of the measurements (Fig. 3.4) indicate that there is a size distribution due to particle aggregation and flocculation in bulk solution.

The coating formation is believed to depend strongly on the surface/chemical characteristics of the cell walls. It appears that the silicon in quartz is dissolved in the strong caustic solution (4 *M*), diffuses from the quartz wall into bulk solution, reacts with the aluminum species near the wall/solution interface, and subsequently forms a white solid coating on inner surface of the quartz cuvette. The dissolution of silicon from the quartz was confirmed by ICP analysis as well as by XRD (see Fig. 3.5). A detailed description of quartz dissolution by caustic solutions is included in Appendix C.

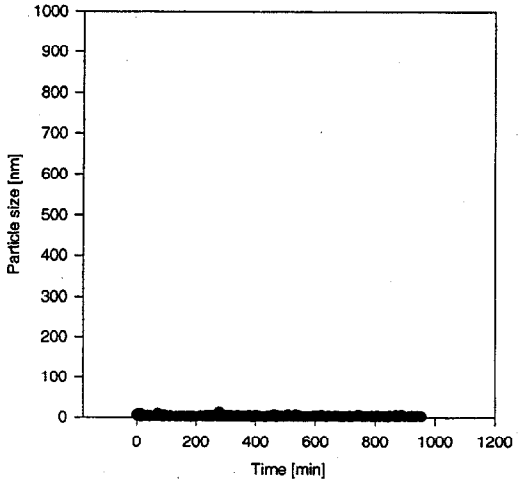

Fig. 3.1. DLS results for silicon-containing Solution B heated at 80 °C in quartz cuvette.

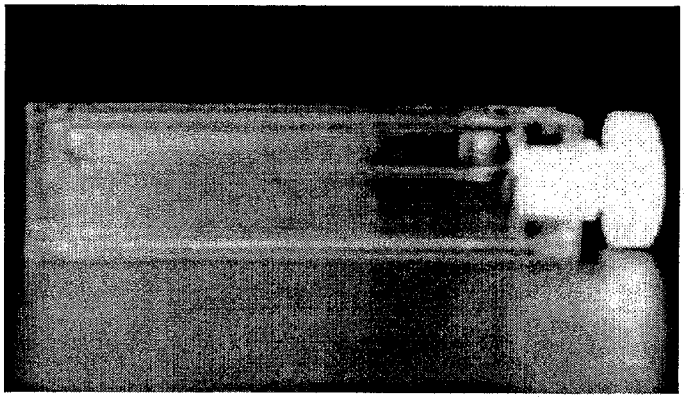

Fig. 3.2. Photograph of quartz cuvette after contact with aluminum-containing Solution A at 80°C.

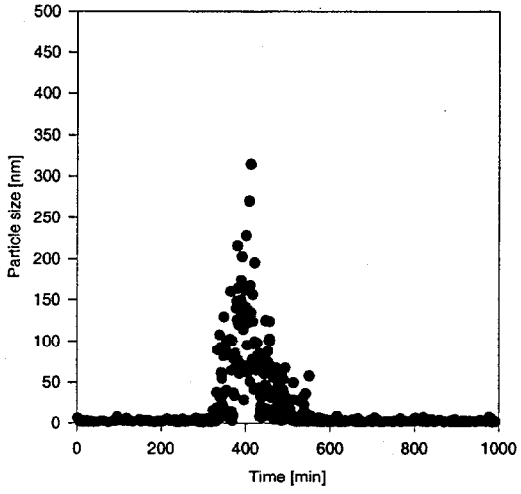

Fig. 3.3. DLS results for aluminum-containing Solution A at 80°C in quartz cuvette.

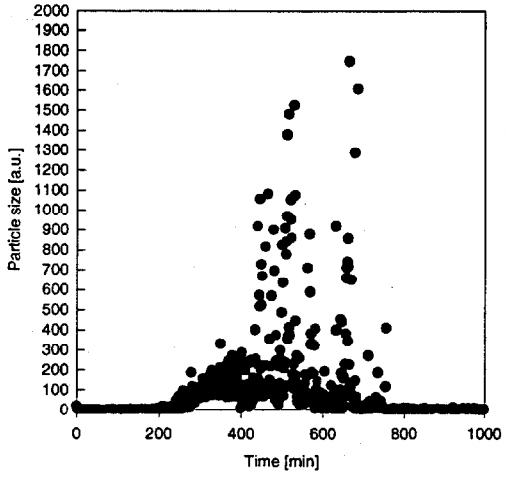

Fig. 3.4. DLS results for 0.133 *M* Al–0.004 *M* Si solution at 80°C in quartz cuvette.

Based on XRD analysis, the solid coatings on the inner walls of the quartz cuvette cells were identified to be predominantly sodium aluminosilicates (or sodalite) with the formula of $Na_8(Al_6Si_6O_{24})(NO_3)_2 \cdot 4H_2O$ (see Figs. 3.5 and 3.6). Such a composition in the case of heating aluminum-containing Solution A in a quartz cell confirmed the above silicon dissolution hypothesis. In this case, the only source of silicon to form the sodalite coating would be silicon dissolved from the quartz.

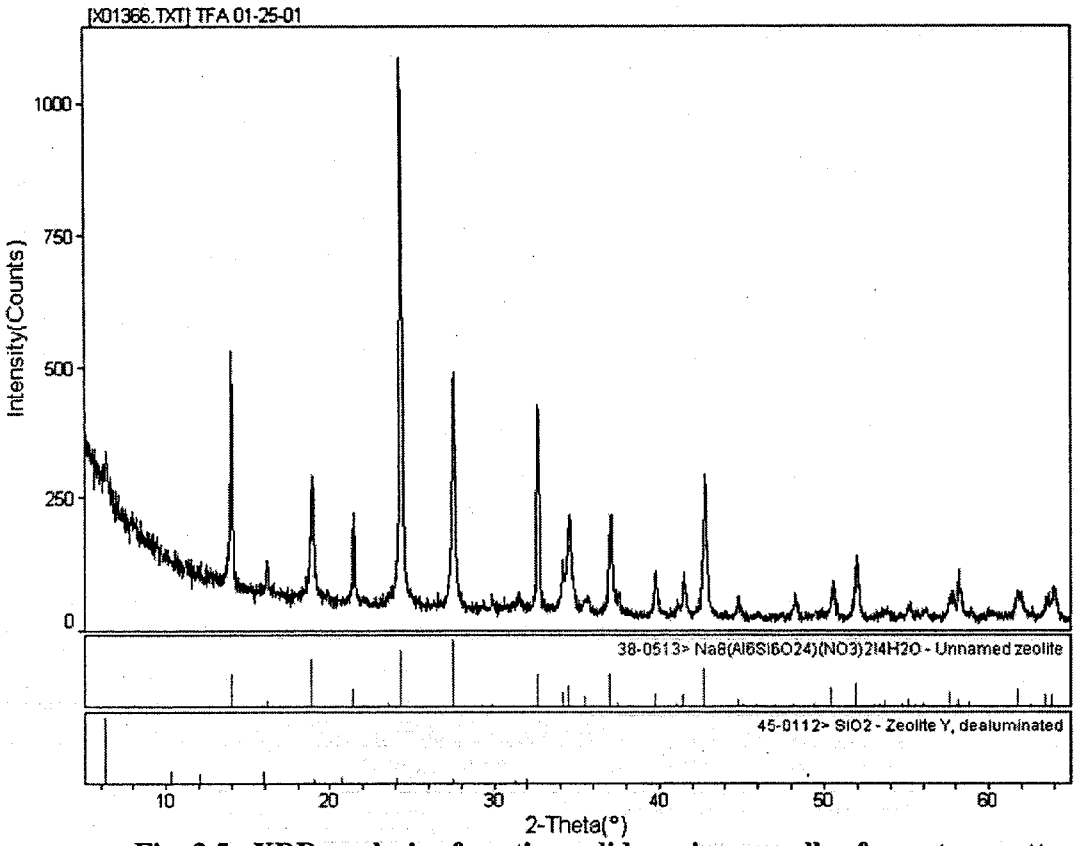

Fig. 3.5. XRD analysis of coating solids on inner walls of quartz cuvette, after contact with aluminum-containing Solution A in quartz cuvette at 80°C overnight.

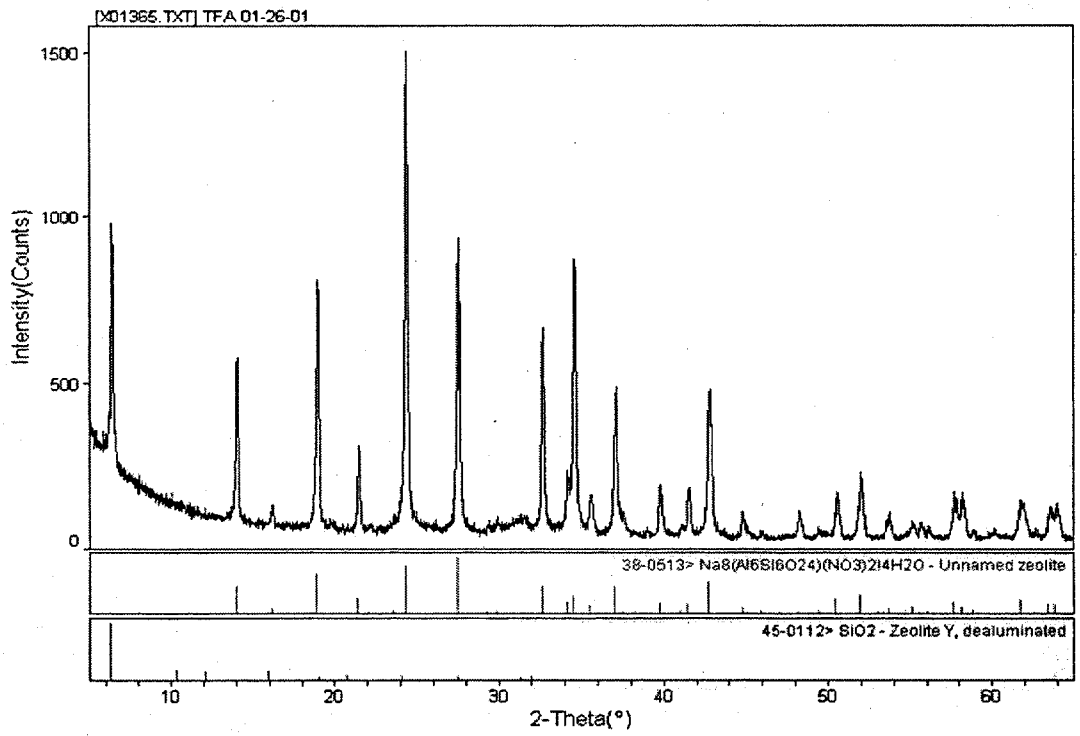

Fig. 3.6. XRD analysis of coating solids from inner walls of quartz cuvette, after contact with 0.004 *M* Si–0.133 *M* Al solution at 80°C overnight.

Polystyrene cuvettes were used for the majority of the DLS tests. Figure 3.7 clearly shows that polystyrene appears to be suitable for caustic solutions, while polycarbonate is not compatible. No coating or colloid was observed in the aluminum-containing solution A after overnight heating (at 80°C) in a polystyrene test tube and a cuvette. Polystyrene was found to be suitable for tests at temperatures up to 80°C. For higher temperatures, translucent Teflon test tubes with caps were used. Although those tubes reduced the overall laser-light intensity, results of tests conducted with particle-size standards indicated that the tubes were suitable for DLS.

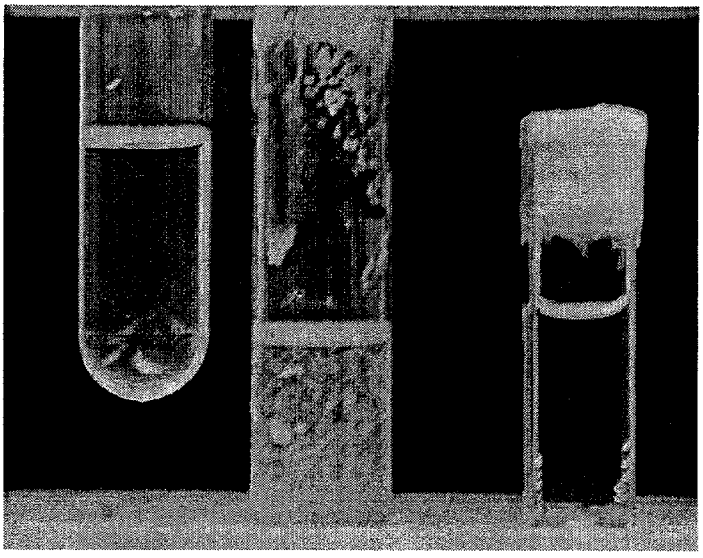

Fig. 3.7. Photograph of plastic cells from materials compatibility tests with aluminum-containing Solution A overnight at 80°C. The polystyrene test tube (left) and the polystyrene cuvette (right) were clear, while the polycarbonate test tube (middle) was discolored and contains solids.

3.2 STABILITY OF SILICON- AND ALUMINUM-CONTAINING SOLUTIONS

The system of interest involves the reaction between silicon and aluminum species in caustic solution (~ 4.0 *M* NaOH). Before looking into reaction-related solid/particle formation, it was necessary to know whether the solid would precipitate in a single-component solution in the desired background (containing 1.4 *M* $NaNO_3$, 1.0 *M* $NaNO_2$, 4.0 *M* NaOH).

In short-term (a few hours to a few days) experiments, the aluminum-containing source solution and silicon-frit solution were stable at elevated temperature (80°C) (Fig. 3.8). However, in more aged solutions (over 1 month at room temperature), flocculated precipitates were observed in the aluminum solution and colloids were detected in the silicon solution. Therefore, the solutions are not thermodynamically stable. Typically, the solutions used in these studies were filtered with 20-nm PTFE syringe disk filters (Anotop 25

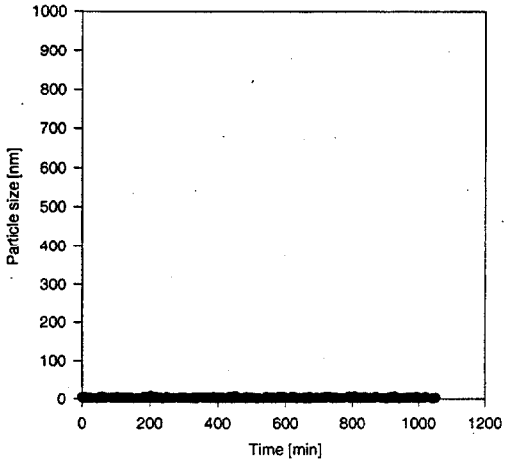

Fig. 3.8. DLS results for aluminum-containing Solution A at 80°C in polystyrene cuvette.

plus, Cat. No. 6809-4002, Whatman International, Ltd.) before being mixed. However, it was found that the small silicon colloids in silicon-source solution could not be completely filtered out.

3.3 PARTICLE FORMATION IN SOLUTIONS

Initial experiments were conducted to observe the nature of solids formed in polystyrene containers. Polystyrene test tubes were filled with the following three simulant solutions, sealed, and held overnight at 80°C:

(1) [Si] = 0.004 *M*, [Al] = 0.133 *M* (Si/Al = 0.03);
(2) [Si] = 0.05 *M*, [Al] = 0.133 *M* (Si/Al = 0.38); and
(3) [Si] = 0.133 *M*, [Al] = 0.133 *M* (Si/Al = 1.0).

As shown in Fig. 3.9, at low [Si] (0.004 *M*), no solid material was observed visually in the solution or at the bottom of the test tube. In the other two test tubes, solids were noted at the bottom of the test tube, while the bulk liquid was clear. In the test tubes with visible solids formation, salt-crystal-like solids were observed at the bottom of the test tube. It appeared that particles had settled on the test tube wall (because test tubes were tilted at an angle) and "fused" together into a connected, flaky layer. This layer fell off the wall with gentle shaking.

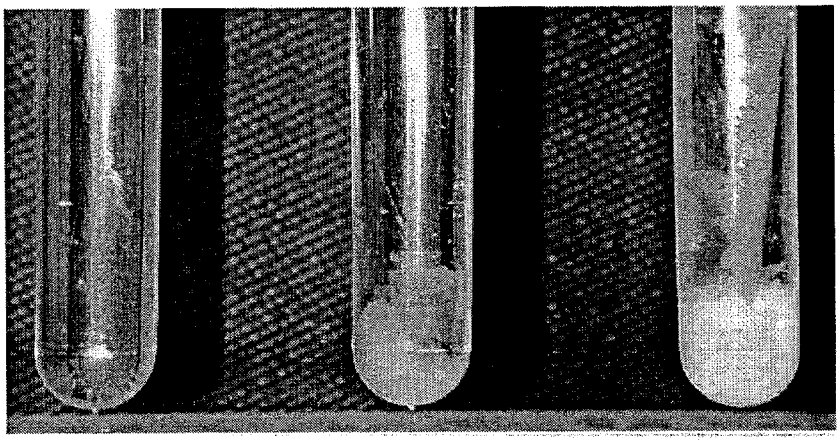

Fig. 3.9. Solids formed overnight in polystyrene test tubes at 80°C with various [Si] at [Al] = 0.133 *M*. Si/Al ratio is increasing from left to right: 0.03, 0.38, and 1.0.

Examination by SEM (Fig. 3.10, for Si/Al = 0.38) revealed that the settled crystal-like solid was actually connected microspheres of sodalite. Each microsphere particle contained many small sodalite crystalites. Microsphere size was affected by the reaction conditions, such as the concentrations of silicon or aluminum, temperature, etc.

The bulk solids collected from the above polystyrene test tubes (Si/Al ratios of 0.38 and 1.0) were identified to be predominantly nitrate-incorporated sodium aluminosilicates with a general formula of $Na_8(Al_6Si_6O_{24})(NO_3)_2 \cdot 4H_2O$ (called sodalite) based on x-ray diffraction analysis (see Fig. 3.11). The change in Si/Al ratio in the initial reactive solutions did not seem to affect the solid composition and crystal structure, indicating that soluble silicon species reacted with aluminum species in a stoichiometic manner. It appears that when silicon is deficient, the same sodalite solid forms, while leaving the unreacted aluminum species in solution

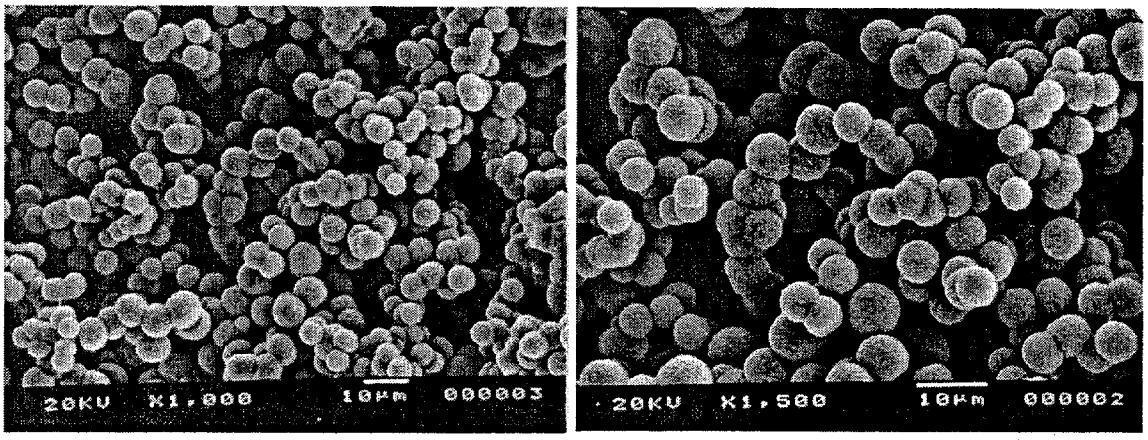

Fig. 3.10. SEM images of settled solids formed overnight in solution at 80°C. Si/Al ratio = 0.38; [Al] = 0.133 *M*.

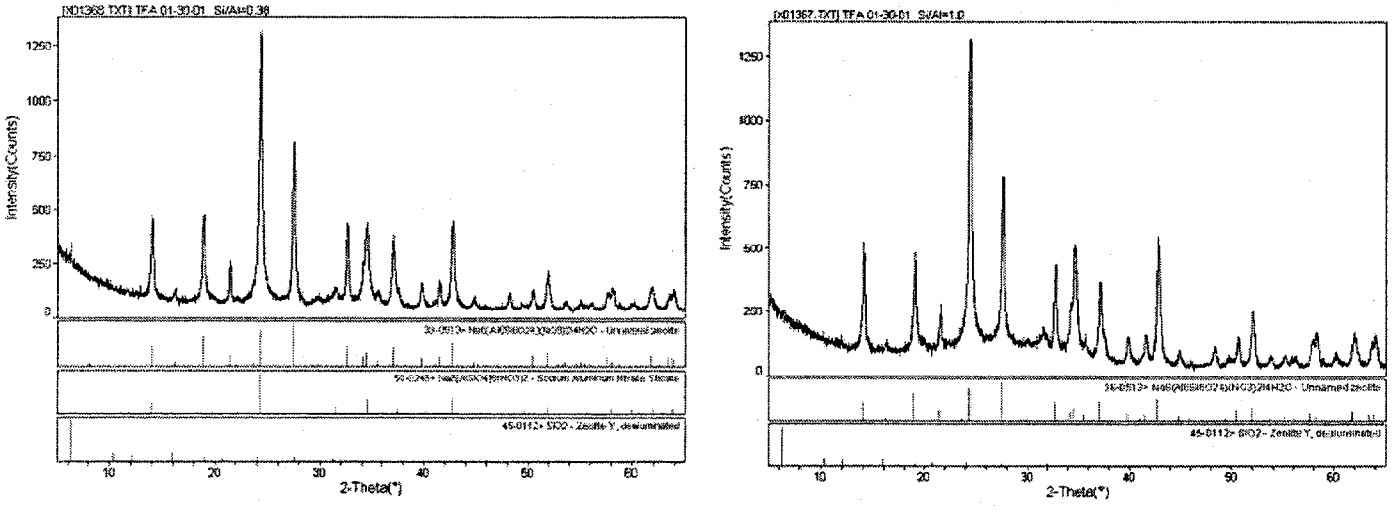

Fig. 3.11. XRD analyses of solids collected in polystyrene test tubes [Si/Al ratio = 0.38 (left) and 1.0 (right)].

Typical DLS data that monitor the formation and growth of solid particles with time in simulant solution are shown in Fig. 3.12. In this figure, the particle size, as determined through autocorrelation of scattered light fluctuations using established commercial software, is shown by the dark circles. Light circles represent the intensity of scattered light, related to the concentration of particles suspended in the solution. The particle size is reported in arbitrary units in this plot to emphasize that particle-size determination by DLS depends on many parameters, such as temperature, particle number density, and the refractive index and viscosity of the solution. During the course of these reaction and particle growth processes, the solution viscosity changes significantly, although the refractive index does not (see Appendix D). For the convenience of data processing, we chose averaged values of viscosity and refractive index for particle-size calculations for a given particle-growth course. Since we did not have an exact value for these quantities for every point in time point during the reactions, the size determined is arbitrary but does not deviate greatly from the true value for hydrodynamic diameter in nanometers. Since the DLS size-vs-time curve is mainly used to determine induction period, the "arbitrary unit" treatment is suitable for the purpose of these studies.

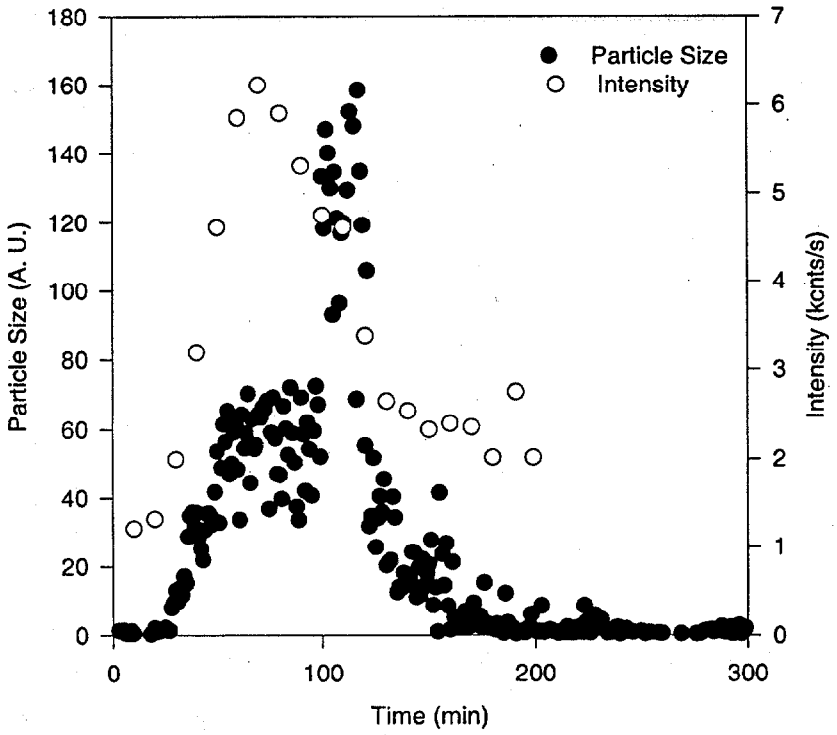

Fig. 3.12. Typical data collected by real-time DLS. This figure shows the capability to monitor the complete process of solids formation in quiescent simulant solution, from particle evolution to settling.

The DLS technique appears to capture the nature of the hydrothermal solid formation process. Figure 3.12 indicates that the formation of solids in solution involves several stages:

(1) An induction period[6] (the time needed for nucleation and growth into a detectable population of particles larger than a few nanometers), a measure of particle formation dynamics in bulk solution. The cross point between a line fitting the initial particle growth curve and the time axis determines the "induction period." Meanwhile, the scattering intensity-vs-time data are also helpful to determine induction period. The shorter the induction period, the faster the particle evolution in solution.

(2) A particle-growth stage, corresponding to the initial particle-size increase and increase in scattering intensity.
(3) Particle aggregation/agglomeration, corresponding to the intermediate region of the growth curve. Aggregation/agglomeration contributes to particle growth and settling.
(4) Particle settling (corresponding to the particle-size decrease and decrease in scattering intensity).
(5) Short-range interaction or reaction of contacted particles (after settling and contact between particles), leading to the formation of connected, chunky solids (or flaky layers on the test-tube wall).

At the beginning stage of the solids formation, an increase of particle size and number density will monotonically correspond to the increase of scattering intensity. However, the solution contains high electrolyte concentrations, and in turn the electrostatic double layers around the particle surfaces are significantly depressed. The very weak electrostatic repulsion between particles leads to a very unstable colloid system, causing particle aggregation.[8]

The effects of process parameters such as temperature, silicon concentration [Si], and aluminum concentration [Al] were studied by DLS determination of the induction period (t_I). Induction-period data are tabulated in Appendix E, along with a description of the methods used for estimating the induction period. The relative standard deviation of induction period determinations was found to be below 10%, based on triplicate experiments. Detailed particle size and intensity-vs-time data are included as Appendix F. Data showing t_I vs temperature, t_I vs [Si], and t_I vs [Al] are presented in Figs. 3.13 through 3.16.

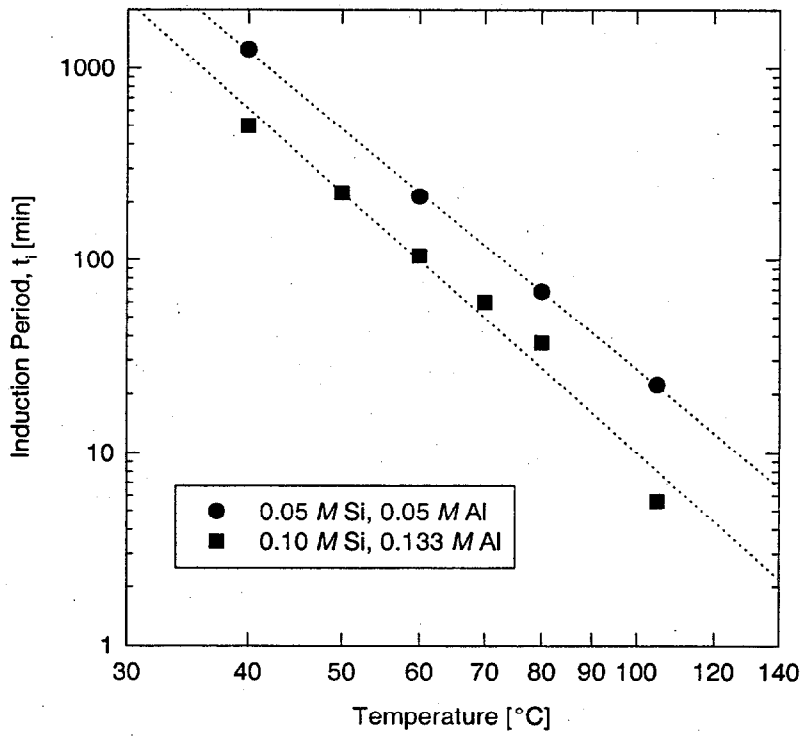

Fig. 3.13. Effect of solution temperature on particle formation.

As shown in Fig. 3.13, the induction period decreased with increasing temperature. The temperature of the solution was slightly lower than the temperature setpoint of the equipment at higher temperatures; at 40°C setpoint, there was essentially no error, while the experiments set at a nominal temperature of 80°C were

conducted at 77°C, and a setpoint of 111°C was required to establish a solution temperature of 105°C. Temperature control remained within ±1°C. There appears to be a fairly good linear relationship between the induction period and the temperature in a log-log plot. Thus, it is possible to predict the induction period at various temperatures for a given composition with only a few experiments at different temperatures. Using this relationship, the induction period at boiling temperature (~110°C for 4 *M* NaOH caustic solution) is predicted to be on the order of 5–10 min, depending on the concentrations of silicon and aluminum. Variation of the compositions does not seem to significantly affect the slope of the linear relationship. Based on a relationship similar to Arrhenius' law,

$$\ln\left(\frac{1}{t_I}\right) = -\frac{E}{R}\left(\frac{1}{T}\right) + \ln(\text{constant}),$$

where R is the universal gas constant (8.3144 J/K· mol) and T is temperature (K), the activation energy (E) for sodium aluminosilicate particle formation may be estimated by plotting of $\ln(1/t_I)$ vs $1/T$. As shown in Fig. 3.14, such a plot is quite linear and leads to an estimate of E of ~65 kJ/mol. In the literature, activation energies for desilication or crystallization processes in similar systems ranging from 30 to 92 kJ/mol[5,9-11] have been reported, based on the reactant consumption kinetic data under seeded or unseeded conditions. Mattus et al.[5] determined an activation energy of 35 kJ/mol for waste simulant solutions without seeding, based on reactant consumption kinetic data. Clearly, seeding affects the desilication rate (relative supersaturation vs. time) and the activation energy requirement for growth on seed crystals. With sodalite seeding, Barnes et al.[10] determined an activation energy of 30 kJ/mol based on the desupersaturation of silica and growth of seed crystals, while an activation energy of 63 kJ/mol was obtained for a seeded process of nitrated cancrinite formation,[11] which is close to the value determined here.

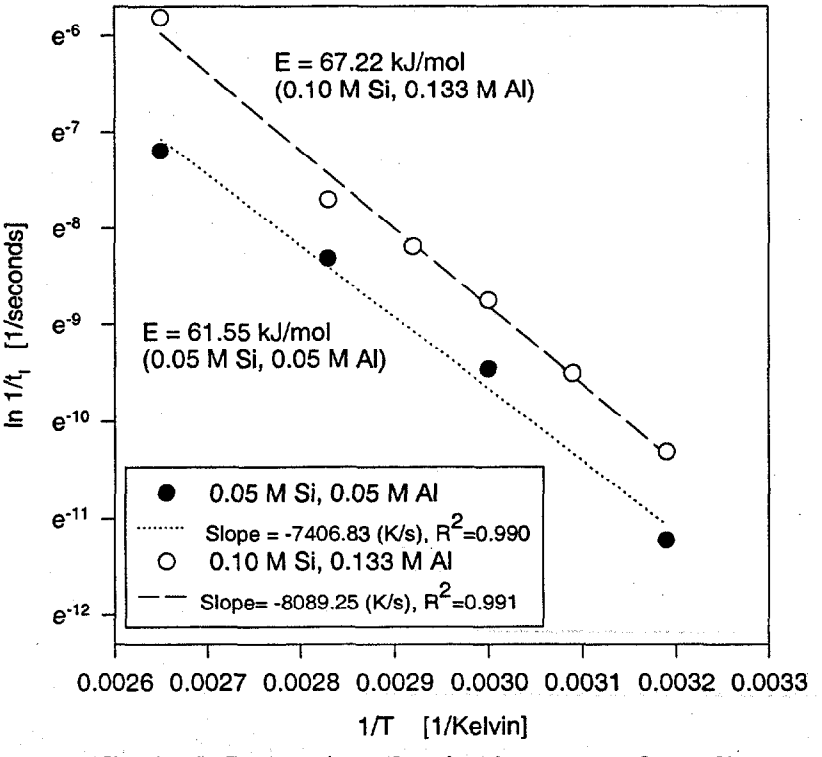

Fig. 3.14. Estimation of activation energy for sodium aluminosilicate particle formation. Parameters of fitted lines: dashed line – slope = –8098, intercept = 15.46; dotted line – slope –7406, intercept = 12.56.

It is important to point out that sodium aluminosilicate solid formation from soluble reactant silicon and aluminum species involves multiple complex steps: soluble species → oligomers or polymers → sols (solid clusters or nuclei) → gels (amorphous) → zeolite A → sodalite → cancrinite. Reactant consumption kinetic measurements provide only an indirect measure on the solid formation or crystallization process. Activation energy values based on unseeded reactant consumption kinetic data do not fully describe crystallization since phase transformation steps may not consume any soluble reactants. The activation energy determined by reactant consumption kinetics might mainly reflect the activation energy for the process of turning soluble species into insoluble solid gel, since further growth of crystals or crystallization from gel precursors may not consume any soluble reactant species. The DLS technique directly detects the solid phase formation, so the activation energy determined by the DLS technique is clearly related to a given state of solid formation, which may be the result of multiple phase transformation steps beyond nucleation of amorphous solid. The very first solid particles detectable by DLS in these experiments may have already been fully crystallized, since the 65-kJ/mol activation energy for the evolution of detectable solid is very close to the 63-kJ/mol value for growth of nitrated cancrinite. If this is true, it may mean that the crystallization from gel is a fast process while the solid-phase nucleation from soluble species (due to polymerization) is rate limiting, which controls the overall solid growth rate.

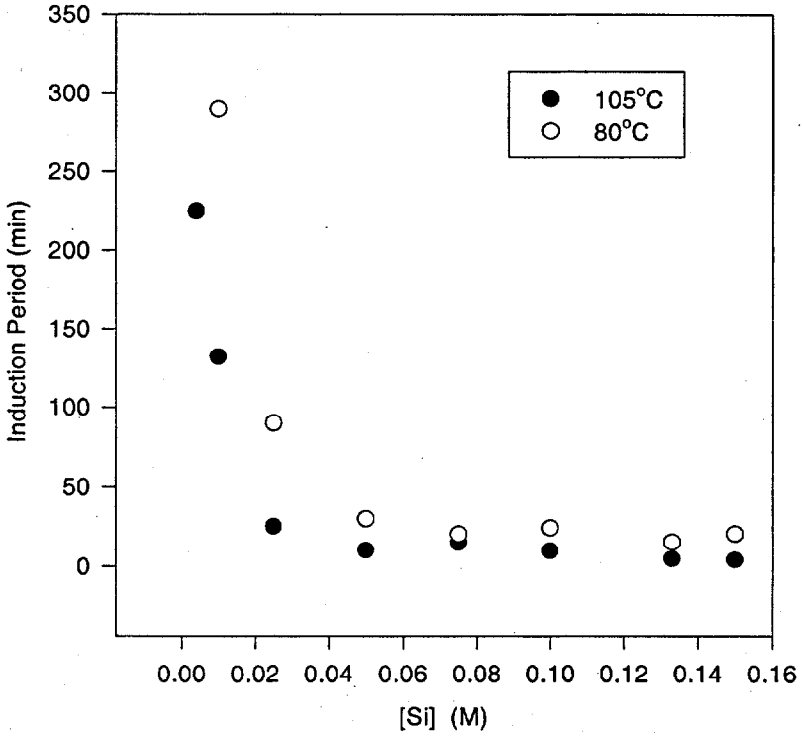

Fig. 3.15. Effect of [Si] on particle formation dynamics.
Constant [Al] = 0.133 *M*.

The effect of [Si] on the induction period for [Al] = 0.133 *M* is shown in Fig. 3.15. Particle formation occurred faster as [Si] was increased from 0.01 to 0.05 *M*; however, little effect on the induction period was measured as [Si] was increased above 0.05 *M*. Variation of temperature did not appear to affect this trend.

The effect of [Al] on the induction period for [Si] = 0.05 *M* is shown in Fig. 3.16. Particle formation occurred faster when [Al] was increased throughout the range from 0.03 to 0.30 *M*. The log-log plot (see insert) seems to show a linear relationship between the induction period and [Al] at 80°C. There is greater scatter in the data for 105°C, mainly due to the lower sensitivity for determining induction periods using a round, sealed Teflon test tube as the DLS cell at the elevated temperature.

Preliminary results were obtained on the effect of seeding on particle formation as shown in Fig. 3.17. New, silicon-containing frit solution (Solution B, prepared as described in Appendix A) is clear; however, aged frit solution is slightly cloudy if it stays at room temperature for periods longer than 1 month. The existing sub-100-nm particles in aged frit solution were used as seed particles. Such seed-containing silicon solution was mixed with aluminum-containing solution for a DLS experiment at 80°C. Clearly, the presence of seed particles in the reaction mixture reduced the induction period for particle growth at the studied conditions by approximately one-third. No further tests were conducted to determine the reproducibility of the effects of aging of silicon-containing solution. Further investigation is needed in regard to seeding effects on solid growth in solution as well as on surface deposition and solid growth at surfaces.

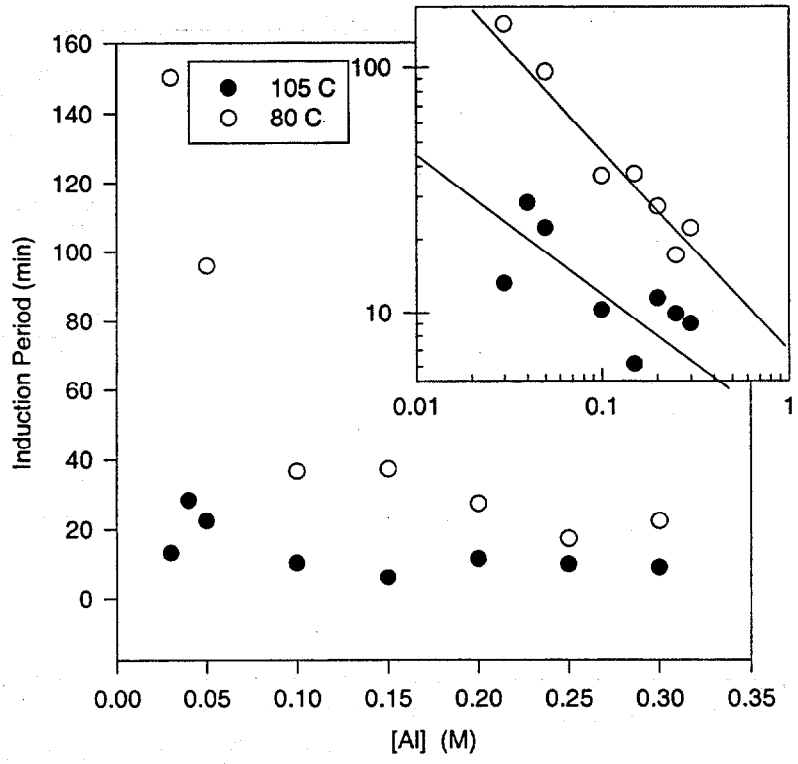

Fig. 3.16. Effect of [Al] on particle formation dynamics. Constant [Si] = 0.05 *M*.

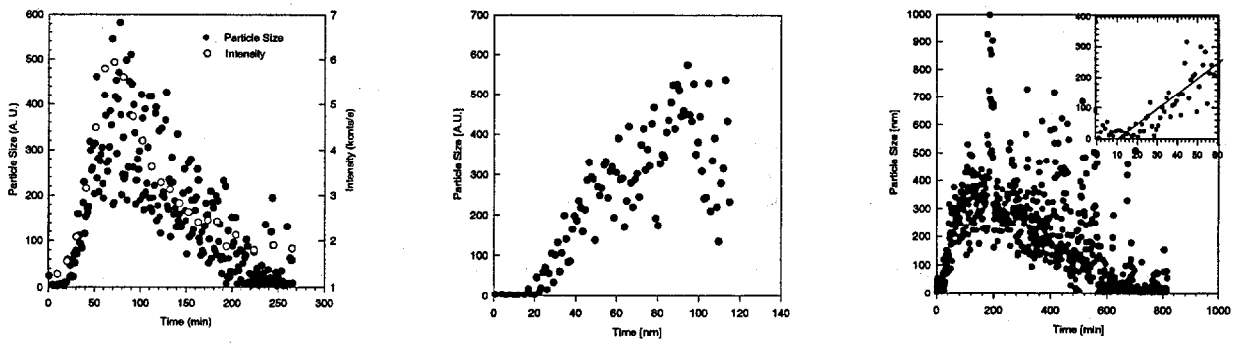

Fig. 3.17. Effect of seeding on particle growth dynamics. Left and middle: duplicate experiments using clear silicon-source solution, t_I = 17 and 16 min. Right: experiment using cloudy silicon-source solution, t_I = 11 min. [Si] = 0.075 *M;* [Al] = 0.133 *M; T* = 80°C.

3.4 FORMATION OF "SURFACE SOLIDS"

As discussed earlier, solids could grow directly on the surfaces of a solid substrate (such as 2H evaporator tank walls) via heterogeneous/surface-growth phenomena. In addition, the solid on the tank-wall surfaces could be due to deposition of particles from solutions, attaching and sticking on these surfaces. Regardless of the mechanism, any formation of solid material in bulk solution would affect the formation of solids on surfaces either via growth of "surface particles" or via deposition of "bulk particles." Our results, as shown below, demonstrate that both "growth" and "deposition" mechanisms can occur during the formation of a surface solid (i.e., scale) in laboratory experiments with simulant solutions. The objectives of surface solid/particle formation studies are

- to confirm the "surface-solid" formation phenomena in experimental simulant solutions;
- to understand the mechanisms of solid formation on stainless steel foil surfaces, which may shed some light into the cause of solid deposits/scale formation in the Savannah River 2H evaporator;
- to monitor the growth dynamics of particles on the surfaces;
- to correlate onset times for particle growth in solutions (i.e., induction periods) and the onset time for formation of surface solid particles; and
- to understand the effects of process conditions on the bulk/surface particle transformation and growth dynamics.

3.4.1 Tests with Quiescent Solution

Scoping tests. Scoping studies on foil deposition were conducted using vertical foil strips (with some tilting at an angle against the test-tube wall) submerged in solutions in polystyrene test tubes. Results of these tests showed that no solid coatings were visible on the polystyrene surfaces or on the metal placed in distilled water, NaOH solution, or Solution 2A. In contrast, a significant amount of solid material was deposited on the foil in the tube containing the silicon/aluminum mixture (see Figs. 3.18 and 3.19).

In addition to the mass settled to the bottom of the test tube and deposited on the horizontal metal surface in the silicon-aluminum solution, a rough, white coating formed on the vertical surface of the foil (see Fig. 3.20). This coating was relatively tough and adherent; it did not fall off into solution with moderate agitation of the fluid. The backside of the foil (right image of Fig. 3.20) was also coated with a solid layer, although visibly much thinner. This is an important observation, because it indicates that solids deposition on the foil was not due only to settling but also involves heterogeneous/surface growth. Continued foil deposition tests were conducted with horizontally positioned stainless steel foil strips that were submerged in reaction mixtures contained in Teflon vessels (as shown in Fig. 2.4).

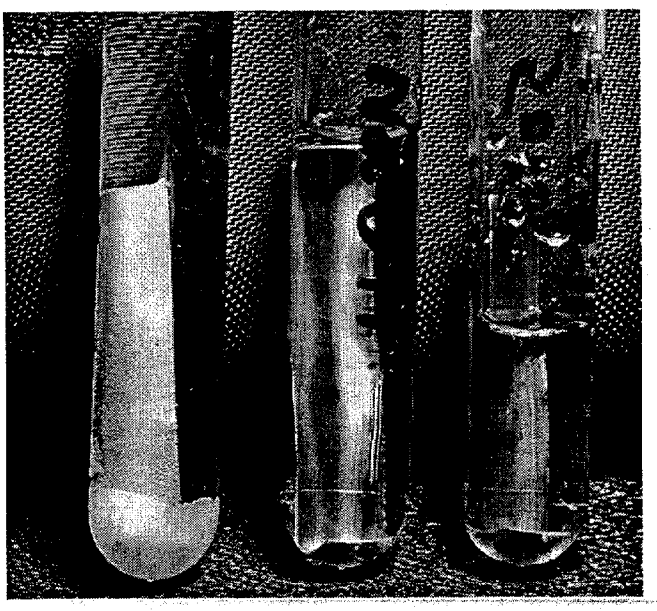

Fig. 3.18. Test tubes containing 304SS foil after 41 h in simulant solutions at 80°C. From left: 0.1 *M* Si, 0.133 *M* Al in 6 *M* Na; 4 *M* NaOH; Solution 2A (0.266 *M* Al).

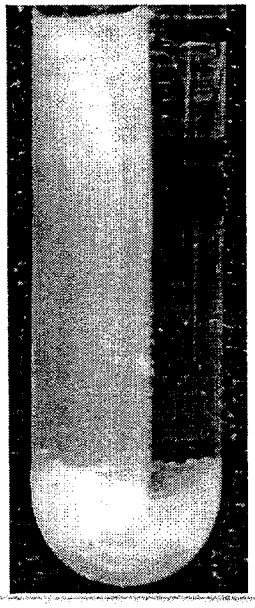

Fig. 3.19. Close-up of foil surface and settled solids from 0.1 *M* Si–0.133 *M* Al solution.

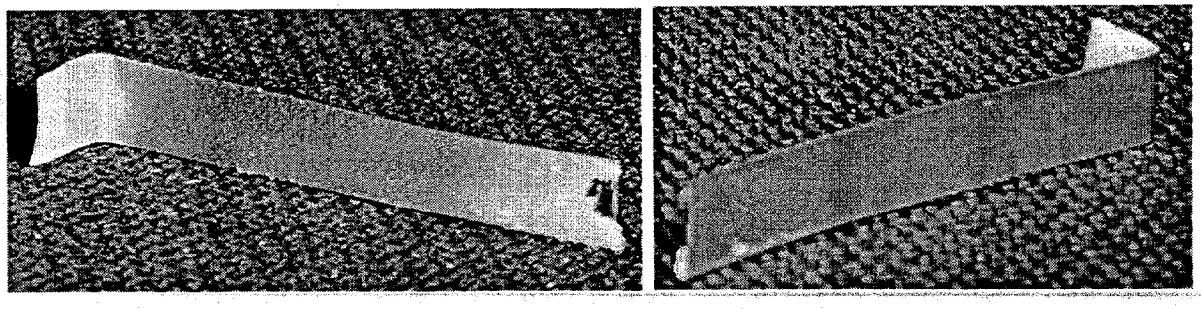

Fig. 3.20. Solid coating formed on 304SS foil placed in quiescent 0.1 *M* Si–0.133 *M* Al solution for 41 h at 80°C. The long portion of the foil was vertical (with a slight tilting angle) in the tube, while the short section was horizontal. Image at left shows significant solids deposition on the side of the foil facing the bulk solution; image at right shows a thin solid layer on the back side of the foil.

Effect of [Si] on surface-solid formation. Foil samples coated with solids by holding them at 80°C for 64 h in solutions containing varying concentrations of silicon and 0.133 *M* aluminum in 4 *M* NaOH are shown in Fig. 3.21. For the photograph, the foils were cut and the top side placed upward in the front, while the bottom side was place upward in the back. No solids were observed on foil surfaces (top or bottom) in silicon-free solution (sample 1). Thick layers of solid deposits were observed on the top sides of foils in solutions that contained silicon (samples 2, 3, and 4). With increasing [Si] in the solutions, more solids accumulated on the top sides of the foils. On the bottom sides of the foils, thin solid coatings could barely be seen through visual observation.

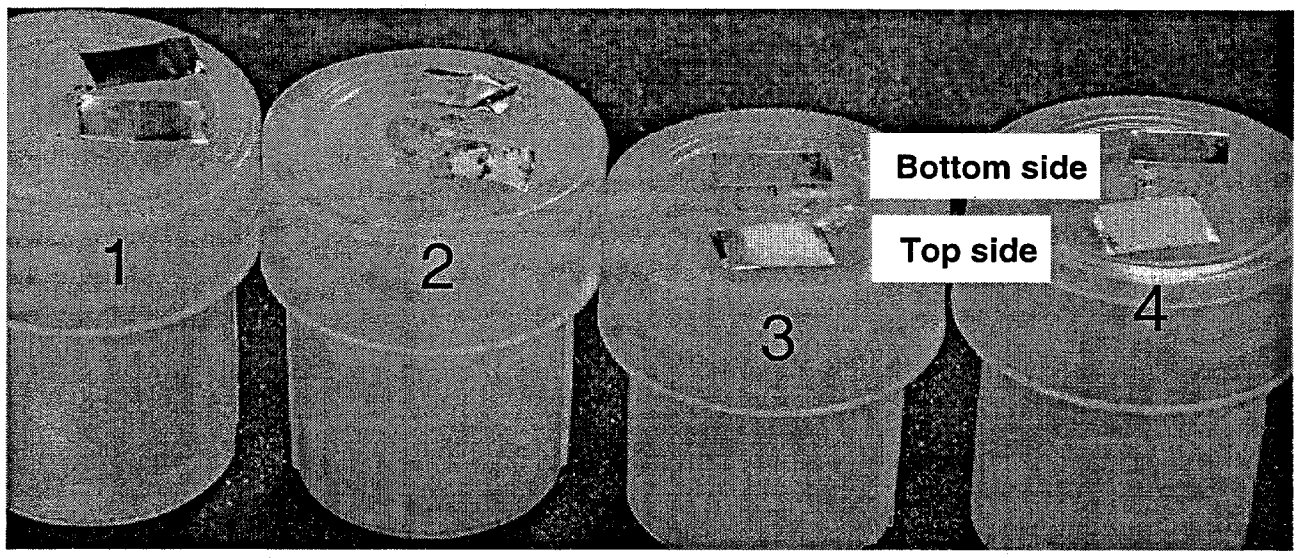

Fig. 3.21. Visual observation of [Si] effect on surface solid formation on 304SS foil surfaces. From left to right, [Si] is increasing: 0, 0.05, 0.133, and 0.15 *M*.

Further examinations of these samples with SEM revealed detailed microstructure of the surface solids (Fig. 3.22). Solids on the top sides consisted of connected microsphere particles (grown together) that were originally from bulk solution. With increasing [Si], the microsphere particle size increased. For the well-grown microsphere particles in thick solids (samples 3 and 4), particle surfaces appeared "rough" or "spiked" (see insert for top side of sample 3 in Fig. 3.22). In addition, a significant finding was that particles grow on the bottom side of foils (for example, Fig. 3.22, bottom side of sample 3). Such "surface-particle" growth can be attributed to heterogeneous nucleation or initial nanocluster deposition, but was not due to settling/deposition of particles that hadalready grown in bulk solution. This surface particle growth occurred in monolayer form; in other words, it appears that no second layer of particles grew on top of the first surface layer of particles under the conditions of this test. The surfaces of the "particles" or "mounds" that formed on the bottom surfaces were rough, similar to those of the particles that were deposited from solution.

The resulting foils are shown in Fig. 3.23. The foil removed from solution at 30 min appeared to be shiny and clear of solids. Because it was dull gray instead of shiny, the 60-min sample appeared to have a light coating. Each of the foils from the 120-min and 240-min samples had a thick coating on the upper surface. The bottom surface of the 30-min sample was shiny, while the bottom surfaces of the other foils were slightly dull gray.

Top side - deposited/connected particles originally from bulk solution

(Sample 2) (Sample 3) (Sample 4)

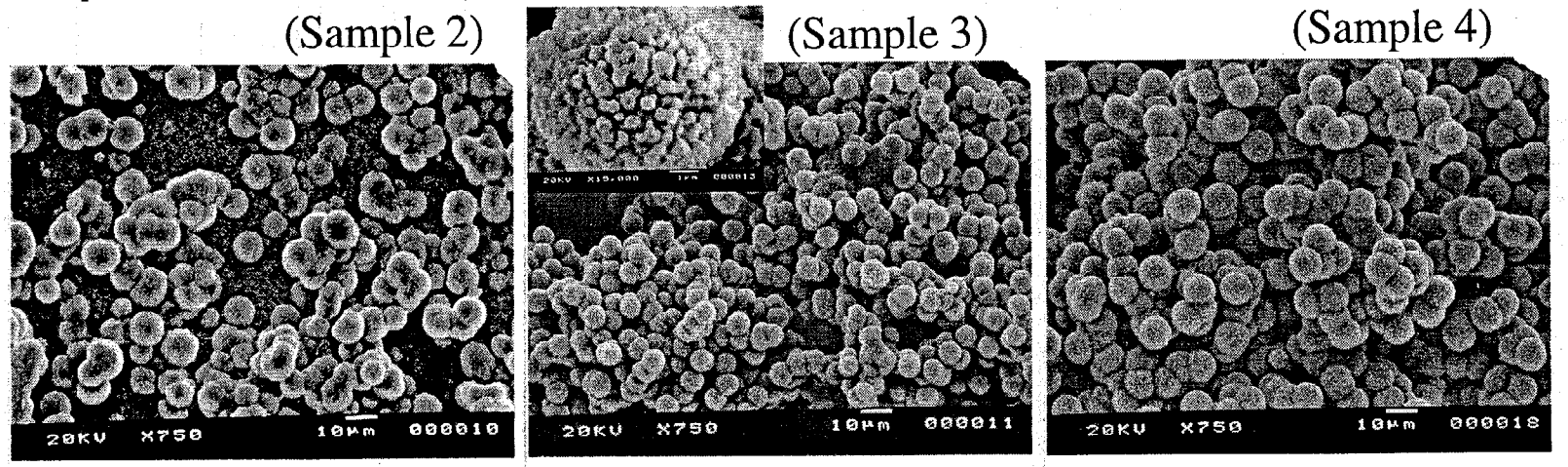

Bottom side - layer of surface grown particles

(Sample 3, increasing magnification from left to right)

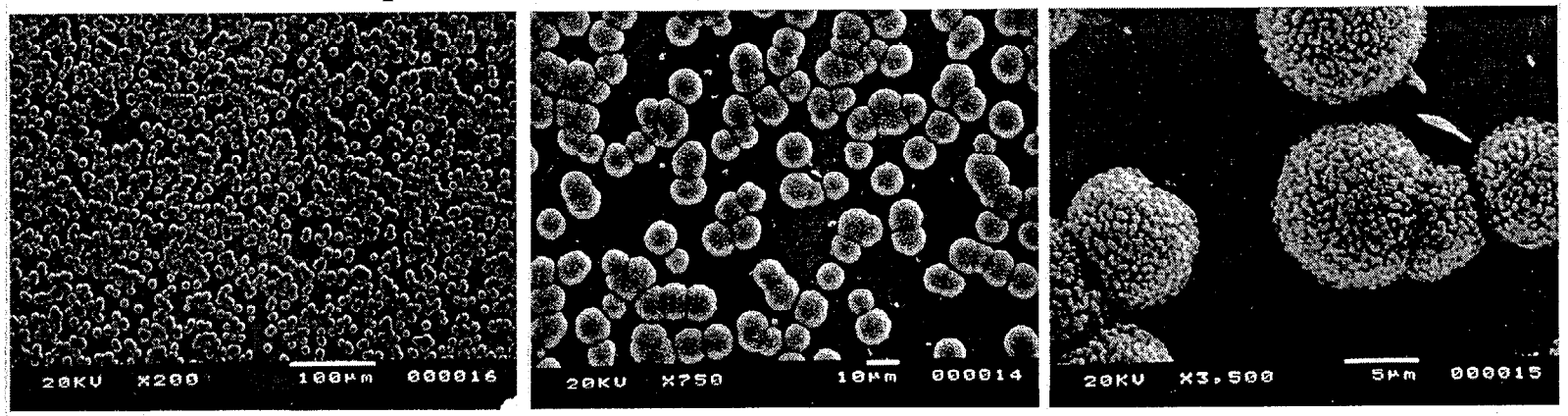

Fig. 3.22. SEM images of surface solids on both sides of stainless steel foils, obtained from solutions of various [Si] while maintaining [Al] = 0.133 *M*. Sample numbers correspond to the numbers in Fig. 3.21.

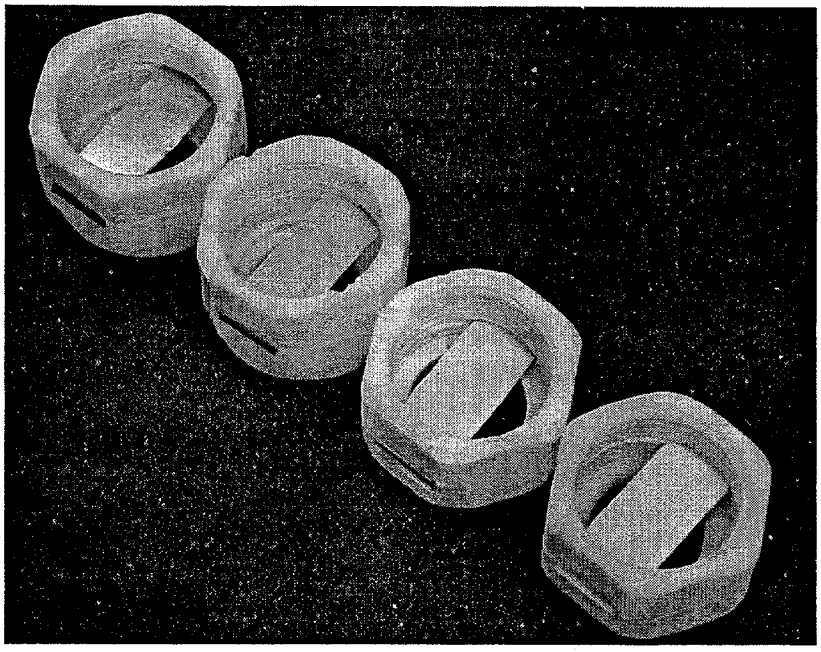

Fig. 3.23. Foils from surface-solid-formation test with 0.133 *M* Si–0.133 *M* Al solution at 80°C. From left to right: 30-, 60-, 120-, and 240-min samples.

Effects of reaction time and temperature on surface solid formation. An additional test was conducted to investigate the effect of reaction time on growth of solids on the surfaces of stainless steel foils in quiescent solutions. The objective was to determine the relationship between particle growth in bulk solution and solids growth on the steel surfaces. The test was conducted with 0.133 *M* Si—0.133 *M* Al at 80°C. Results of previous DLS tests had indicated that the nucleation time for these conditions was near 30 min, the peak of the growth curve was at approximately 2 h, and settling was nearly complete at 4 h. Based on that information, vessels were removed from heating at 30, 60, 120, and 240 min, corresponding to periods when (a) particle nucleation in solution was just beginning, (b) the particles were in the initial growth phase, (c) the particles appeared to be aggregating and settling, and (d) particle growth and settling appeared to be complete. The turbidities of the solution samples collected were consistent with the light scattering results. The solution removed at 30 min was clear, while the solutions removed at 60 and 120 min were turbid; and the 240-min solution sample was clear.

SEM images of the upper and lower surfaces of the foils are shown along with DLS results for the same composition and temperature conditions in Fig. 3.24. The upper and lower foil surfaces at 30 min (near the nucleation time) are essentially free of solids. The 60-min sample shows that solids have settled on the upper surface; in addition, there are a significant number of particles on the bottom surface. The particles on the bottom surface are similar in size to those that settled on the upper surface. It is not clear whether the particles on the surface originated from a heterogeneous nucleation at the surface, or whether they were formed by the attraction of nanoparticles to the surface. The particles at both the top and the bottom surfaces at 120 min are larger than those at 60 min. Most particles are shaped like balls of yarn in the 120-min sample of the top surface; however, a few cube-shaped particles are visible. There is a general trend that increasing the reaction time will increase particle sizes. The growth of the particles at the bottom foil surface is significant. While the particles at the top surface at 240 min appear to be the same size as those at 120 min, the particles at the bottom surface appear to have grown in the period from 120 min to 240 min—more nearly forming a complete monolayer. The cracks in the solid layer in the 240-min sample are probably due to

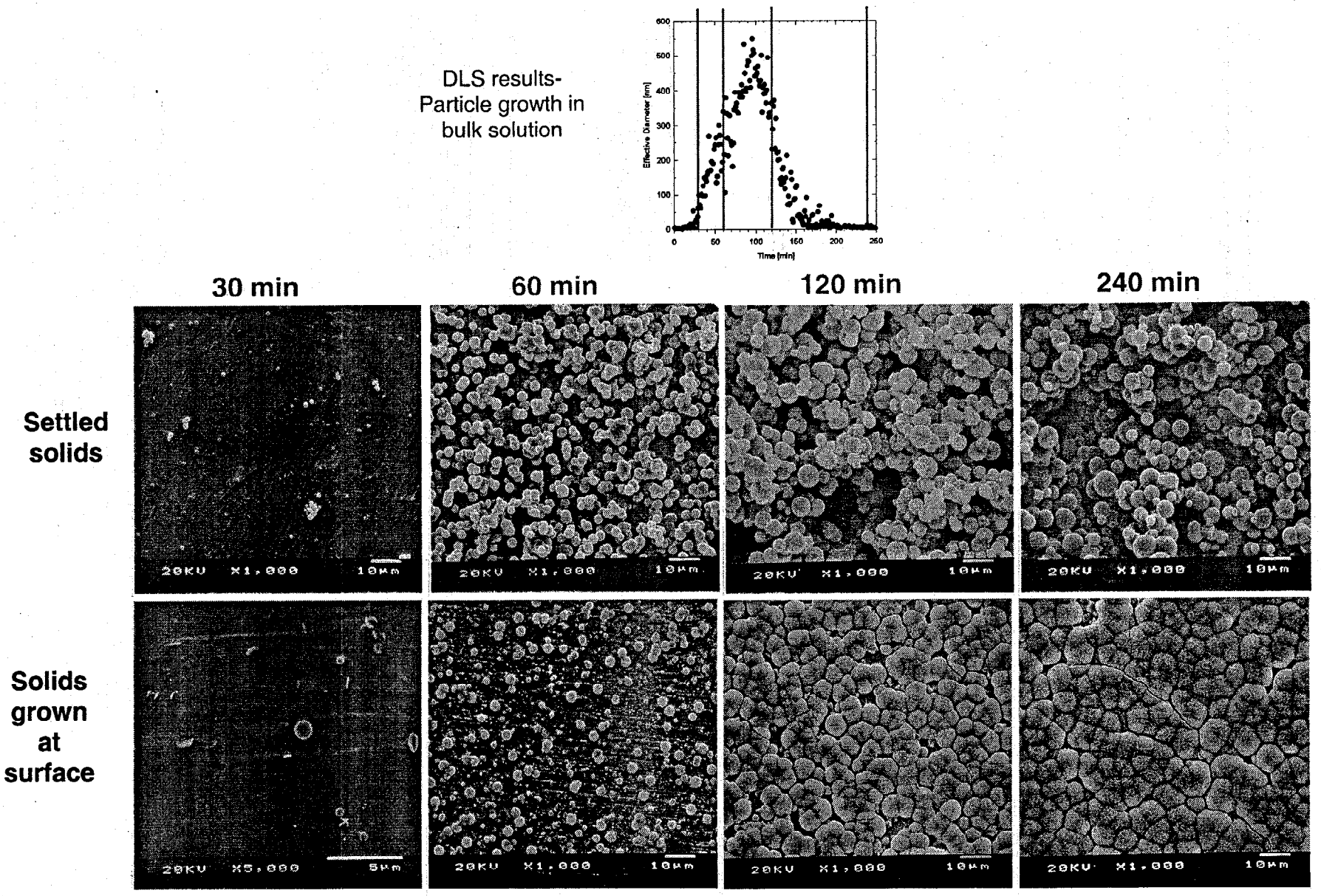

Fig. 3.24. Effect of reaction time on surface-solid formation in solutions of 0.133 *M* Si–0.133 *M* Al–6 *M* Na^+ at 80°C. Images labeled "Settled solids" are of the upper surface of the foils; those labeled "Solids grown at surface" are of the bottom surface of the foils. Sample times (see DLS curve) were selected to correspond with the following phases: nucleation time, middle of growth stage, aggregation, and fully settled.

drying; it is notable that in several instances the cracks run through surface particles (grain-like) rather than only along interfaces between particles (grain-boundary-like). The cracks through the surface-grown particles appear to be an indication that as the particles have grown together, the bonding between them is as strong as within the particles.

The material on the top side of the 120-min sample was poorly adhered to the foil and thus did not hold together well. The material from the top surface of the 240-min sample was also weakly adhered to the foil, but it was strongly consolidated. As seen in Fig. 3.25, this material held together well as a single mass. SEM analysis of the material removed from the top of the foil after 240 min of exposure to the solution at 80°C appeared to indicate that settled particles could grow together into a consolidated solid.

As shown in Fig. 3.26, the material that was exposed to the solution consists of individual particles (as in a porous solid), while the solids at the solid-steel interface appear to have grown together into a single mass with high density, having only a small fractional area of voids. There appears to be a mass-density gradient from the surface porous solid to the steel surface; the highest density is near the solid-steel interface.

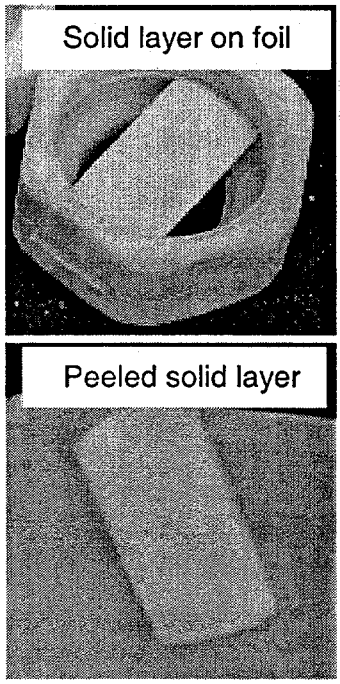

Fig. 3.25. Unsupported, membrane-like solid, detached from top surface of foil in 240-min sample (after drying at room temperature).

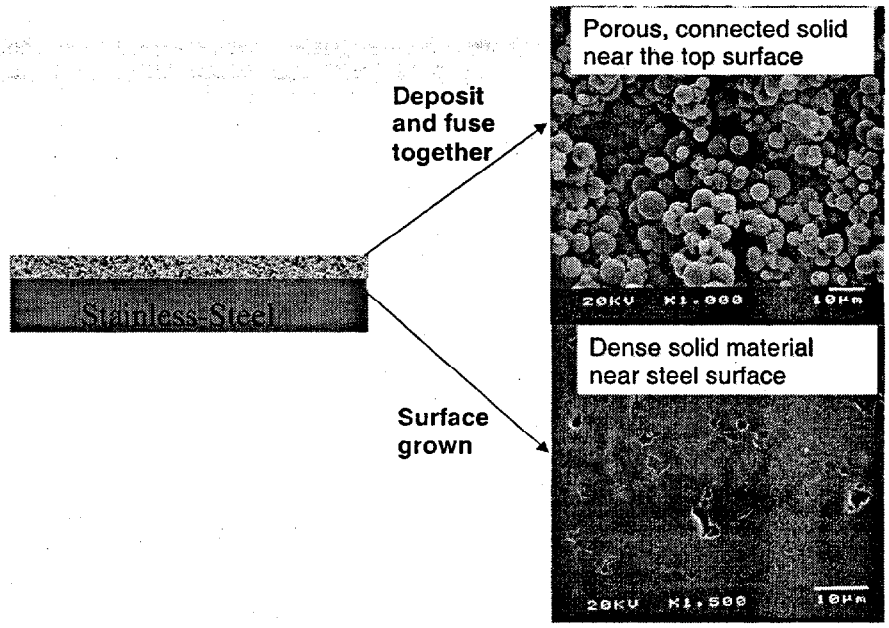

Fig. 3.26. Settled solids on top of foil (240-min sample) show a mass-density difference between the upper solid surface and the solid-steel interface.

Another experiment with a starting solution having the same composition was conducted at 100°C. Samples were collected at 36, 72, and 150 min, as well as overnight (21 h, 50 min), and the foils were analyzed by SEM (see Fig. 3.27). Similar to the 80°C results, both bulk and surface particles grew with increasing time, and surface particle growth again seemed to correlate with bulk particle growth. It is of note that the 36-min sample suggests that the initial particles grown on the steel surface were cubic-shaped crystals (Fig. 3.28, left image), instead of spheres (see in bulk solution, Fig. 3.28, right image). Initial surface crystal/particle growth occurred on both sides of the foil (Fig. 3.28). Morphological transformation of

deposited/settled "bulk grown" particles on the top side of foils is shown in Fig. 3.29. Clearly, the morphology of the deposited particles changed with time:

spheres → dimpled spheres → spiked balls.

The morphological transformation of "surface-grown" particles (Fig. 3.30) seemed to follow a somewhat different course:

cubic crystals → "balls of yarn" grown on top of cubic crystals → lumpy balls → "coral-like" mounds.

Surface microspheroids appeared to grow by consumption of the cubic crystals. Surface microspheroid particles on the bottom side of the foils showed a different surface morphology from that of bulk microspheres on the top side of foil, as shown in Fig. 3.31.

These morphological changes are consistent with the following process of sodium aluminosilicate crystallization: amorphous to zeolite A to sodalite to cancrinite.[9] The cubic crystals are similar to those reported by Dworjanyn[3] to be zeolite. The "balls of yarn" are similar to results obtained by Dworjanyn[3] and Addai-Mensah[9] for sodium aluminosilicate (sodalite/cancrinite), while the spiked balls and "coral-like" mounds are similar to the morphology of nitrated cancrinite synthesized by Barnes et al.[10]

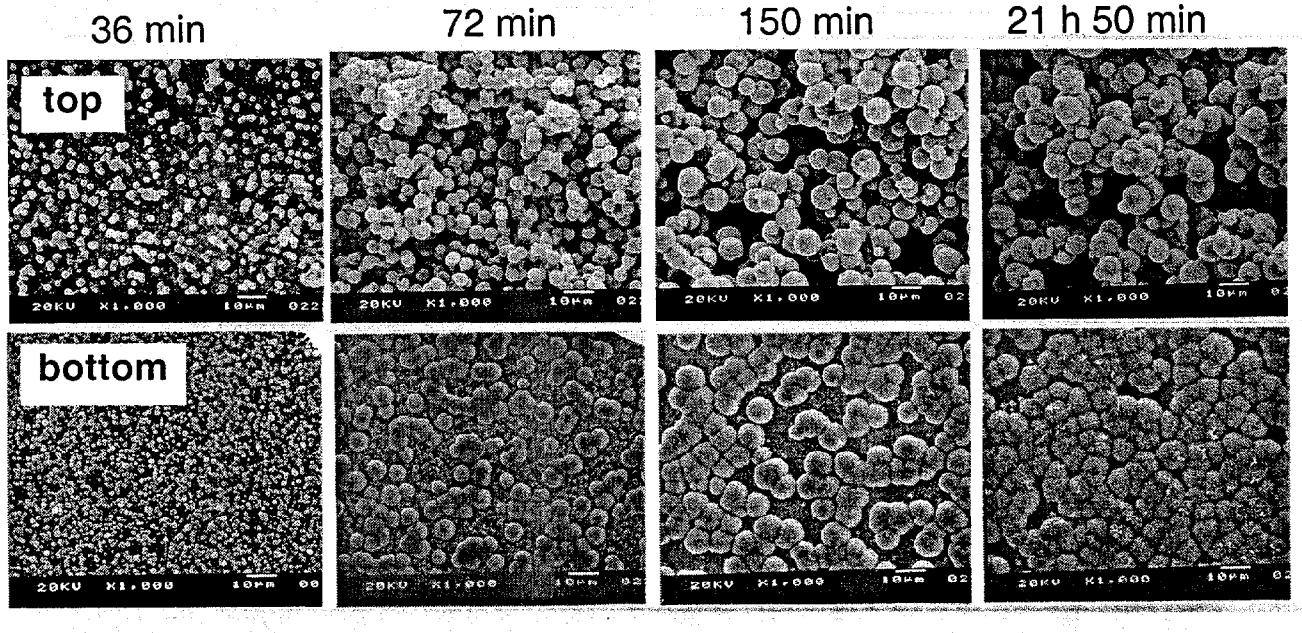

Fig. 3.27. Surface-solid-formation test at 100°C: growth vs time. Upper images are of the top surfaces of the foils; lower images are of the bottom surfaces of the foils.

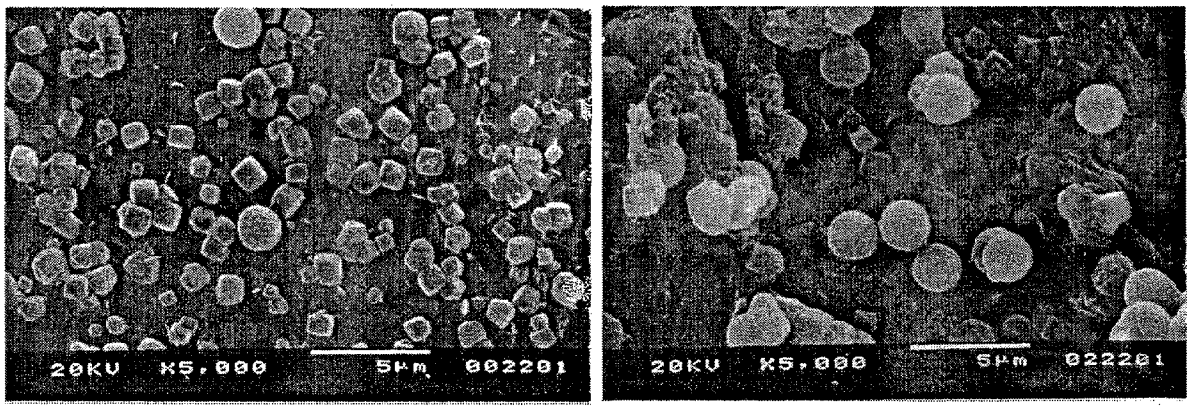

Fig. 3.28. Surface-solid-formation test at 100°C: 36-min sample showing initial surface-grown, cubic-shaped crystals, which transformed into surface microspheres.

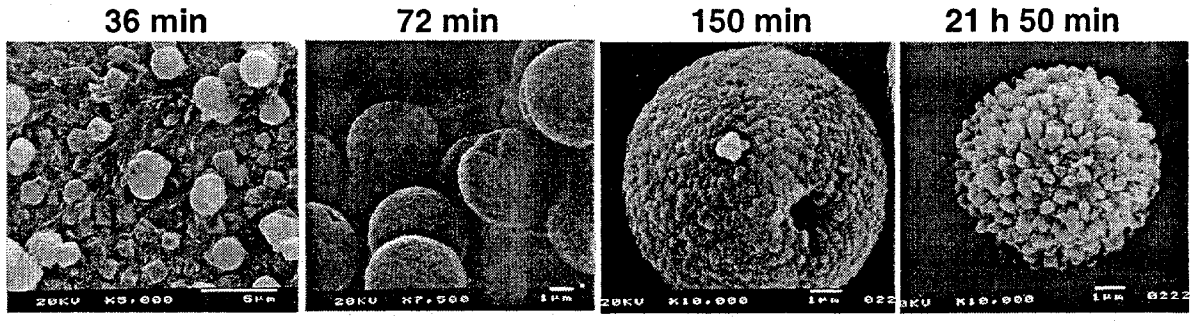

Fig. 3.29. Morphological transformation of settled particles on top side of foil at 100°C.

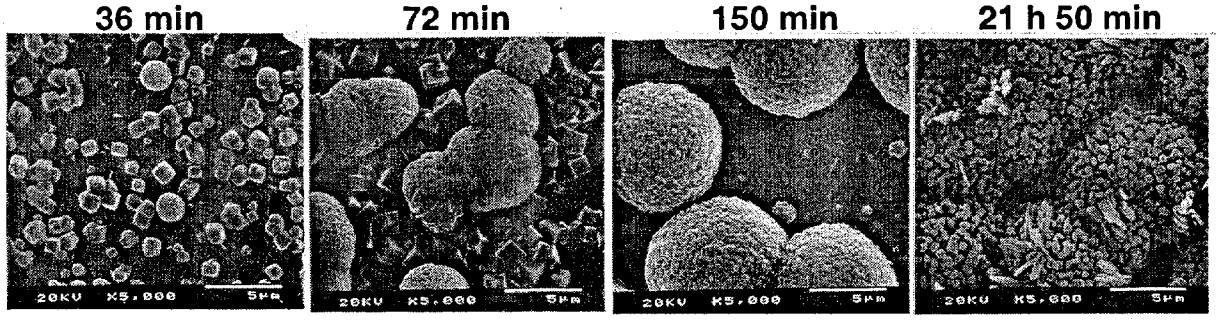

Fig. 3.30. Morphological transformation of "surface-grown" particles on bottom side of foil at 100°C.

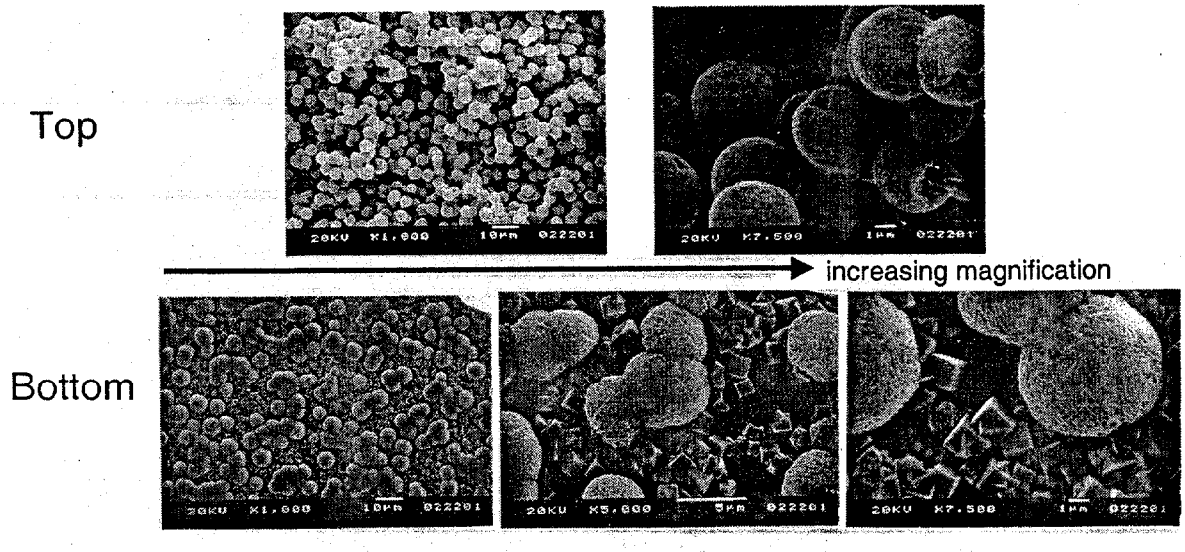

Fig. 3.31. Comparison of morphologies between deposited and "surface-grown" particles for 72-min sample at 100°C.

The following observations may be made from the results of quiescent surface-solid-formation experiments described above:

- Particles can grow at the metal surfaces by a heterogeneous mechanism. The nucleation mechanism for such growth, heterogeneous nucleation at the surface and/or homogeneous nucleation in solution followed by nanoparticle attachment to the surface, is unclear.
- It appears that particle growth in bulk solution and the growth of solids at the surface have similar kinetics under the conditions studied.
- The induction period in bulk solution, as determined by DLS, appears to coincide with the onset time for surface particle growth in these tests.
- Surface solids begin as small particles on the surface and grow larger and thicker, eventually forming a monolayer. The material connecting the particles appears to be as strong as the particle material.
- Precursor depletion in solution appears to stop further solid layer growth. Precursor depletion in these batch tests may also affect solid morphology and phase formation.
- Settled particles appear to grow/fuse together into a connected solid.
- A density gradient exists in the deposit on top of the foil.
- The thick layer of solid deposit (240-min sample) can be peeled off from the foil surface after drying.
- Such layer-type structure seems to indicate that either (a) surface-grown solid material is formed before particle settling, or (b) the deposit may undergo a transition.
- Higher temperatures will accelerate the formation dynamics of surface solids/particles as well as the solids/particles in bulk solution.

3.4.2 Effect of Fluid Flow on the Formation of Surface Solids

To study the effect of solution flow on the formation of solids on foil surfaces (i.e., particle deposition and surface growth of particles), a magnetic stir bar below the foil strip was used to create a rotating flow in the Teflon vessels (see Fig. 3.32). An experiment was performed at 80°C with a solution containing 0.133 *M* silicon and 0.133 *M* aluminum, conditions similar to the quiescent experiment that resulted in the solids shown in Figs. 3.23 and 3.24. Two vessels were used, with one foil removed from solution after 1 h and the other foil after 2 h. Macroscopic images of the top and bottom surfaces of the foils are shown in Fig. 3.32.

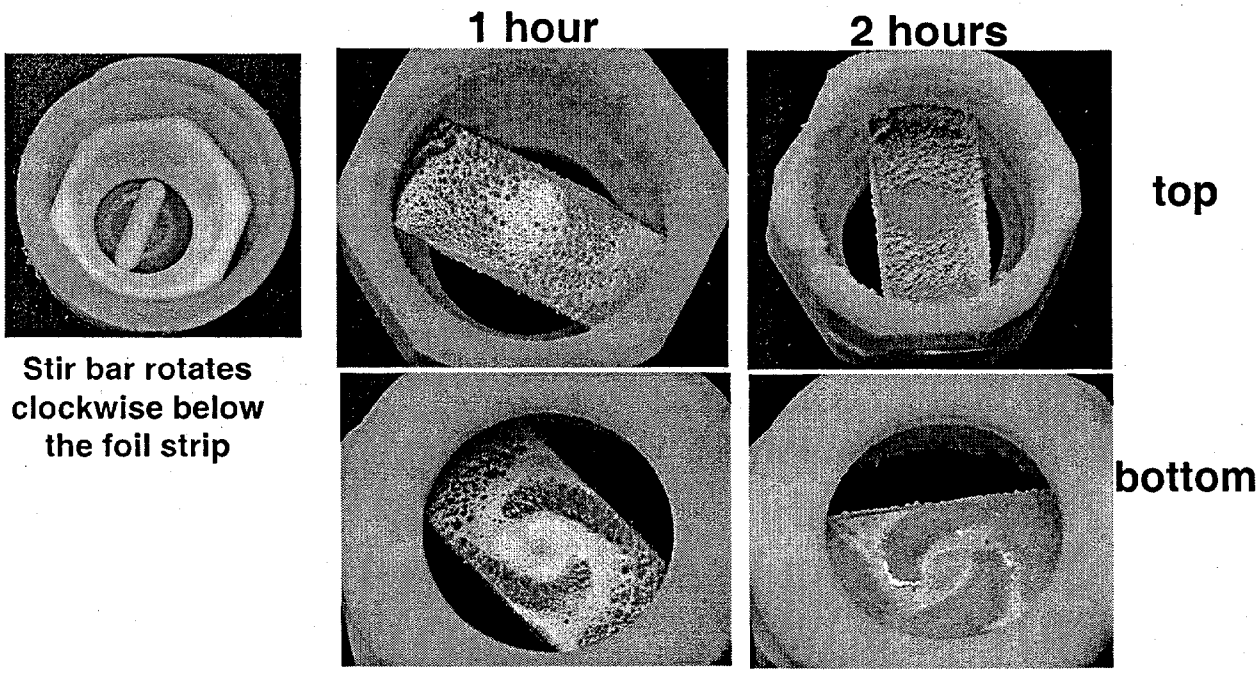

Fig. 3.32. Effect of solution flow on the formation of solid material on stainless steel foils in 0.133 *M* [Si]–0.133 *M* [Al] solution at 80°C.

Several observations can be made from visual inspection of the foils (see Fig. 3.32). Most notable is the fact that significantly more solids were present on the bottom sides of the foils than in the quiescent tests. Unlike the quiescent tests, the solids on the bottom sides of the foils in this stirred test were similar to those on the top sides. Each side had areas coated with a thin, translucent solids layer, while other areas were covered with macroscopic rough, chunky particle deposits. The deposited solids on the foil surfaces were distributed nonuniformly, with patterns that appear to be related to the fluid flow in the vessel. On the bottom side of the foil (the side closer to the stir bar), the solids were deposited in a "galaxy" pattern, while on the top side of the foil, the heaviest deposits formed in a ring, with the fewest particles deposited in the center (the zone with the lowest fluid velocity). The deposited solids were much more strongly adhered to the foil than those that were formed by settling in the quiescent tests.

Results of SEM examination of these samples is shown in Fig. 3.33. The images were collected for both sides of the foils for the areas with the thin, translucent layers ("surface-grown area") and for the areas of particle deposits ("deposited area"). These SEM results show that the microstructure of the solids in each type of area is similar for each side of the foil—that is, the solids in surface-grown areas are similar, and those in the deposited areas are similar. However, the microstructures of the two area types are significantly different and are consistent with surface growth for the thin areas and flow-induced deposition for the thickly deposited areas. It is well known that fluid flow or hydrodynamics affect particle deposition on wall significantly.[12, 13] The surface-grown solids are similar to those from the bottom surfaces of foils in quiescent tests, as evidenced by the formation of solid "mounds" on top of cubic solids. The deposited solids are similar to settled solids from the top surfaces of foils in quiescent tests with two significant differences: (1) the solids appear to be more agglomerated, and (2) the particles are not as homogeneous in size, with finer particles incorporated into the deposits. These findings suggest that the mechanisms of flow-induced deposition are different from those of settling. It may be possible that fluid flow carries the particles to the surface and deposits them into growing surface layers.

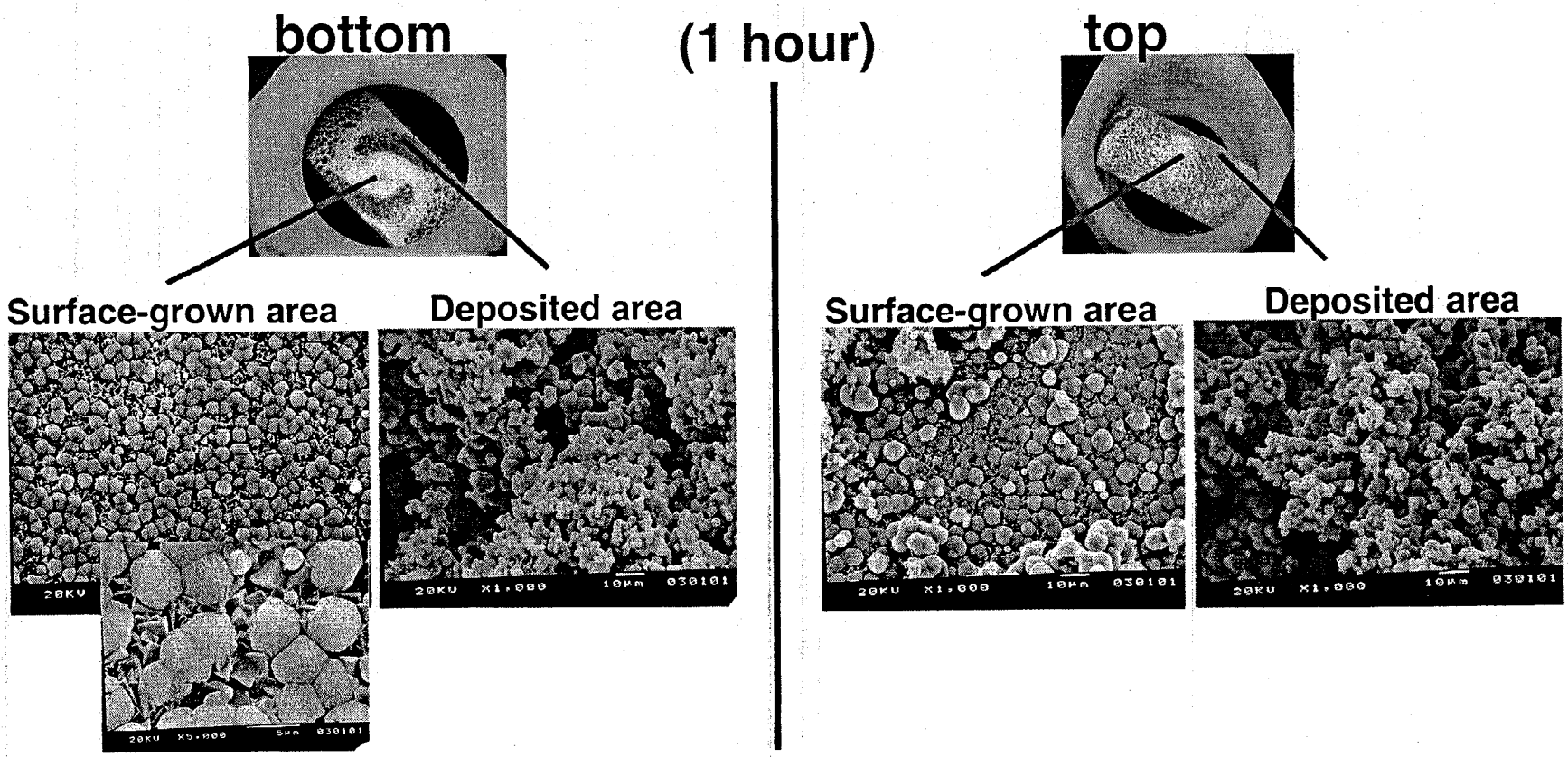

Fig. 3.33. SEM examination of foil surface solids obtained under flow conditions.

This stirred surface-solids-formation test is significant for understanding solids deposition in the 2H evaporator. While it appears that all surfaces may be coated by a surface-growth mechanism, areas of high fluid velocity and/or high shear may be much more susceptible to the deposition of solids to form hard, well-adhered scale. These observations are consistent with the formation of scale in the lift line and gravity drain lines. In addition, the nonuniform distribution of solids on the evaporator walls may also be related to high-velocity zones caused by steam injection into the evaporator at the steam lance. Further investigation of the effect of flow on scale formation is warranted.

3.4.3 Growth of Solids on Existing Solid Films

The deposition tests and SEM studies described above have shown that solid particles will grow on stainless steel surfaces and transform from cubic-shaped particles (probably zeolite A), through microspheres/mounds of "yarn," into spiked microspheres/mounds (probably sodalite). Both "surface growth" and "particle deposition" were found to be responsible for the solid buildup on the surfaces of stainless steel foils. (It is not surprising, since many other processes of solid film growth on substrates in reactive solutions can involve both mechanisms.[14]) Surface growth of the solid layer occurs everywhere. Particle deposition is induced by either particle settling or flow/shear. Dense "surface-grown" layers exist below the deposited solids that are somewhat porous. A remaining question from those tests is whether heterogeneous nucleation or surface growth can occur on an existing aluminosilicate solid surface. Resolution of this question would help clarify the mechanism of how solids can build up further on the wall surface.

An additional test was conducted to examine and determine whether, and by what mechanisms, new solids could grow on an existing layer of scale or on surfaces of already deposited particles. This experiment was conducted by first depositing a layer of aluminosilicate by holding foil samples overnight in five vessels containing 0.1 *M* Si–0.133 *M* Al in 6 *M* Na^+ at 100°C. One foil sample was used as a control to characterize the initial film, while the remaining four foil samples were placed again in new 9-mL batches of solution (0.133 *M* Si–0.133 *M* Al in 6 *M* Na^+) in separate vessels for a second deposition. The latter vessels were held at 100°C, and foil samples were removed from the vessel solution after 36, 72, and 150 min, and 2 days, respectively. By visual observation, the four samples from the second batch appeared similar to those from previous experiments at 100°C; however, both the "surface-grown" layers at the bottom side of the foils and the "deposited" layers on the top side of foils seemed thicker than the bottom and the top of the "control" sample.

SEM examination results for "surface grown" solid are shown in Fig. 3.34. Clearly, on the bottom side of the foil, another solid layer of scale grew on the surface of the existing aluminosilicate layer. This second-layer growth underwent a surface particle morphology (crystalline phase) transformation similar to the initial growth on the foil surface. However, no cubic-shaped crystals were observed on the few samples collected (Fig. 3.34). We plan to run a new set of tests that will allow us to determine whether transitional cubic-shaped crystals exist before the surface solid transforms to the type of material shown in Fig. 3.34(B).

SEM results for "deposited" particles on the top sides of the foils are shown in Fig. 3.35. Significantly, we observed a cubic-shaped crystal on the particle surfaces at an early stage (36-min sample, Fig. 3.35(B)). This seems to indicate a heterogeneous nucleation mechanism. The differences in the observed growth on the top and bottom surfaces in this test may be due to different cube-crystallization kinetics on the different surfaces and in bulk solution; a greater frequency of sampling and more-detailed analysis would be necessary to elucidate the mechanisms.

In summary, as would be expected from other studies of seeded growth of aluminosilicates,[10] this experiment has shown that it is possible for further solid growth (and phase transformation) to occur on an existing aluminosilicate particle/solid surface.

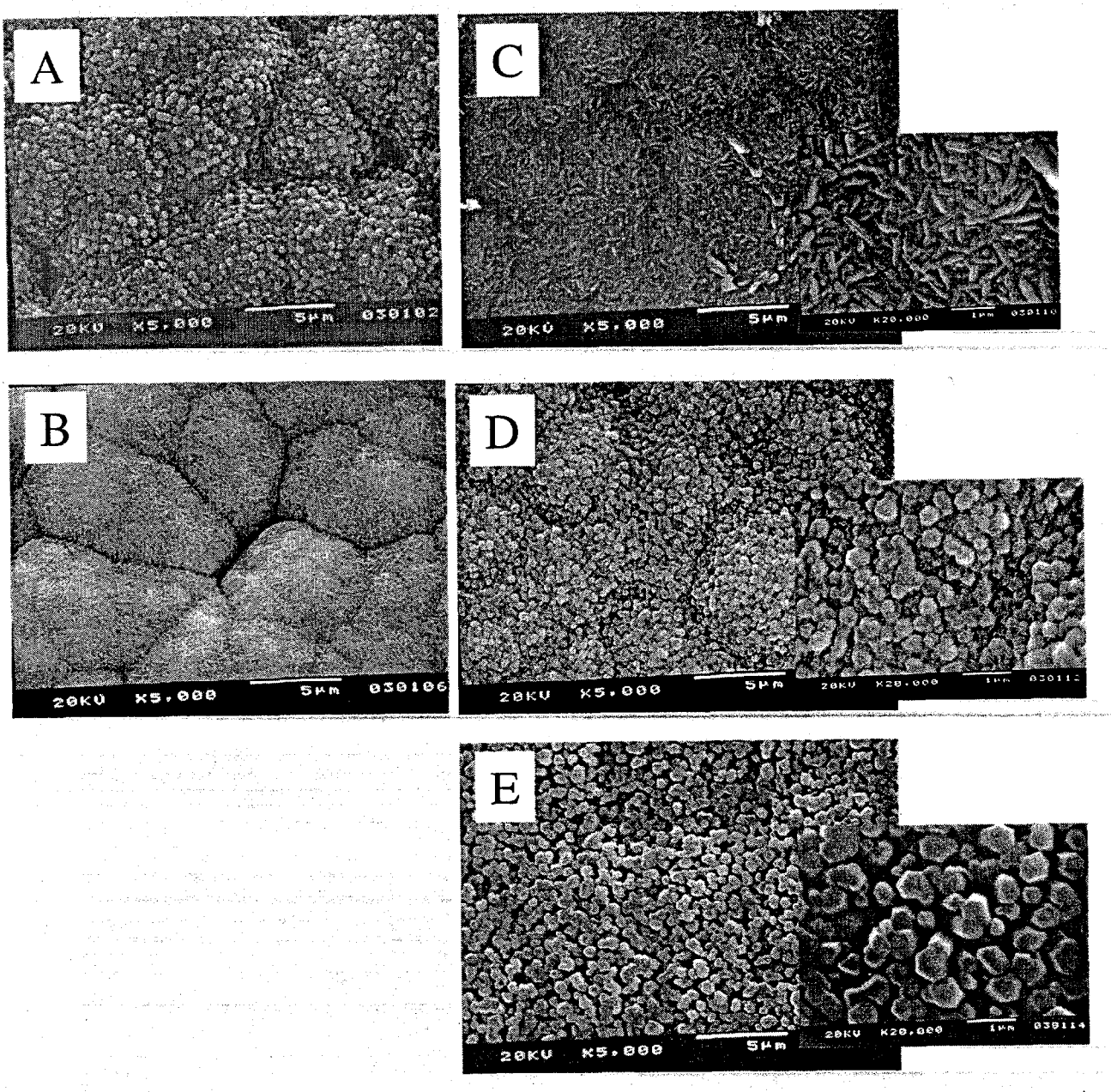

Fig. 3.34. Surface solid growth/evolution on existing solid film—bottom side of foil.
(A) control sample; (B) 36 min; (C) 72 min; (D) 150 min; (E) 2 days.

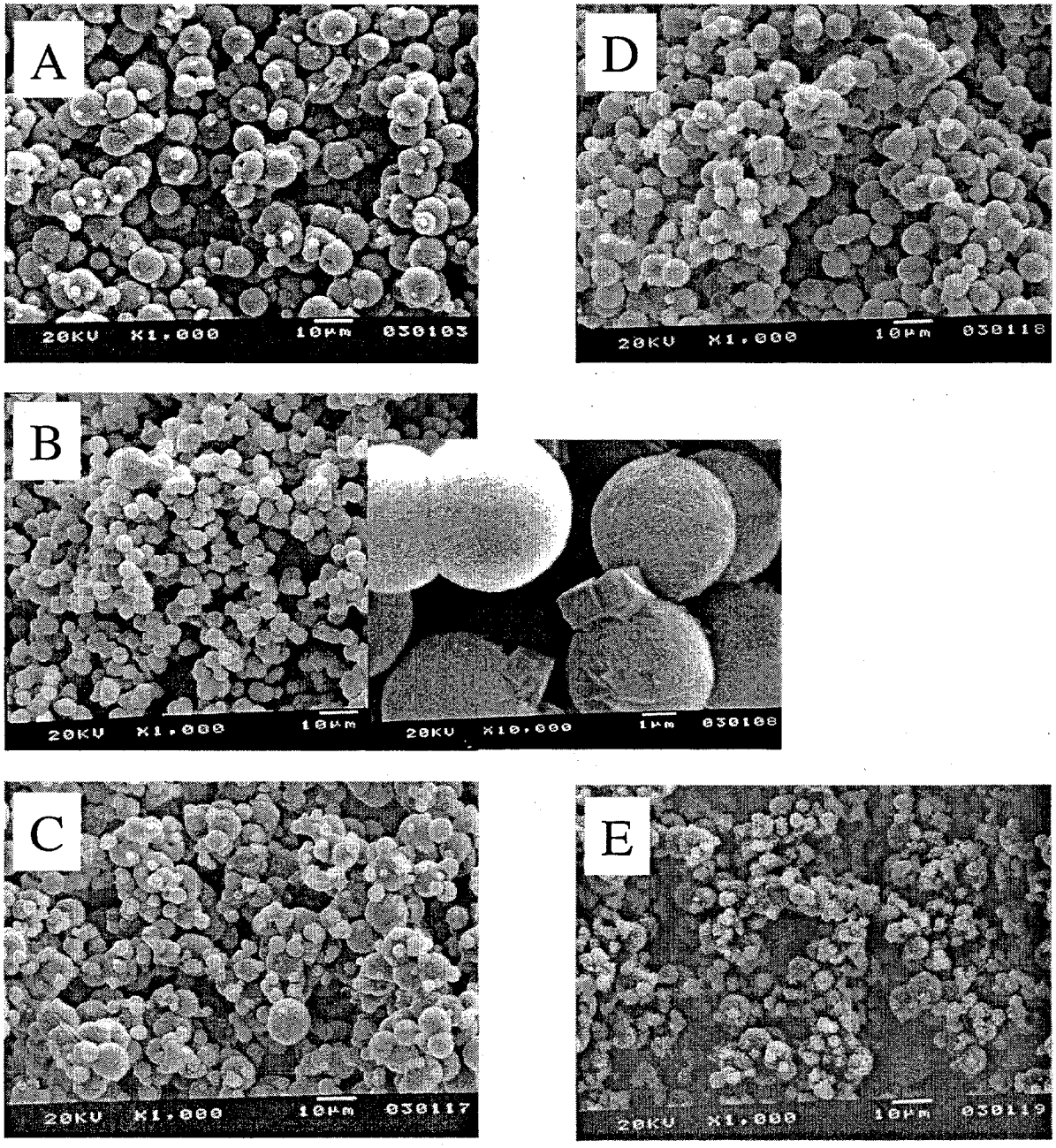

Fig. 3.35. Surface solid growth/evolution on existing solid film—top side of foil. (A) control sample; (B) 36 min; (C) 72 min; (D) 150 min; (E) 2 days.

4. SUMMARY AND RECOMMENDATIONS

4.1 SUMMARY

In this study, we investigated the formation of aluminosilicate solids/particles from caustic (4–6 *M* NaOH) solutions that contained dissolved silicon and aluminum (typically 0.004–0.3 *M*) at elevated temperatures (40–110°C). Solid formation was found to occur both in bulk solutions and on submerged substrate surfaces. The solids underwent a complicated crystalline phase transformation and solid/particle morphology evolution with time. X-ray diffraction (XRD) analyses showed that at equilibrium the aluminosilicate solids were predominantly sodalite with a formula of $Na_8(AlSiO_4)_6(NO_3)_2 \cdot 4H_2O$, whose stoichiometric reactive formation seems to be relatively unaffected by the concentration or the [Si]/[Al] ratio in solution. The bulk solids or scales microscopically resembled aggregated, connected, or fused microspheres within which there were finer, primary crystalline particles. A real-time DLS technique was employed to monitor the particle-growth dynamics (i.e., determination of induction period for solid-phase formation) in quiescent solutions, while SEM was used to examine heterogeneous *surface growth* of particles and formation of surface solids (i.e., scales) on stainless steel surfaces. Process conditions, including temperature, concentrations of silicon and aluminum, reaction time, and hydrodynamics of fluid flow, were studied for their effects on solids formation on surfaces. The major findings were as follows:

(1) A linear relationship holds between log $(1/t_I)$ and $1/T$ (where t_I is the induction period and T is the temperature); the activation energy for aluminosilicate solid-phase formation is ~65 kJ/mol. With an increasing concentration of aluminum, the induction time decreases monotonically. A similar decrease in induction time was noted for increasing silicon concentration; however, for the conditions tested, the induction time did not appear to significantly decrease as silicon concentration was increased above approximately 0.05 *M*.

(2) Both the growth of "surface particles" and the deposition/fusion of "bulk particles" from solutions are attributable to the mechanism of scale formation on clean stainless steel surfaces. Surface particles grow and expand their coverage of substrate surface in a monolayer manner, and this surface-grown monolayer can be a dense, continuous layer between the substrate and the top deposited/fused particles.

(3) During growth, early-stage cubic-shaped particles (probably zeolite A) are consumed/transformed into microsphere-like (in bulk) or mound-like (on surface) particles (probably sodalite). The surface morphologies of both "bulk particles" and "surface particles" evolve with time, changing from needle-like to lumpy—and eventually to spiked-shape—primary particles.

(4) The hydrodynamic flow of solutions significantly affects the deposition/attachment of particles on stainless steel surfaces. While solid films can form on all surfaces by a surface-growth mechanism, it appears that particles from the bulk solution can be deposited in zones of high velocity and/or shear. The deposits in high-shear zones are much thicker and more strongly attached. These results appear to be significant both for determining the causes of scaling and for devising means to minimize scaling.

(5) The surface growth of particles can occur on preexisting aluminosilicate solid surfaces, supporting the conclusion that heterogeneous surface growth of particles, as well as deposition and growth of deposited particles from bulk solution, could be responsible for further buildup of scale.

It should be emphasized that these findings are for laboratory-scale experiments with simulant solutions at reaction conditions (temperature, composition, etc.) that do not precisely match the process conditions in the 2H evaporator. While these experimental results shed some light on the processes involved in the formation of scale in the 2H evaporator, it is possible there are other contributing factors not simulated in the laboratory.

4.2 RECOMMENDATIONS FOR FUTURE WORK

Based on the results of this work, several topics that are recommended for future experiments to develop greater understanding of the factors contributing to scale formation in waste evaporators. Among these are the following:

- Further dynamic-light-scattering studies are recommended to include other conditions, such as:
  - higher temperatures, approaching ~120-130°C conditions in the evaporator, and more-concentrated simulant solutions (while such work would be more difficult to perform, it would yield information that would be valuable in comparing reaction rates with characteristic times for fluid transport and mixing in the evaporator);
  - shear-induced aggregation in bulk; and
  - the influence of seed particles and/or inhibitors on solids formation.
- Further studies of solids formation at surfaces are recommended, designed for the purposes of determining
  - the effect of flow velocity on surface growth and particle deposition;
  - the solids distribution and growth kinetics between surface-grown solids and particles in solution;
  - the effect of surface-modifying agents on surface growth;
  - "surface-particle" phase evolution/transformation; and
  - the effects of engineering approaches, such as ultrasonication, to minimizing particle deposition.

Such investigations would not only provide a greater understanding of the processes but would also allow us to move toward a possible solution to the problem associated with deposit/scale formation.

During Phase II studies in the remainder of FY 2001, our experimental studies will be aimed at (1) measuring particle-particle and particle-surface interaction forces in high-ionic-strength, high-caustic solutions and (2) investigating the effect of fluid hydrodynamics (flow and shear) on the deposition of solids on metal surfaces.

REFERENCES

1. W. R. Wilmarth, C. J. Coleman, J. C. Hart, and W. T. Boyce, *Characterization of Samples from the 242-16H Evaporator Wall*, WSRC-TR-2000-00089, Savannah River Technology Center, Aiken, S.C., March 20, 2000.

2. W. R. Wilmarth, S. D. Fink, D. T. Hobbs, and M. S. Hay, *Characterization and Dissolution Studies of Samples from the 242-16H Evaporator Gravity Drain Line (U)*, WSRC-TR-97-0326, Rev. 0, Savannah River Technology Center, Aiken, S.C., October 16, 1997.

3. L. O. Dworjanyn et al., Savannah River Technology Center, personal communication, May 1, 2001.

4. W. R. Wilmarth, S. D. Fink, D. T. Hobbs, and M. S. Hay, *Characterization and Dissolution Studies of Samples from the 242-16H Evaporator Gravity Drain Line (U)*, WSRC-TR-97-0326, Rev. 0, Savannah River Technology Center, Aiken, S.C., October 16, 1997.

5. A. J. Mattus, C. H. Mattus, and R. D. Hunt, *Kinetic Testing of Nitrate-Based Sodalite Formation Over the Temperature Range of 40 to 100°C*, ORNL/TM-2001/117 (Draft), Oak Ridge National Laboratory, Oak Ridge, Tenn., April 13, 2001.

6. M. Z. Hu, M. T. Harris, and C. H. Byers, "Nucleation and Growth for Synthesis of Nanometric Zirconia Particles by Forced Hydrolysis," *J. Colloid Interface Sci.* **198**, 87–99 (1998).

7. M. Z. Hu, E. A. Payzant, and C. H. Byers, "Sol-Gel and Ultrafine Particle Formation via Dielectric Tuning of Inorganic Salt–Alcohol–Water Solutions," *J. Colloid Interface Sci.* **222(1)**, 20–36 (2000).

8. P. C. Hiemenz, and R. Rajagopalan, *Principles of Colloid and Surface Chemistry*, 3rd ed., Marcel Dekker, Inc., New York, 1997.

9. J. Addai-Mensah, *Sodium Aluminosilicate Scale Formation in Westinghouse Savannah River Company 2H Evaporation Process*, Report No. 1 of Westinghouse Savannah River Company subcontract AC18106S, Ian Wark Research Institute, University of South Australia, Mawson Lakes, Adelaide, Australia, May 18, 2001.

10. M. C. Barnes, J. Addai-Mensah, and A. R. Gerson, "The Kinetics of Desilication of Synthetic Spent Bayer Liquor and Sodalite Crystal Growth," *Colloids and Surfaces A: Physicochemical and Engineering Aspects* **147**, 283–95 (1999).

11. M. C. Barnes, J. Addai-Mensah, and A. R. Gerson, "The Kinetics of Desilication of Synthetic Spent Bayer Liquor Seeded with Cancrinite and Cancrinite/Sodalite Mixed-Phase Crystals," *J. Crystal Growth* **200**, 251–64 (1999).

12. P. Warszynski, "Coupling of Hydrodynamic and Electric Interactions in Adsorption of Colloidal Particles," *Ad. Colloid Interface Sci.* **84**, 47–142 (2000).

13. Z. Adamcyk, P. Warszynski, L. Szyk-Warszynska, and P. Weronski, "Role of Convection in Particle Deposition at Solid Surfaces," *Colloids and Surfaces A: Physicochemical and Engineering Aspects* **165**, 157–87 (2000).

14. H. Shin, M. Agarwal, M. R. De Guire, and A. H. Heuer, "Deposition Mechanism of Oxide Thin Films on Self-Assembled Organic Monolayers," *Acta Mater.* **46**, 801–15 (1998).

6. APPENDIXES

Appendix A

SIMULANT SOLUTIONS FOR 2H EVAPORATOR

Appendix A. SIMULANT SOLUTIONS FOR 2H EVAPORATOR

I. Test Solutions Containing 0.133 *M* Aluminum and Variable Silicon Concentrations

Several precursor solutions were prepared for this study such that their mixture would maintain relatively fixed concentrations of aluminum (0.144 *M*), sodium (6.6 *M*), hydroxide (4 *M*), nitrate (1.4 *M*), and nitrite (1.0 *M*). These fixed concentrations were similar to those observed for median values in samples taken from SRS Tank 43H. The silicon concentration was then varied between 0.004 and 0.15 *M*. The compositions of precursor solutions for this testing are summarized below.

Solution A:

	mol/L
NaOH	4.00
$NaNO_3$	1.00
$NaNO_2$	1.00
$Al(NO_3)\cdot 9H_2O$	0.133
Total Na^+	6.00
Total OH^-	4.00
Total NO_3^-	1.399
Total NO_2^-	1.00
Total Al^{3+}	0.133

Solution B:

NaOH	6 *M*
Silica Frit 200	20 g/L
Si	0.2 *M*
Final OH^-	5.53 *M*

Solution 2A:

	mol/L
NaOH	3.00
$NaNO_3$	2.00
$NaNO_2$	2.00
$Al(NO_3)\cdot 9H_2O$	0.266
Total Na^+	7.00
Total OH^-	3.00
Total NO_3^-	2.798
Total NO_2^-	2.00
Total Al^{3+}	0.266

Solutions A and 2A were prepared by first dissolving the solid NaOH in nanopure water. Once the solution had cooled to room temperature, aluminum nitrate was added and dissolved. After compete dissolution of the aluminum salt, sodium nitrate was dissolved followed by sodium nitrite. The final solution was brought to volume with nanopure water.

Solution B was prepared by dissolving 240 g sodium hydroxide (EM Science) in 800 mL of deionized water in a 1200-mL stainless steel beaker. Twenty grams of SRS glass Frit 200 was then added; a Teflon-coated stirring bar was inserted to disperse the frit. A water-cooled condenser column was attached to a stainless steel top and used to cover the beaker during heating. The solution was boiled under reflux for 20 h. The cooled solution was filtered through a Whatman No. 1 paper filter into a Nalgene 1-L volumetric flask and make up to 1000 mL with nanopure water.

Simulant samples were prepared by adding solid sodium hydroxide and aluminum nitrate to various volume ratios of precursor Solutions A and 2A according to Table A.1. As shown in Table A.1, 3-mL milliliter samples were prepared in the optical cell of the light-scattering experiment by adding from 2.96 to 0.75 mL combined A+2A solution to the cell. The remainder of the 3-mL volume was made up by the addition of Solution B to initiate the precipitation reaction.

II. Solutions Containing 0.05 *M* Silicon and Variable Aluminum Concentrations

Similarly, several precursor solutions were prepared such that their mixture would maintain relatively fixed concentrations of silicon (0.05 *M*), sodium (6.6 *M*), hydroxide (4 *M*), nitrate (1.4 *M*), and nitrite (1.0 *M*). The aluminum concentration was then varied between 0.04 and 0.3 *M*. The compositions of precursor solutions are summarized below.

Simulant samples were prepared by adding solid sodium hydroxide and sodium nitrate to various volume ratios of precursor D and 2D solutions. As shown in Table A.2, 3-mL samples were prepared in the optical cell of the light-scattering experiment by adding from 2.85 to 1.5 mL of combined D+2D solution to the cell. The remainder of the 3-mL volume was made up by adding Solution E to initiate the precipitation reaction.

Solution D: (6 *M* Na^+ formulation)

	mol/L
NaOH	2.62
$NaNO_3$	0.02
$NaNO_2$	1.00
Si	0.05
Total Na^+	5.14
Total OH^-	4.00
Total NO_3^-	0.1
Total NO_2^-	1.00
Total Al^{3+}	0.05

Solution 2D: (6 *M* Na^+ formulation and 3 *M* NaOH)

	mol/L
NaOH	0.23
$NaNO_3$	0.20
$NaNO_2$	2.00
Si	0.10
Total Na^+	5.43
Total OH^-	3.23
Total NO_3^-	0.20
Total NO_2^-	2.00
Total Al^{3+}	0.10

Solution E:

Total Na^+	5.5 *M*
$Al(NO_3)\cdot 9H_2O$	0.60 *M*
Total OH^-	3.10 *M*
Total NO_3^-	1.80 *M*

Table A.1. Mixture of precursor Solutions A, 2A, and B for variable [Si] experiments

	Final silica concentration (*M*)							
	0.004	0.01	0.025	0.05	0.075	0.1	0.133	0.15
Solution A blend (100 mL)								
ML Solution A	96	90	75	50	25	0	0	0
mL Solution 2A	2	5	12.5	25	37.5	50	33.5	25
g NaOH	2.09	2.02	1.86	1.59	1.33	1.06	0.00	0.00
g $Al(NO_3)_3 \cdot 9H_2O$	0.00	0.00	0.00	0.00	0.00	0.00	1.65	2.49
Solution A blend contains:								
Total Na	6.55	6.58	6.67	6.86	7.13	7.53	7.00	7.00
Free OH	3.97	3.92	3.78	3.49	3.08	2.47	1.41	0.87
Total NO_3	1.43	1.47	1.60	1.87	2.24	2.80	3.19	3.60
Total NO_2	1.02	1.05	1.14	1.33	1.60	2.00	2.00	2.00
Total Al	0.136	0.140	0.152	0.177	0.213	0.266	0.397	0.532
To make 3 mL of sample mix:								
mL A blend	2.94	2.85	2.63	2.25	1.88	1.50	1.01	0.75
mL Solution B	0.06	0.15	0.38	0.75	1.13	1.50	2.00	2.25
3 mL of sample mix contains:								
Total Na	6.54	6.56	6.59	6.65	6.71	6.76	6.34	6.25
Free OH	4.00	4.00	4.00	4.00	4.00	4.00	4.15	4.37
Total NO_3	1.40	1.40	1.40	1.40	1.40	1.40	1.07	0.90
Total NO_2	1.00	1.00	1.00	1.00	1.00	1.00	0.67	0.50
Total Al	0.133	0.133	0.133	0.133	0.133	0.133	0.133	0.133
Si/Al ratio	0.03	0.08	0.19	0.38	0.56	0.75	1.00	1.13
Solution density (g/mL) at 25°C	1.2522		1.2468		1.2574			1.2168

Table A.2. Mixture of precursor Solutions D, 2D, and E for variable [Al] Experiments

	Final aluminum concentration (*M*)							
	0.03	0.04	0.05	0.1	0.15	0.2	0.25	0.3
Solution D Blend								
mL Solution D	90.0	86.7	83.3	66.7	50.0	33.3	16.7	0.0
mL Solution 2D	5.0	6.7	8.3	16.7	25.0	33.3	41.7	50.0
g NaOH	0.36	0.48	0.60	1.20	1.80	2.40	3.00	3.60
mL Solution B	0.00	0.00	0.00	0.00	0.00	0.00	0.00	0.00
g $NaNO_3$	6.89	6.63	6.38	5.10	3.83	2.55	1.28	0.00
Solution D blend contains:								
Total Na	6.10	6.12	6.15	5.56	5.84	6.18	6.63	7.23
Total OH	4.05	4.07	4.09	4.21	4.34	4.52	4.74	5.03
Total NO_3	0.96	0.94	0.93	0.84	0.73	0.60	0.43	0.20
Total NO_2	1.05	1.07	1.09	1.20	1.33	1.50	1.71	2.00
Total Si	0.053	0.054	0.055	0.060	0.067	0.075	0.086	0.100
To make 3 mL of sample mix:								
mL D blend	2.85	2.80	2.75	2.50	2.25	2.00	1.75	1.50
mL E Solution	0.15	0.20	0.25	0.50	0.75	1.00	1.25	1.50
3 mL of sample mix contains:								
Total Na	6.07	6.08	6.09	5.55	5.75	5.96	6.16	6.37
Total OH	4.01	4.01	4.01	4.02	4.03	4.04	4.06	4.07
Total NO_3	1.00	1.00	1.00	1.00	1.00	1.00	1.00	1.00
Total NO_2	1.00	1.00	1.00	1.00	1.00	1.00	1.00	1.00
Total Si	0.050	0.050	0.050	0.050	0.050	0.050	0.050	0.050
Total Al	0.030	0.040	0.050	0.100	0.150	0.200	0.250	0.300
Si/Al ratio	1.667	1.250	1.000	0.500	0.333	0.250	0.200	0.167
Solution density (g/mL) at 25°C	1.2016			1.2176		1.2320		1.2420

III. Titration of Free OH^- in Dissolved Frit Solution B

Background. The calculated concentration of free hydroxide in SRS Frit 200 dissolved in 6 *N* NaOH is 5.6 *M*. Similarly, the calculated concentration of free hydroxide for frit dissolved in 4 *N* NaOH is 3.6 *M*.

The calculations assume that 20 g of Frit 200 will be dissolved in 1 L of caustic and that the frit is made of 70% SiO_2. Initial dissolution of SiO_2 is governed by the following equation:

$$SiO_2 + 2\ NaOH \rightarrow Na_2SiO_3 + H_2O.$$

Subsequent polymerization reactions were not considered in the calculation of free hydroxide since the extent of the reaction in each case are unknown. Boron oxide is present at 20% in the frit, dissolving according to the following equation:

$$B_2O_3 + 2\ NaOH + 3\ H_2O \rightarrow 2\ B(OH)_4^- + 2\ Na^+.$$

This reaction was not taken into account in the calculation due to the lower concentration of boron in the frit.

The free hydroxide concentration was determined experimentally by titration with standard 1 *N* HCl using a programmable autotitrator (Brinkman Model Titrino 716). This instrument was programmed to provide acid volumes required to reach pH 7 and pH 3.4. The second pH value was selected because it is the pK_a for the pH indicator, methyl orange, used in the determination of free hydroxide in the analysis of dissolved silicates for industrial use (*Encyclopedia of Industrial Chemical Analysis*, Volume 18, pp. 44–25, F. D. Snell and L. S. Ettre, eds., Interscience Publishers, New York, 1973). The titrator was programmed to identify any other significant breaks in the titration curve that might represent titration of silicon hydroxide species.

Procedure. The following parameters were used to set up the titration method:

(a) Press Mode key until Det is selected; then enter.
(b) Select pH and enter, followed by pressing the Parameters key.
(c) Select "titration parameters" and then enter. Set up the following parameters:
Point density = 1; titration max. rate = 1 mL/min; minimum volume increment = 5 µL;
Pause = 30 s; temperature = 24.5 °C; volume stop = 10 mL; stop pH = 1.9; stop end points = 5; fix EP1 @ pH 7; fix EP2 @ pH 3.4; fix EP3 @ pH 2. Press Quit key twice to exit the titration parameter subroutine.
(d) Set up the printer by pressing Def key twice for "report"; then push Select key three times, followed by Enter to get a "full" titration report. Press Def key three times for report; use Select key to get a printout of the titration curve.
(e) Tare an empty Erlenmeyer flask on a balance. Add 0.5 mL of dissolved Frit sample to the flask, and determine the weight of the sample. Add about 150 mL of nanopure water.
(f) Press Start key once the pH electrode, titrant delivery tube, and magnetic stirrer have been added to the flask.

Results. Free hydroxide concentration was reported on a volume basis of a 0.5-mL sample and on a weight basis. In the latter case, the densities of the 6 *N* and 4 *N* NaOH Frit solutions were taken to be 1.22 and 1.16 g/mL, respectively.

Sample: Dissolved silica frit in 6 *N* NaOH (SFS1 preparation, A. J. Mattus)

	Concentration of OH^- (*M*)			
	Volumetric		Gravimetric	
pH end point	pH 7	pH 3.4	pH 7	pH 3.4
Trial 1	5.58600	5.89	5.74323	6.05579
Trial 2	5.67400	------	5.82684	-------
Trial 3	5.82000	6.006	5.83531	6.02179
Average	5.693	5.948	5.802	6.039
Standard deviation	0.118	0.082	0.051	0.024

Sample: Dissolved silica frit in 4 *N* NaOH (SFS2 preparation, A. J. Mattus)

	Concentration of OH^- (*M*)			
	Volumetric		Gravimetric	
pH end point	pH 7	pH 3.4	pH 7	pH 3.4
Trial 1	3.91600	4.058	4.01499	4.16058
Trial 2	4.01400	4.168	4.08084	4.23741
Trial 3	3.99400	4.142	3.95446	4.10099
Average	3.975	4.123	4.017	4.166
Standard deviation	0.052	0.057	0.063	0.068

Sample: Dissolved silica frit in 4 *N* NaOH (SFS3 preparation, A. J. Mattus)

	Molar concentration of OH^- (*M*)			
	Volumetric		Gravimetric	
pH end point	pH 7	pH 3.4	pH 7	pH 3.4
Trial 1	3.80200	3.97	3.91541	4.08842
Trial 2	3.89200	4.028	3.92653	4.06373
Trial 3	3.83200	3.976	3.92055	4.06788
Trial 4	3.93400	4.074	3.92993	4.06979
Average	3.865	4.012	3.923	4.072
Standard deviation	0.059	0.049	0.006	0.011

Conclusions. Data based on an fixed end point of pH 7 came closest to the calculated value for free hydroxide, particularly for the 6 *N* NaOH sample. However, free hydroxide concentration in the 4 *N* NaOH samples were elevated by 0.3 *M* hydroxide as compared with the calculated hydroxide concentration. Data based on a fixed pH 3.4 (methyl orange) end point overestimated free hydroxide by 2% as compared with pH 7 calculations. The standard deviation of the analysis was typically within 2%. Volumetric results were consistently lower, by 0.5%, than those based on gravimetry. The titrator located end points at pH 10.6 and pH 6, although no discernable breaks were observed in the plotted titration curve.

Appendix B

BOILING-POINT DETERMINATION OF SIMULANT SOLUTIONS

Appendix B. BOILING-POINT DETERMINATION OF SIMULANT SOLUTIONS

Procedure. Two simulant samples were prepared using SRS Solution A (2/2/01), SRS Solution 2A (2/2/01), and SRS Solution B (SFS1, A. J. Mattus).

Sample 2/05/01 Mix A:	24 mL Solution A 0.5 mL Solution 2A 0.59 g NaOH 0.5 mL Solution B (Si/Al = 0.03; [Si] = 0.004 *M*; [Al] = 0.133 *M*)
Sample 2/05/01 Mix B:	8.375 mL Solution 2A 16.62 mL Solution B 0.414 g $Al(NO_3)_3 \cdot 9H_2O$ (Si/Al = 1.0; [Si] = 0.133 *M*; [Al] = 0.133 *M*)

Each 25-mL sample was placed in a Pyrex 50-mL beaker to which a Teflon magnetic stirring bar was added, and the beaker was covered with a watch glass. The 2/05/02 Mix B sample "bumped" considerably during the boiling of the sample because of the large volume of solids that tended to collect at the bottom of the beaker. The temperatures of the solutions were measured at the onset of boiling using a digital thermometer.

Results. Boiling points were: Sample 2/05/01 Mix A: 110.4°C

Sample 2/05/01 Mix B: 109.2°C

The daily barometric pressure was 29.09 in. Hg (738.9 mm). Mix A remained clear throughout the test; Mix B formed a precipitate within a few minutes of being heated.

Appendix C

COMPATIBILITY TESTING OF 6 *N* NaOH IN QUARTZ CUVETTE CELLS

Appendix C. COMPATIBILITY TESTING OF 6 N NaOH IN QUARTZ CUVETTE CELLS

Purpose: The primary component of SRS H2 tank simulant is sodium hydroxide. Precipitate formation in the simulant was monitored optically at temperatures ranging from ambient to 120°C. Scoping tests were performed to determine whether quartz optical cells are chemically resistant to 6 *N* NaOH at elevated temperatures. The optical absorbance of the cell prior to NaOH contact was compared with that after alkaline treatment at elevated temperatures to determine whether any change in opacity would skew particle testing results.

Procedure: Two quartz cells (Reference 1 and Reference 2) containing water were used to set the baseline of the UV/Vis scanning spectrometer over the 190- to 900-nm range. A third quartz cell (sample 1) was scanned over this wavelength range when containing water and then 6 *N* NaOH. The cell containing 3 mL of 6 *N* NaOH and sealed with a Teflon cap was then heated in a drying oven. The cell was removed occasionally to determine its opacity over a specific period of time.

Equipment: Lambda EZ210 Version 2550 Rev 01 software was used to control a Perkin Elmer EZ210 scanning spectrophotometer. The wavelength was scanned from 900 to 190 nm at 100 nm/min using a slit width of 2 nm. The system was baseline corrected with 1-cm quartz reference cells in the optical paths. Absorbance data were reported every 10 nm.

Preparation of 6 N NaOH
A total of 12.0247 g of solid NaOH (EM Science, Lot 32150303) was added to a 50-mL volumetric flask and diluted with nanopure water. When the solution had cooled, it was brought to 50-mL volume.

Results:

1. Sample 1 cell is a 1-cm fluorescence cell with a plug Teflon cap. After determination of the initial optical absorbance with water, and then 3.5 mL of 6 *N* NaOH, the cell was placed in a drying oven at 81°C at noon on December 20, 2000 and taken out on January 02, 2001. Because of the tight seal from the plug, solution expansion cracked the cell along one edge. Most of the caustic had leaked out; some had dried and etched the interior cell walls. The cell was then washed and filled with water. The absorbance over the 400- to 700-nm range had increased by approximately 0.05 optical density unit (ODU).

2. The absorbance of sample 2 cell (quartz, fluoresence, 1 cm, rectangular cap) was determined when filled first with water and then with 3.0 mL of 6 *N* NaOH. The absorbance did not exceed 0.001 ODU. Tape was used to affix the Teflon cap to the top of the cell prior to placing it in the drying oven at 81°C from noon on January 11, 2001 until noon on January 18, 2001. The final volume in the cell after being heated was approximately 1.3 mL. The caustic was transferred to a 10-mL volumetric flask. The sides of the cell were rinsed three times with nanopure water; the rinsates were transferred to the flask before the volume was brought to 10 mL. The solution was submitted for silicon analysis by inductively coupled plasma (ICP) spectrometry. The cell was filled with water, and the optical absorbance was measured over the 190- to 900-nm range. The absorbance ranged from –0.001 to –0.012 ODU relative to an unheated quartz cell over the 400- to 700-nm range. The absorbance was then determined when filled with 6 *N* NaOH. The absorbance ranged from –0.002 to –0.007 ODU over the 400- to 700-nm range; however, the cell began leaking with the introduction of the caustic.

3. The absorbance of sample 3 cell (borosilicate, two-sided, 1 cm, rectangular cap, cracked in upper body) was determined when filled with water and found to be $\leq$0.001 ODU. The cell was then filled with 2 mL of 6 *N* NaOH and capped. Since there was a slow leak in the cell, the absorbance was not measured in order to protect the spectrometer. Tape was used to affix the Teflon cap to the top of the cell prior to placing it in the drying oven at 81°C from noon on January 11, 2001 until noon on January 18, 2001. Following the heating period the sides looked hazy; all caustic had leaked from the cell. The cell was

rinsed and then filled with water. The absorbance did not exceed 0.007 ODU over the 400- to 700-nm range. The absorbance was determined again when filled with 6 N NaOH and found to exceed 0.145 ODU over the 400- to 700-nm range. The cell leaked at the seams with the introduction of either water or caustic.

4. Results for 01/23/01: ICP analysis of NaOH solution from 5-day contact in cell 2 showed 0.1 g of silicon dissolved from the cuvette to produce a silicon concentration of 0.1 g/3 mL NaOH, or 1.26 *M* silicon in the cell.

5. Results for 01/23/01 – 1/31/01: Silica leaching of cell 4 (Starna Cell, 29F-Q-10, micro fluorimeter cell, quartz '6Q', no fused edges, plug cap, 2-mL volume, 1-cm light path) was tested by adding 6 *N* NaOH to the cell for various lengths of times. As with the previous cells, cell 4 was cleaned by immersing it in ~0.5 *M* HNO_3 and heated for 1 h ~ 50°C. The cell was rinsed sucessively with nanopure water and 6 *N* NaOH. Finally, it was filled with 1 mL of 6 *N* NaOH for testing. After contact, the NaOH was quantitatively removed, diluted to 10 mL with nanopure water, and submitted for ICP analysis of silicon. The following samples were generated:

Long-Term Exposure (0–9 h cumulative)

Sample	Temp. (°C)	6 *N* NaOH (mL)	Time		Contact time (h)	ICP [Si] (μg/mL)	[Si] in cell (*M*)
			Start	Finish			
Cell 4-25-1	24.5	1.25	1/23, 12:00	1/23, 1:00	1	2.3 ± 0.1	0.0008
Cell 4-81-1	81	1.0	1/23, 1:00	1/23, 2:00	1	40 ± 0.7	0.0174
Cell 4-81-2	81	1.0	1/24, 8:00	1/24, 9:00	1	37 ± 1	0.0161
Cell 4-81-4	81	1.0	1/24, 9:15	1/24, 10:55	2	72 ± 1	0.0313
Cell 4-81-6	81	1.0	1/30, 8:15	1/30, 10:15	2	72 ± 0.7	0.0313
Cell 4-81-8	81	1.0	1/30, 10:30	1/30, 12:30	2	92 ± 3.5	0.0400
6 *N* NaOH	---	1.5	---	---	0	0.8 ± 0.1	0.0002

6. Results for 02/02/01: Silica leaching of cell 4 (Starna Cell, 29F-Q-10, micro fluorimeter cell, quartz '6Q', no fused edges, plug cap, 2-mL volume, 1-cm light path) was tested by adding 6 *N* NaOH to the cell for short (up to 1 h) times. The cell was filled with 1 mL of 6 *N* NaOH for testing. After contact, the NaOH was quantitatively removed, diluted to 10 mL with nanopure water, and submitted for ICP analysis of silicon. The following samples were generated:

Short-Term Exposure (0–1 h cumulative)

Sample	Temp. (°C)	6 *N* NaOH (mL)	Time		Contact time (min)	ICP [Si] (μg/mL)	[Si] in cell (*M*)
			Start	Finish			
Cell 4-25-1B	24.5	1.0	12:45	1:45	60	2.7 ± 0.1	0.0009
Cell 4-81-0.25	81	1.0	9:15	9:30	15	6.7 ± 0.1	0.0029
Cell 4-81-0.5	81	1.0	9:45	10:15	30	20 ± 0.4	0.0087
Cell 4-81-0.75	81	1.0	10:30	11:15	45	35 ± 0.8	0.0152

Conclusions: The silicon content in the cell did not appear to increase when the quartz cell was contacted with caustic at room temperature. However, within the first 15 min of exposure to 6 *N* NaOH at 80°C, the [Si] concentration in the cell was 75% of the value of the lowest silicon concentration (0.004 *M*) to be used in the testing of SRS simulants. A 2-h contact with caustic resulted in ten times the lowest silicon concentration to be studied. The amount of silica in solution was not affected by cumulative exposure time—only by the time of exposure to an addition of caustic to the cell. The cell remained leaktight with long-term exposure to hot caustic.

Appendix D

MEASUREMENTS OF SOLUTION VISCOSITIES AND REFRACTIVE INDEX VALUES

Appendix D. MEASUREMENTS OF SOLUTION VISCOSITIES AND REFRACTIVE INDEX VALUES

Viscosity Measurements in SRS Simulant Solutions

Purpose: A value for solution viscosity must be known to determine particle size by the DLS technique. A series of SRS simulant solutions were prepared to cover the variation in concentrations of simulants to be studied by light scattering. Because precipitates will settle to the bottom of the rheometer cell, the viscosities were determined without prior filtration. Samples were degassed by placing the bottles in an ultrasonic water bath for 20 min. Viscosities were then determined at 40, 80, and 100°C.

Procedure: Twenty milliliters of the following solutions were prepared and placed in polypropylene bottles:

100% SRS Simulant Solution A (prepared 2/07/01)
100% SRS Simulant Solution 2A (prepared 2/02/01)
100% SRS Simulant Solution B (SFSC1 preparation)
50/50 SRS Simulant Solution A/2A
50/50 SRS Simulant Solution 2A/B
30/70 SRS Simulant Solution 2A/B

100% SRS Simulant Solution D (prepared 2/20/01)
100% SRS Simulant Solution 2D (prepared 2/21/01)
100% SRS Simulant Solution E (prepared 2/16/01)
50/50 SRS Simulant Solution D/2D
50/50 SRS Simulant Solution 2D/E
30/70 SRS Simulant Solution 2D/E

Equipment: Viscosity determinations were performed using a Brookfield DV-III rheometer, a Brookfield UL adapter, a Haake A81 circulator, a jacketed beaker, and an RTD temperature probe. The adapter, circulator, and beaker were connected with flexible tubing. The temperature probe and water were placed into the beaker. For each test condition, 16 mL of sample was transferred into the adapter, which was then attached to the rheometer. The circulator was set to the desired temperature for the viscosity measurement. The temperatures in the beaker and in the adapter were assumed to be equivalent. After a given sample had reached the desired temperature, it was allowed to equilibrate for 30 min and its viscosity was measured at 40, 50, 60, and 70 rpm. The corresponding shear rates were 49, 61, 73, and 86 s^{-1}. At each rpm increment, measurements were taken every 10 s for a period of 2 min; this procedure was repeated to confirm the consistency of the results. The average viscosity at each rpm was then determined in each case. The individual viscosities were subsequently averaged to determine the final viscosity value for the specific test condition. The maximum experimental error was +/- 0.1 cP. Data were validated by also determining the viscosity of distilled, deionized water and comparing experimental with literature values.

Results: Viscosity and refractive index values of simulant solutions are needed for determination of the particle size (hydrodynamic diameter) based on DLS data. With variation of temperature and concentrations, the refractive index does not change much (~1.38); however, the viscosity changes significantly with temperature as well as solution composition.

I. Viscosities of Various Simulant Solutions (from R. D. Hunt)

Viscosity measurements (in cP) for the SRS evaporator simulants

SRS Simulant	40°C	80°C	95°C
A	2.21	1.16	0.97
A	2.22	1.14	0.94
2A	2.38	1.21	1.04
2A	2.39	1.21	1.05
A + 2A (1/1)	2.28	1.22	1.04
A + 2A (1/1)	2.29	1.22	1.04
B	2.77	1.30	1.02
B	2.79	1.30	1.00
2A + B (1/1)	2.56	1.14	0.94
2A + B (1/1)	2.61	1.09	0.96
2A + B (3/7)	2.66	1.20	1.02
2A + B (3/7)	2.66	1.25	1.04
D	1.92	1.00	0.96
D	1.92	1.02	0.95
2D	1.91	1.03	0.91
2D	1.90	1.05	0.91
D + 2D (1/1)	1.91	0.96	0.90
D + 2D (1/1)	1.93	0.93	0.90
E	2.40	1.16	1.02
E	2.41	1.19	1.00
2D + E (1/1)	2.20	1.06	0.99
2D + E (1/1)	2.18	1.09	1.01
2D + E (3/7)	2.36	1.14	1.03
2D + E (3/7)	2.36	1.14	1.04

An interpolation technique (see the two graphs below for linear regression) was used to calculate the viscosity for conditions without measurements.

Solution Viscosity vs. Temperature for (2A + B)

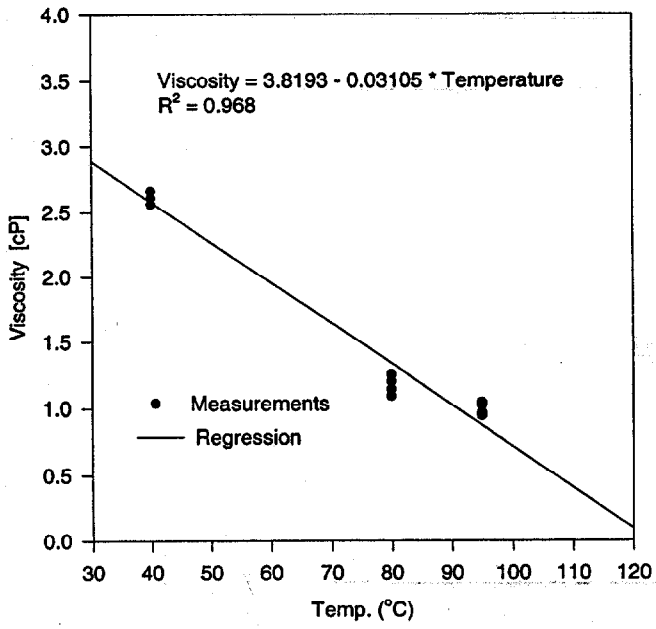

Solution Viscosity vs. Temperature for (2D + E)

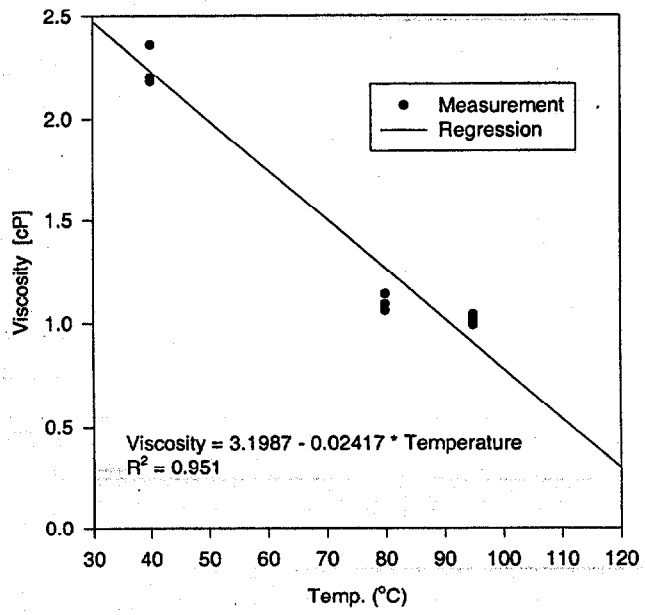

II. Measurement of Refractive Index in SRS Simulants and Sample Mixes

Purpose: The refractive index (RI) values of SRS solutions must be known to accurately determine particle size by the DLS technique.

Equipment: An Abbe 60 Refractometer (Bellingham + Stanley Inc, Norcross, GA) fitted with a Haake thermostated recirculating bath was used to determine the RI values for standards and samples at set temperatures.

Procedure: The refractometer is zeroed by setting the scale for the RI of water at 30°C (set point, ~3.32). Published data[a] are used to calculate the actual RI value for water at any other temperature according to the equation

$$RI_{H_2O} = 1.3379 - 0.00019 \times \text{temperature, °C.}$$

The calculated RI value for water is then used to set the scale reading (intercept) of the refractometer for a specific temperature. The response factor (slope) for the instrument scale is determined by using four prepared sucrose standards (Fisher Scientific Co.; Lot 790452). Again, published data[a] are used to determine the RI values at 20°C for a given concentration of sucrose:

$$RI_{\text{sucrose}} @20°C = 1.3229 + 0.00200 \times [\text{sucrose}], \text{ w/w\%.}$$

The RI value is then calculated[b] for a given temperature as

$$RI_{\text{sucrose}} @ \text{ temperature, °C} = RI_{\text{sucrose}} @20°C + 7.80E\text{-}06 \times (\text{temperature, °C} - 20).$$

Regression analysis of sucrose standards yields a linear equation to convert instrument readings to the refractive index of the particular sample. Neat organic compounds are used to verify the measurement of RI, based on instrument calibration with sucrose standards.

Samples: The RI values for SRS Simulant Solutions A, 2A, B, D, 2D, and E were determined at various temperatures. SRS Simulant A Blend mixed with B solution and D Blend mixed with E Solution were used to make 3 mL of SRS samples according to the "H2 Simulant A Blend" and "H2 Simulant B Blend" spreadsheets. Sample solutions were brought to temperature by submersing them in the reservoir of the recirculating bath.

Results:

1. Instrument Calibration—Data were collected by sequentially increasing the operating temperature. The set point of the scale for the next operating temperature was determined by using the regression equation of the previous temperature to calculate the instrument reading for RI of water for the upper temperature. Sucrose standards were then run at the upper temperature to determine the new regression line for the upper temperature. Table D.1 demonstrates the repeatability of the regression line.

   The RI values for neat organic compounds were measured at 29 °C to verify the performance of prepared sucrose standards. The close correspondence between established values for these organics and sucrose standards (Fig. D.1) indicates that sucrose solutions will provide a valid calibration of the refractometer.

---

[a] *CRC Handbook of Chemistry and Physics*, 61st ed., pp. E-392–E-394.

[b] Operating instructions for Abbe 60 Refractometer, Bellingham + Stanley Lmd., Polyfract Works, Tunbridge Wells, Kent TN2 3EY, England.

Table D.1. Regression analysis of refractometer scale using sucrose standards

Temperature (°C)	Scale intercept	Scale slope
29	-123.59	95.21
40	-118.45	91.64
58	-118.41	91.29
75	-121.46	93.05
90	-121.65	93.11

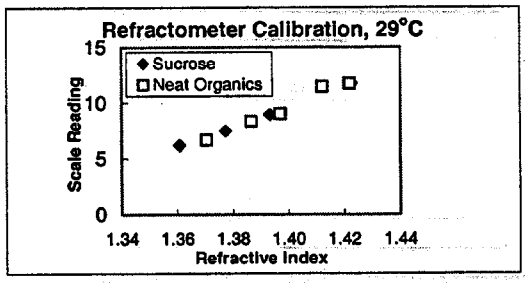

Fig. D.1. Correspondence of sucrose standards and neat organic compounds.

2. Measured Refractive Indexes—A summary of RIs for SRS solutions and samples at temperatures ranging from 29 to 89 °C is given in Table D.2.

Table D.2. RI data summary

		Temperature (°C)				
		29	40	58	75	89
Variable [Si] at constant [Al]	Si = 0.004; Al = 0.133	1.3845	1.3847	1.3864	1.3850	1.3852
	Si = 0.025; Al = 0.133	1.3850	1.3853	1.3870	1.3849	1.3861
	Si = 0.075; Al = 0.133	1.3863	1.3865	1.3883	1.3873	1.3868
	Si = 0.15; Al = 0.133	1.3843	1.3844	1.3863	1.3845	1.3854
Variable [Al] at constant [Si]	Si = 0.05; Al = 0.03	1.3805	1.3805	1.3823	1.3804	1.3809
	Si = 0.05; Al = 0.10	1.3817	1.3817	1.3838	1.3820	1.3820
	Si = 0.05; Al = 0.20	1.3836	1.3838	1.3859	1.3830	1.3840
	Si = 0.05; Al = 0.30	1.3851	1.3851	1.3875	1.3860	1.3858
SRS Simulant Solutions	Solution A 2/07	1.3813	1.3809	1.3827	1.3829	1.3820
	Solution 2A 2/02	1.3858	1.3858	1.3874	1.3850	1.3862
	Solution D	1.3756	1.3751	1.3778	1.3766	1.3769
	Solution 2D	1.3760	1.3759	1.3787	1.3759	1.3764
	Solution B	1.3856	1.3848	1.3869	1.3866	1.3862
	Solution E	1.3837	1.3835	1.3854	1.3841	1.3839
	6 *N* NaOH	1.3838	1.3839	1.3858	1.3841	1.3847
Sucrose standards, (%, w/w)	Sucrose = 18.87%	1.3609	1.3619	1.3631	1.3630	1.3620
	Sucrose = 27.09%	1.3774	1.3763	1.3778	1.3760	1.3776
	Sucrose = 34.98%	1.3932	1.3931	1.3888	1.3926	1.3926
	Sucrose = 49.62%	1.4226	1.4233	1.4252	1.4242	1.4239

3. Data Trends—The RI values of all solutions peaked at 59°C; the RI decreased by approximately 2% from the maximum value when the solution temperature was 90°C. Within a sample type, the RI increased with the concentration of dissolved solids. Although the sample containing 0.075 *M* Si in the Variable Si samples appeared too high compared with the remaining samples in this group, the results are reasonable if total dissolved solids in the samples are considered (Fig. D.2).

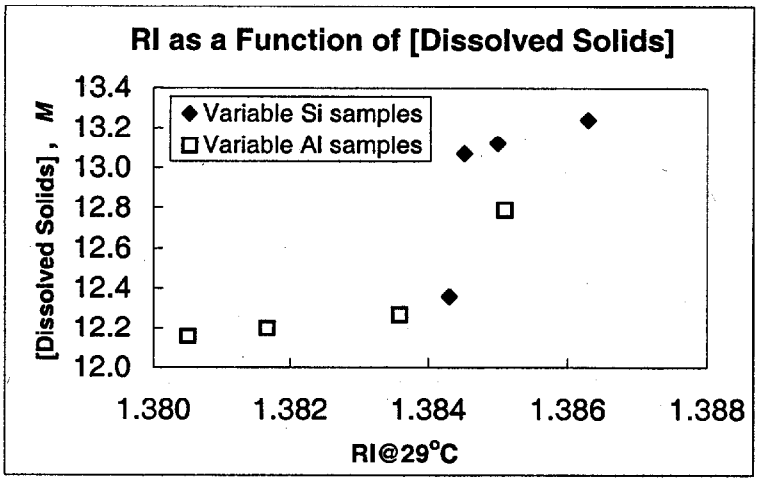

Fig. D.2. Relationship between dissolved solids concentration and sample RI.

Within the Variable Si sample group, samples containing [Si] ≥ 0.075 *M* formed precipitates when heated above 60°C. The RI values of cloudy samples were significantly underestimated compared with their clear filtrates after solids removal with a 0.02-μm-pore syringe filter. The clarified samples had RI values following the trend line of lower-temperature sample data.

Appendix E

INDUCTION PERIOD MEASUREMENTS

Appendix E. INDUCTION PERIOD MEASUREMENTS

Variation of Induction Time with Temperature

0.05 *M* Si, 0.05 *M* Al		0.10 *M* Si, 0.133 *M* Al	
Temperature (°C)	Induction time, (min)	Temperature, (°C)	Induction time, (min)
40	1250	40	500
59	215	49	225
77	68	59	105
105	22.3	68	60
		77	37
		105	5.6

Variation of Induction Time with Aluminum Concentration, [Si] = 0.05 *M*

	Induction time (min)	
[Al] (*M*)	77°C	105°C
0.30	22.2	9
0.25	17.2	9.9
0.20	27.3	11.5
0.15	37.2	6.1
0.10	36.5	10.3
0.05	95.8	22.3
0.04		28.3
0.03	150	13.2

Variation of Induction Time with Silicon Concentration, [Al] = 0.133 *M*

	Induction time (min)	
[Si] (*M*)	77°C	105°C
0.004	–	225
0.010	290	132
0.025	90	25.3
0.050	30	10.2
0.075	20.3	15
0.100	24.3	9.7
0.133	15.2	4.6
0.150	20.3	4.1

Estimation of Induction Time

Induction period is determined from dynamic-light-scattering data using a plot of average particle size vs time. The crossing point between a straight line fitting the initial particle growth curve and the time axis defines the induction time. Additionally, data of the scattering intensity vs time are used to determine induction period. Plots of particle size and intensity vs. time for the dynamic-light-scattering experiments are included in Appendix F.

Induction times for experiments conducted at temperatures of 80°C and lower were determined directly from plots of particle size vs time, as indicated in the plot below.

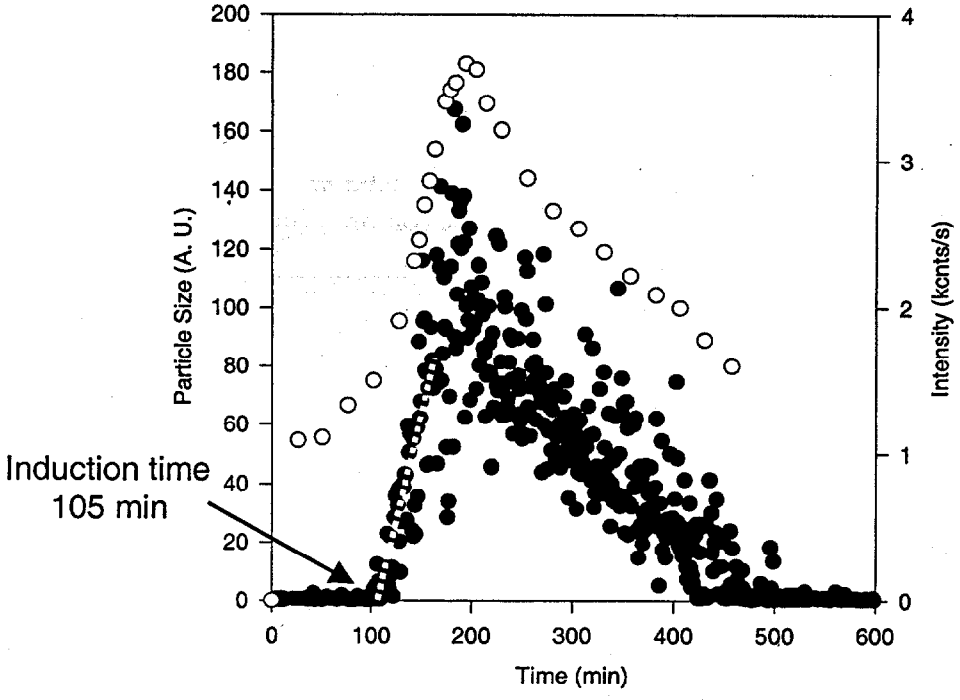

The plots of particle size vs time for the experiments conducted at 105°C in the translucent Teflon test tubes were less ideal. It appears that the Teflon interferes with the size determination. During the initial period of the experiments, the measured size data were noisy and of significant magnitude. After a period of time, the measured size flattened out to a nonzero value, suggesting that induction had already occurred. Consistently, the plots of scattering intensity exhibited sharp increases in the range of time when the size curve was flattening. Therefore, the point of inflection in the scattering intensity was used as the estimate of induction time for these experiments. An example is shown below.

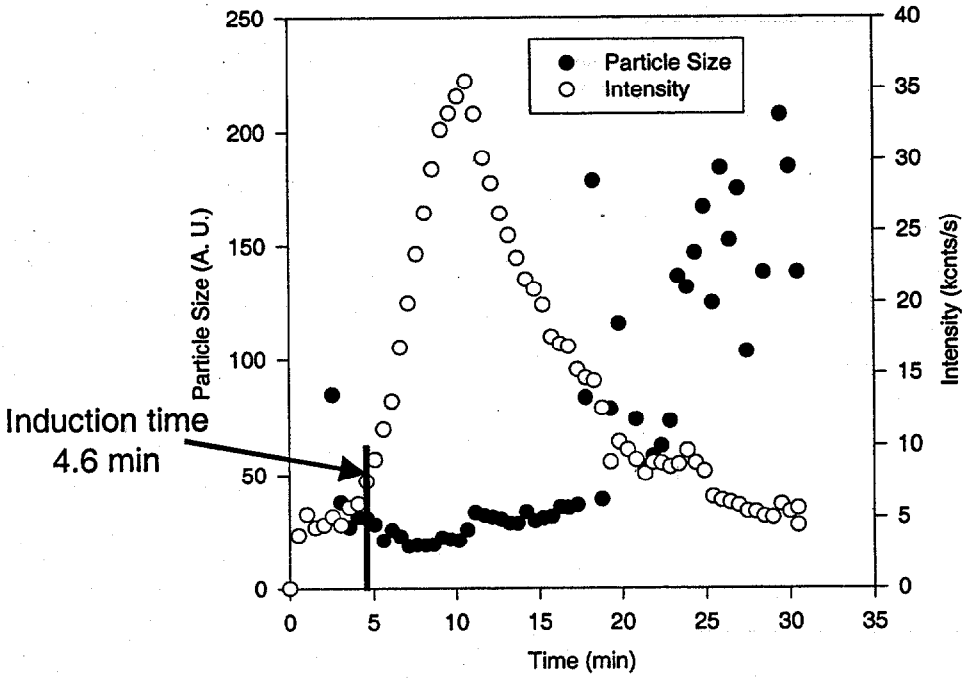

Reproducibility:

The reproducibility of induction time measurements was estimated by triplicate experiments conducted at identical conditions. The results are shown in the table below.

	80°C		105°C	
	Time	Relative error	Time	Relative error
Trial 1	1400 s	- 9.52%	1050 s	6.67%
Trial 2	1220 s	3.83%	1170 s	- 4.27%
Trial 3	1180 s	7.34%	1140 s	- 1.75%
Std. Deviation	117 s (1.95 min)		62.45 s (1.04 min)	
Rel. Std. Dev.	9.23%		5.58%	

Appendix F

DETAILED DATA FOR REAL-TIME DLS EXPERIMENTS

Appendix F. DETAILED DATA FOR REAL-TIME DLS EXPERIMENTS

Particle size (nm or a. u.) and intensity (kcount/s) data vs time (min) are typically plotted for each set of measurement. Note that solution composition (and viscosity) change with time during particle formation, which might affect the exact determination of particle sizes.

I. DLS Data at Various Temperatures (40, 50, 60, 70, 80, and 105°C)

Using solution of 0.1 M Si—0.133 M Al (from Blend A + B)

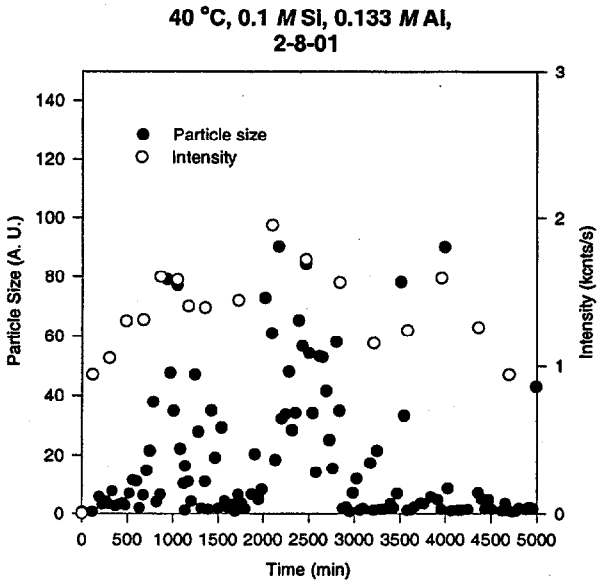

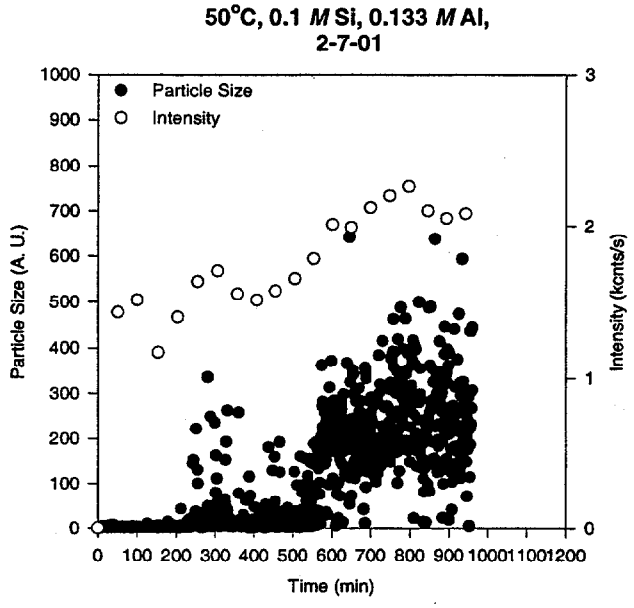

60°C, 0.1 *M* Si, 0.133 *M* Al,
2-5-01

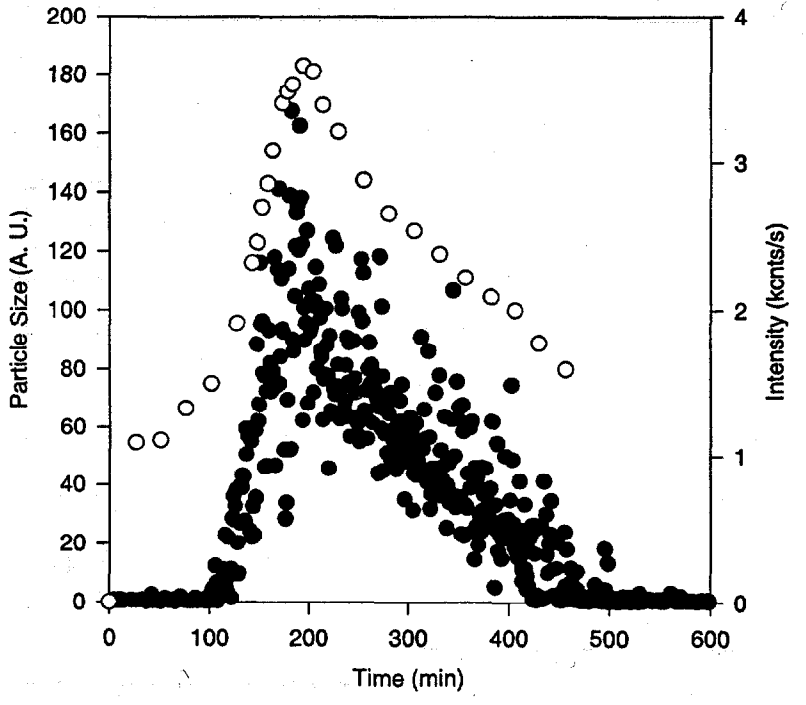

70°C,0.1 *M* Si, 0.133 *M* Al
2-6-01

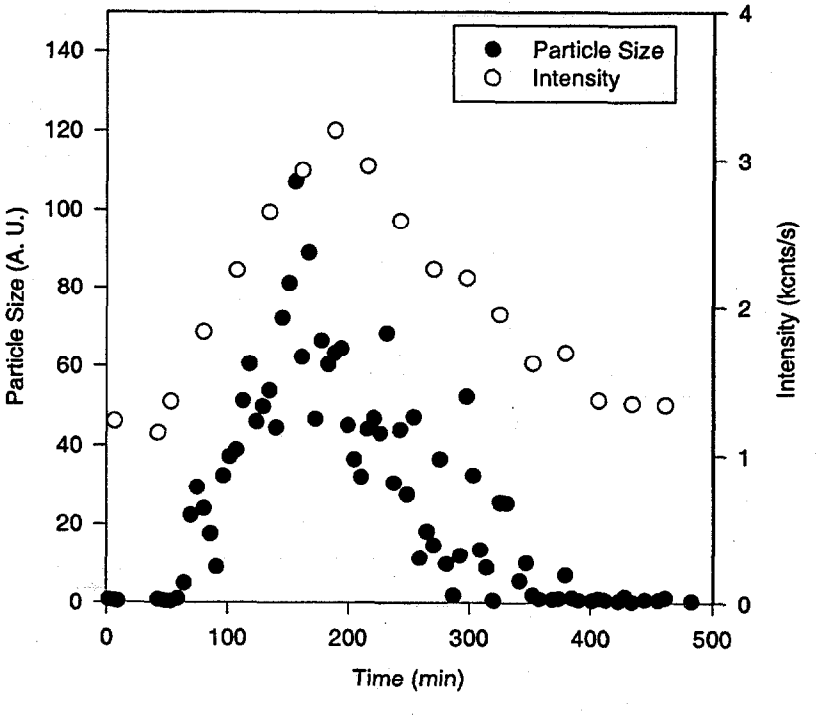

80°C, 0.1 *M* Si, 0.133 *M* Al
2-6-01a

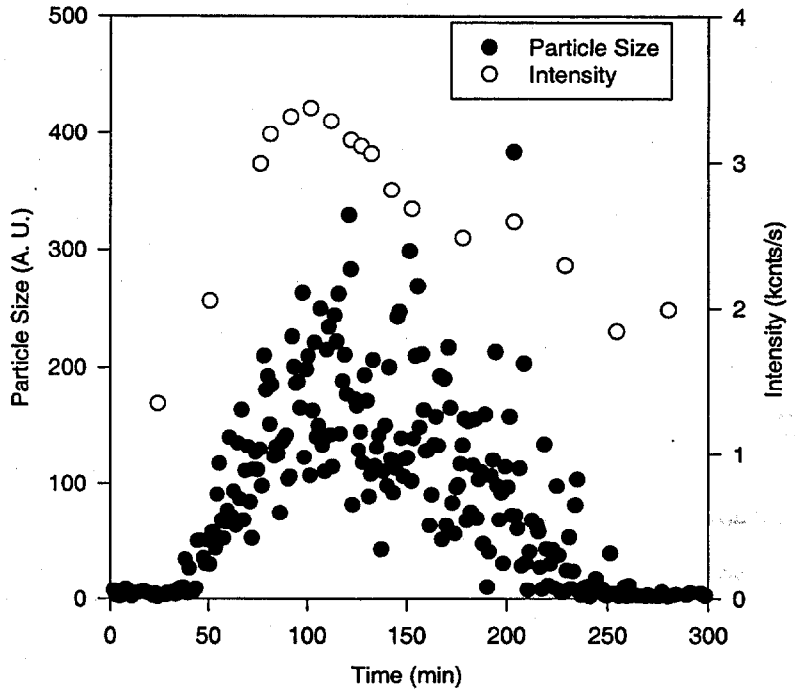

105°C, 0.1 *M* Si, 0.133 *M* Al
3-13-01

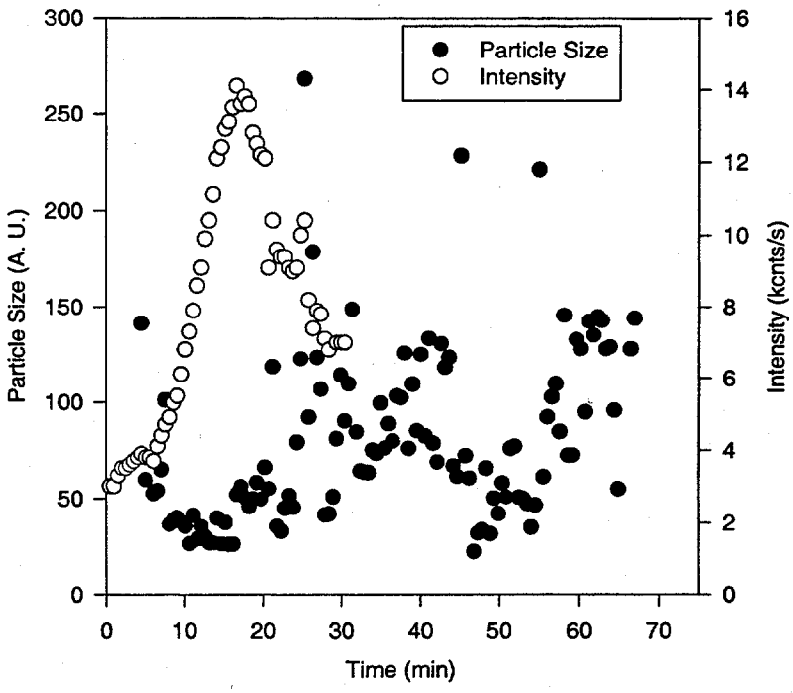

II. **DLS Data at Various Temperatures (40, 60, 80, and 105°C)**
Using solution of 0.05 *M* Si and 0.05 *M* Al (from Blend D + E)

80°C 0.05 *M* Si, 0.05 *M* Al
2-22-01b

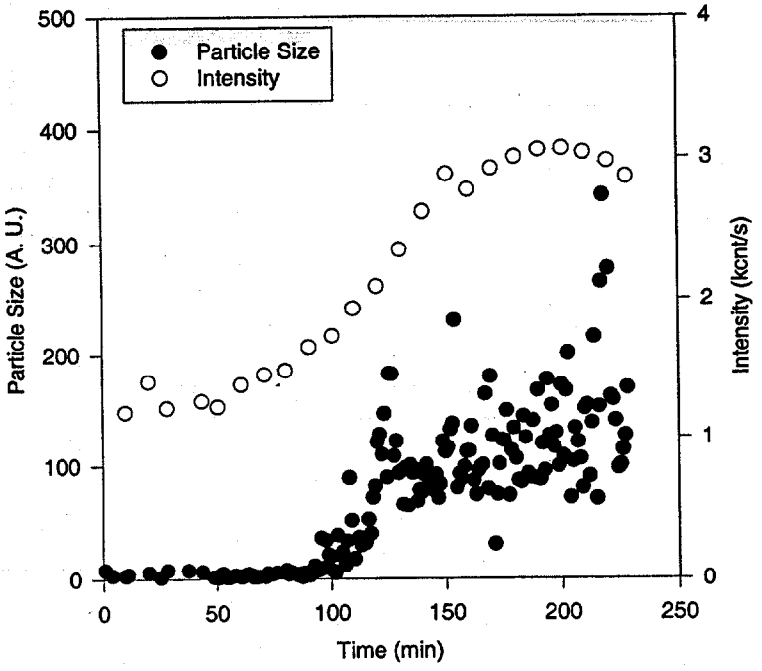

60°C, 0.05 *M* Si, 0.05 *M* Al
3-11-01

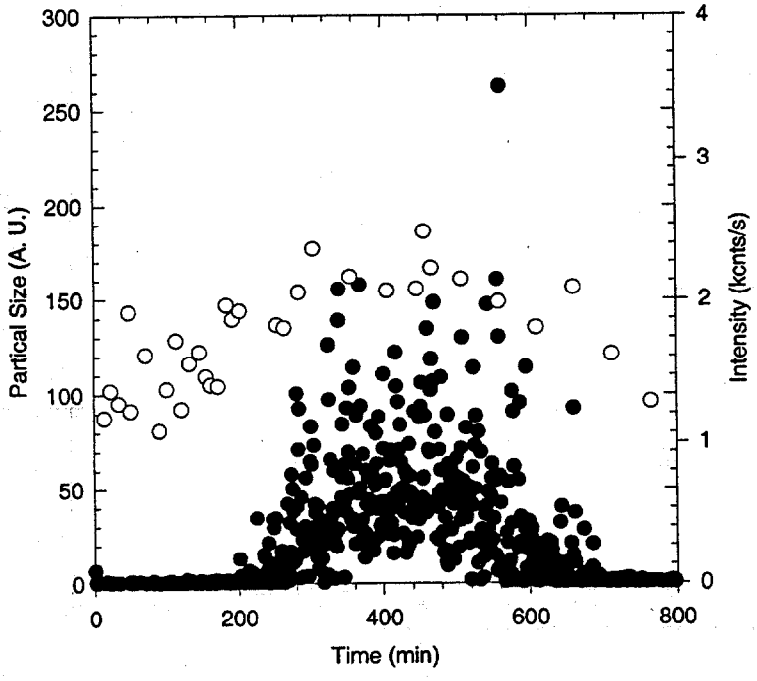

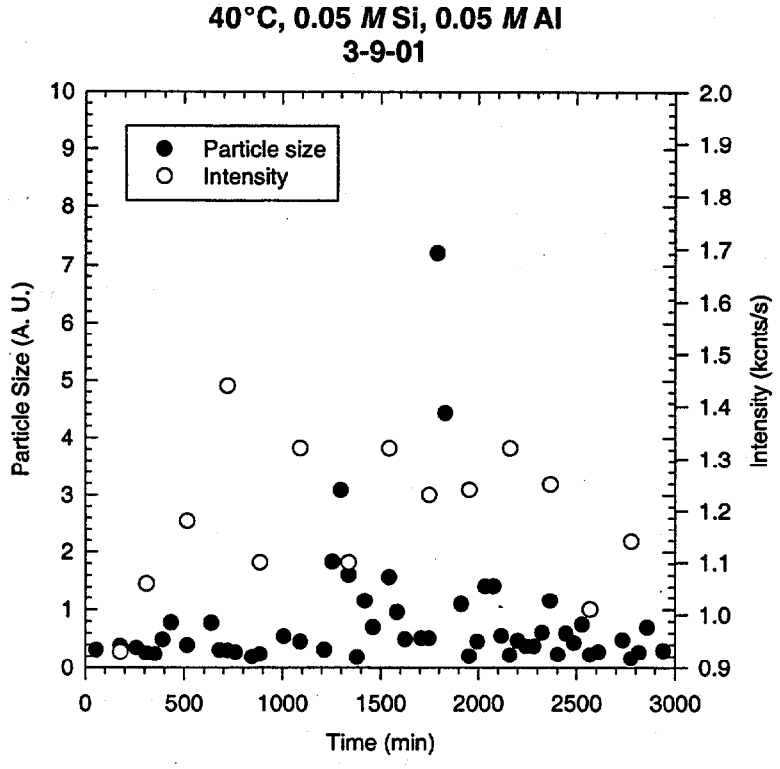
40°C, 0.05 M Si, 0.05 M Al
3-9-01
Particle size
Intensity
Particle Size (A. U.)
Intensity (kcnts/s)
Time (min)
0
500
1000
1500
2000
2500
3000
0
1
2
3
4
5
6
7
8
9
10
0.9
1.0
1.1
1.2
1.3
1.4
1.5
1.6
1.7
1.8
1.9
2.0

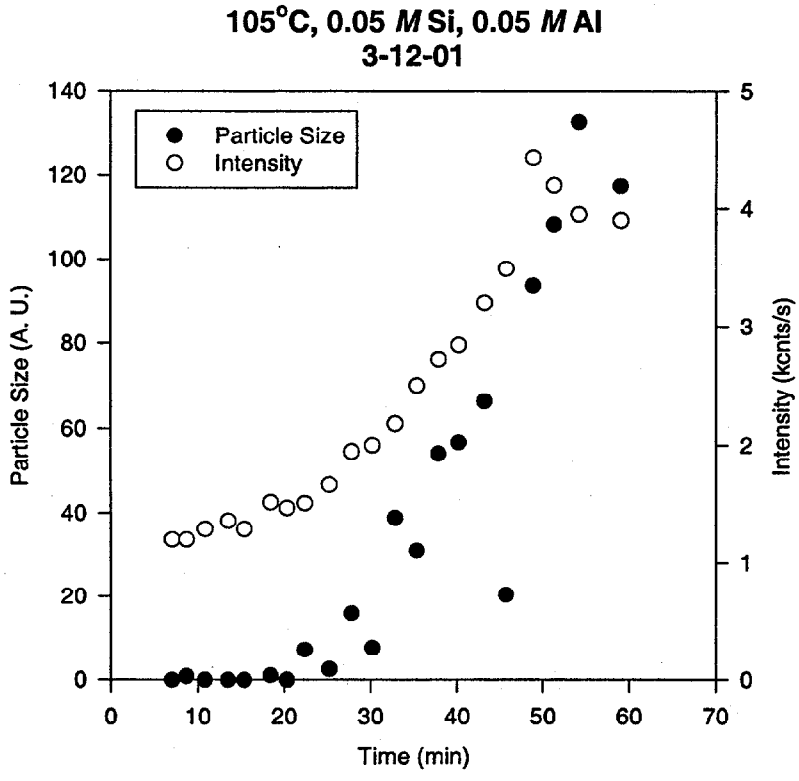
105°C, 0.05 M Si, 0.05 M Al
3-12-01
Particle Size
Intensity
Particle Size (A. U.)
Intensity (kcnts/s)
Time (min)
0
10
20
30
40
50
60
70
0
20
40
60
80
100
120
140
0
1
2
3
4
5

III. DLS Data at Various [Si]: 0.15, 0.133, 0.1, 0.075, 0.05, 0.01, and 0.004 *M*
At fixed 0.133 *M* Al and 80°C (using solution of blend A + B)

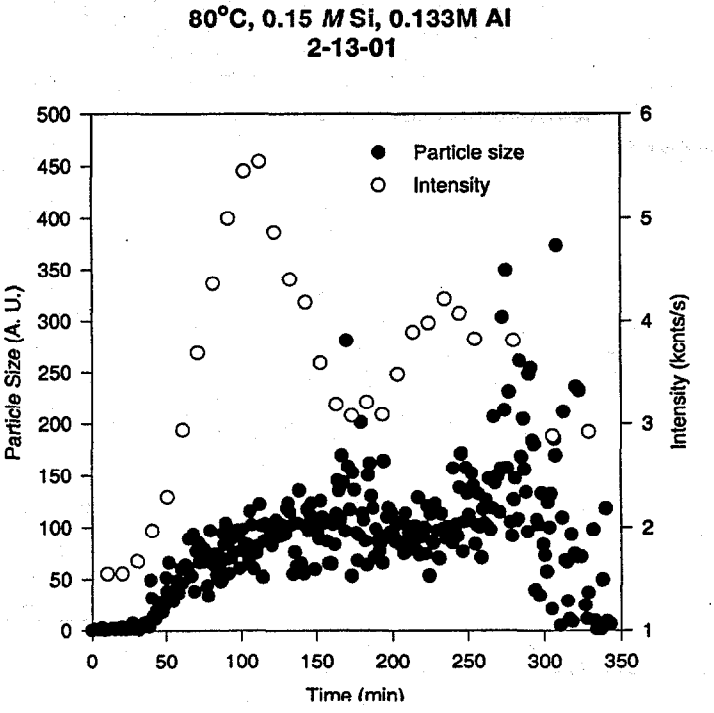

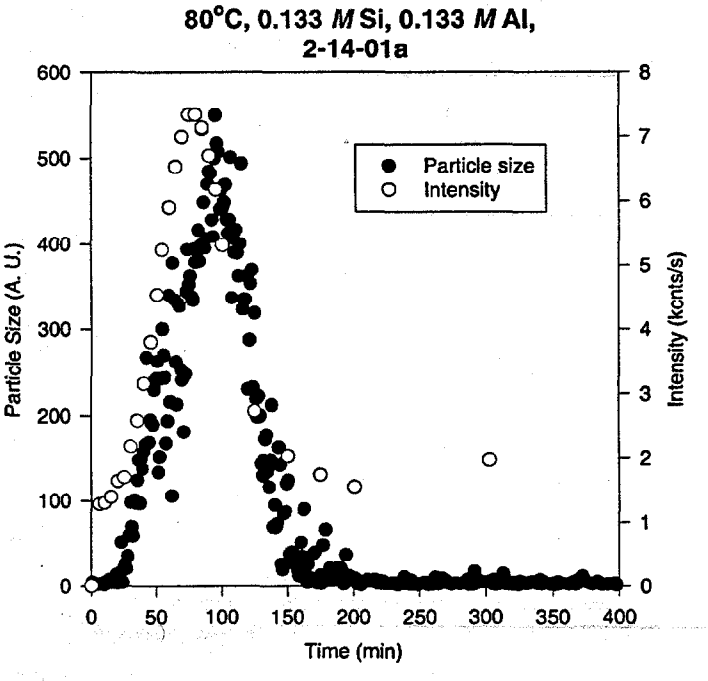

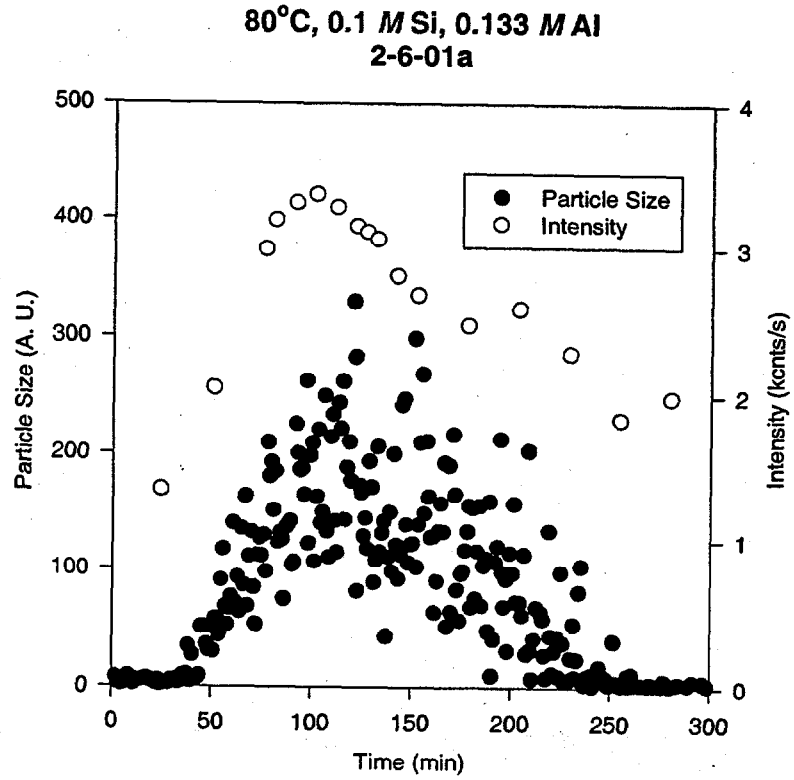
80°C, 0.1 M Si, 0.133 M Al
2-6-01a
Particle Size
Intensity
Particle Size (A. U.)
Intensity (kcnts/s)
Time (min)
0
50
100
150
200
250
300
100
200
300
400
500
1
2
3
4

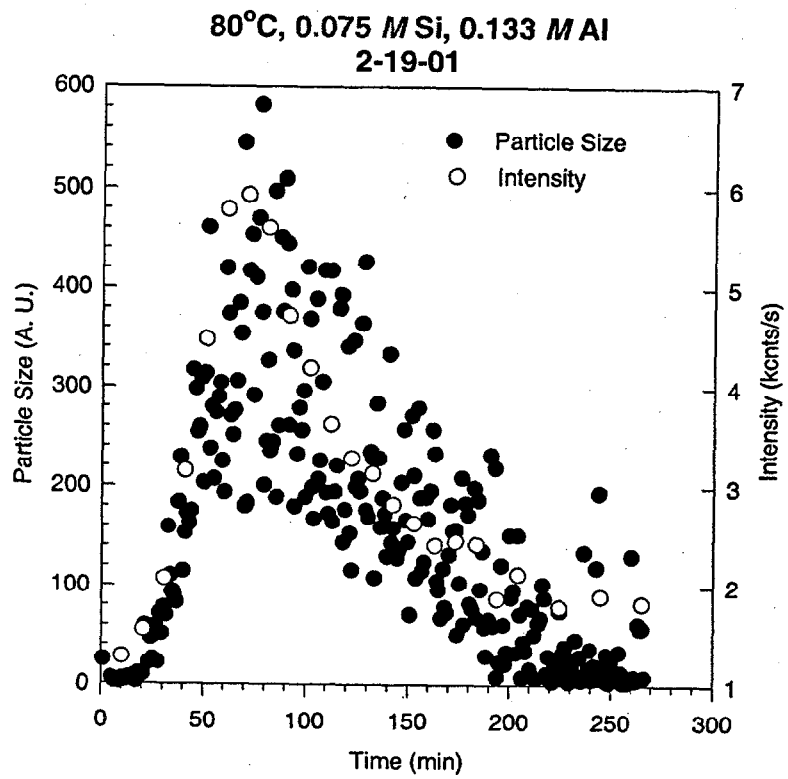
80°C, 0.075 M Si, 0.133 M Al
2-19-01
Particle Size
Intensity
Particle Size (A. U.)
Intensity (kcnts/s)
Time (min)
0
50
100
150
200
250
300
100
200
300
400
500
600
1
2
3
4
5
6
7

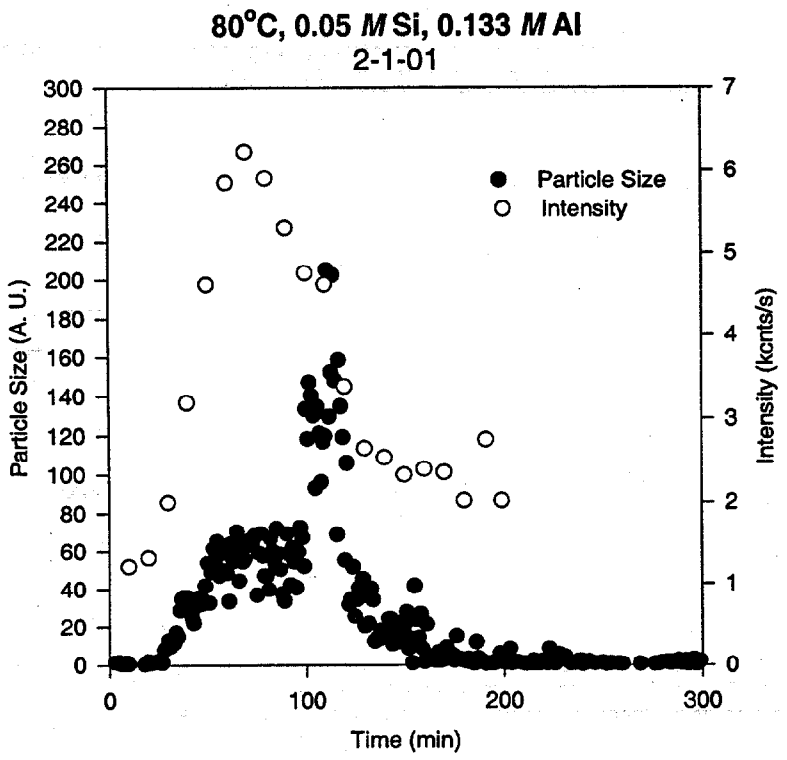
80°C, 0.05 M Si, 0.133 M Al
2-1-01
Particle Size
Intensity
Particle Size (A. U.)
Intensity (kcnts/s)
Time (min)
0
20
40
60
80
100
120
140
160
180
200
220
240
260
280
300
0
1
2
3
4
5
6
7
0
100
200
300

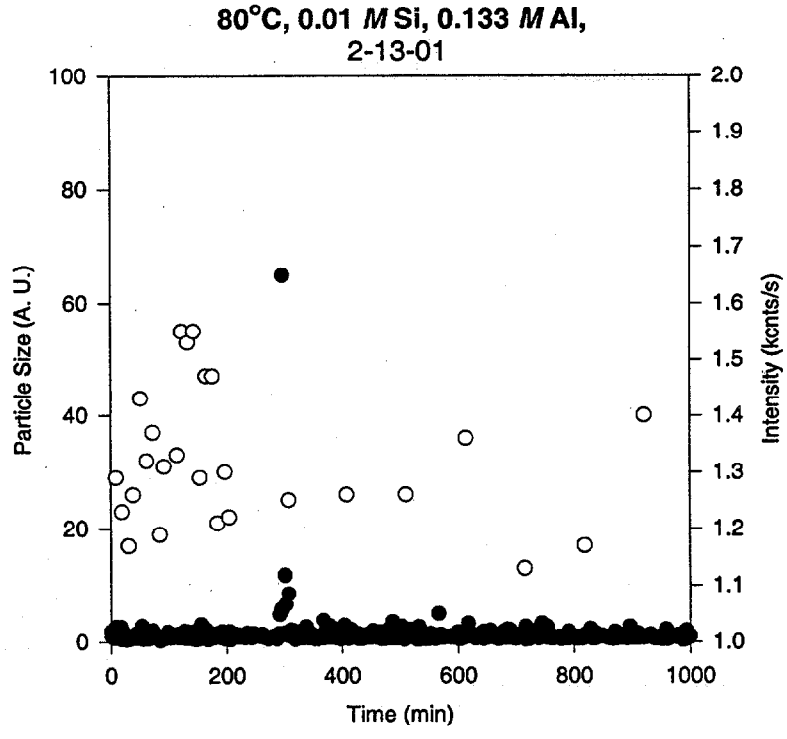
80°C, 0.01 M Si, 0.133 M Al,
2-13-01
Particle Size (A. U.)
Intensity (kcnts/s)
Time (min)
0
20
40
60
80
100
1.0
1.1
1.2
1.3
1.4
1.5
1.6
1.7
1.8
1.9
2.0
0
200
400
600
800
1000

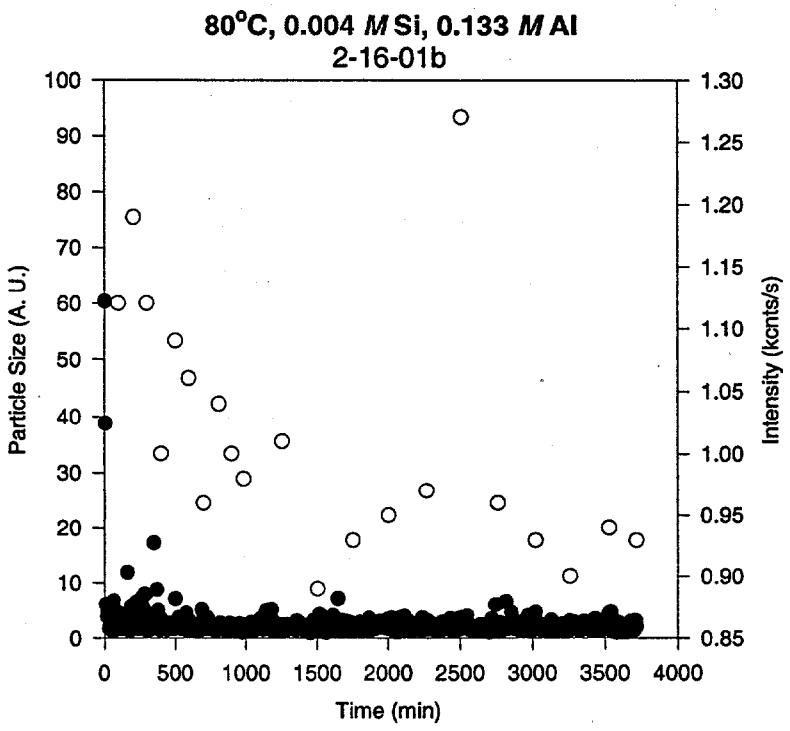
80°C, 0.004 M Si, 0.133 M Al
2-16-01b
Particle Size (A. U.)
Intensity (kcnts/s)
Time (min)
0
10
20
30
40
50
60
70
80
90
100
0.85
0.90
0.95
1.00
1.05
1.10
1.15
1.20
1.25
1.30
0
500
1000
1500
2000
2500
3000
3500
4000

IV. DLS Data at Various [Al]: 0.3, 0.25, 0.2, 0.1, and 0.03 *M*

At fixed 0.05 *M* Si and 80°C (using solution Blend D + E)

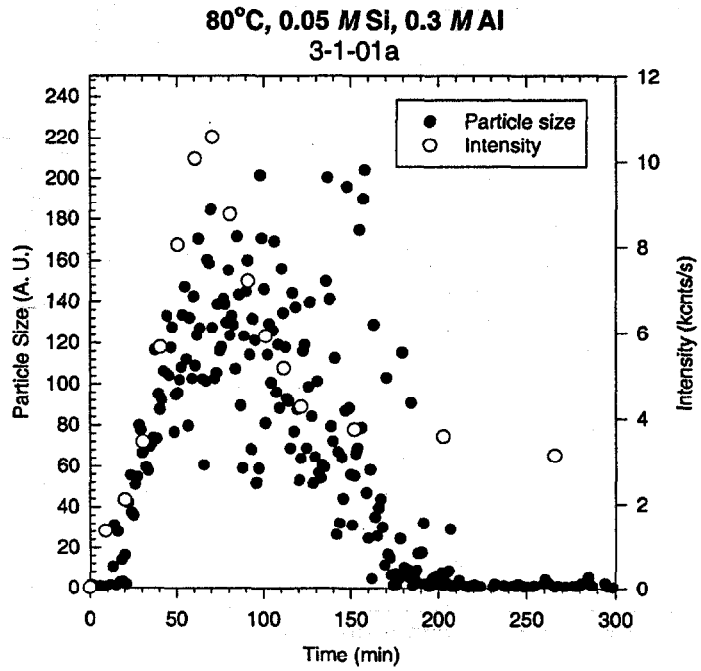

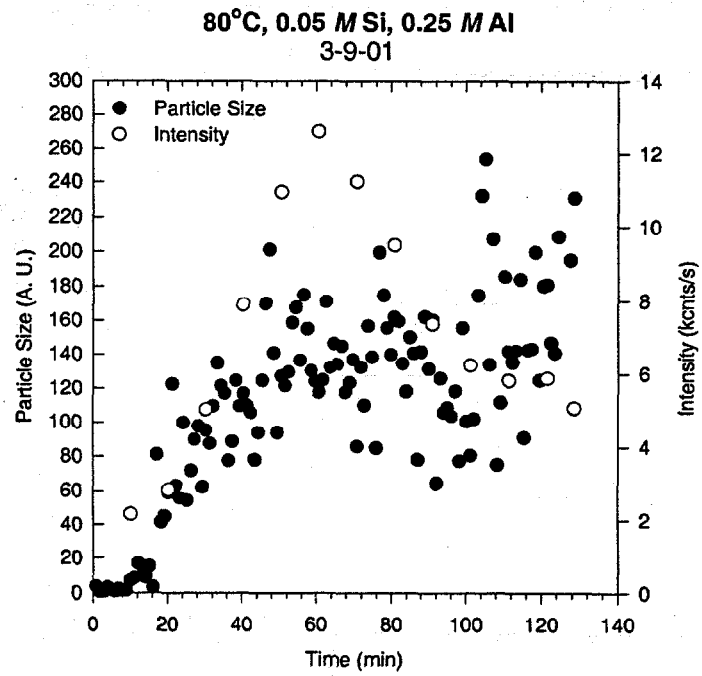

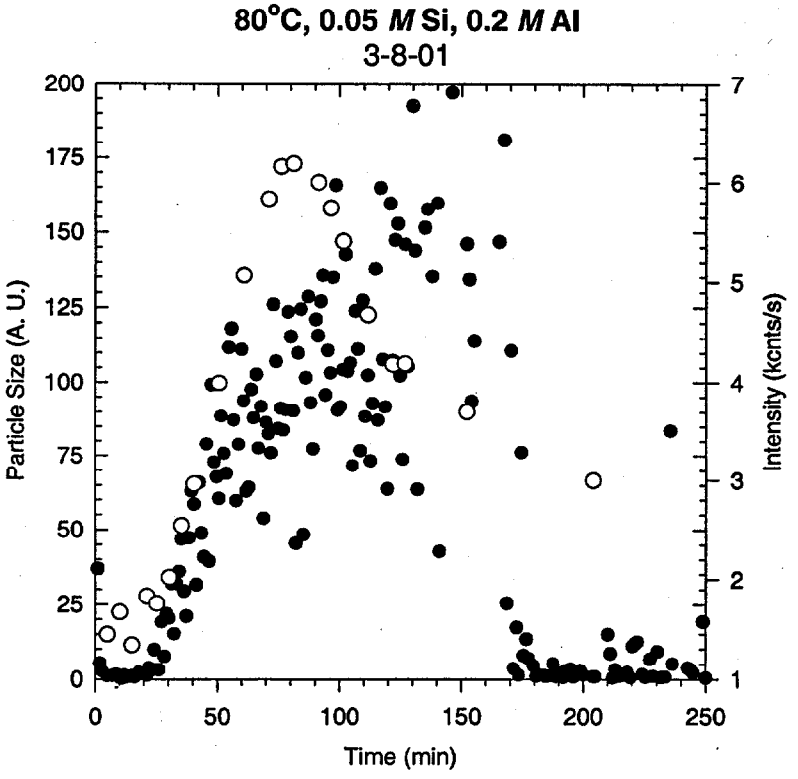
80°C, 0.05 M Si, 0.2 M Al
3-8-01
Particle Size (A. U.)
Intensity (kcnts/s)
Time (min)
0
25
50
75
100
125
150
175
200
1
2
3
4
5
6
7
0
50
100
150
200
250

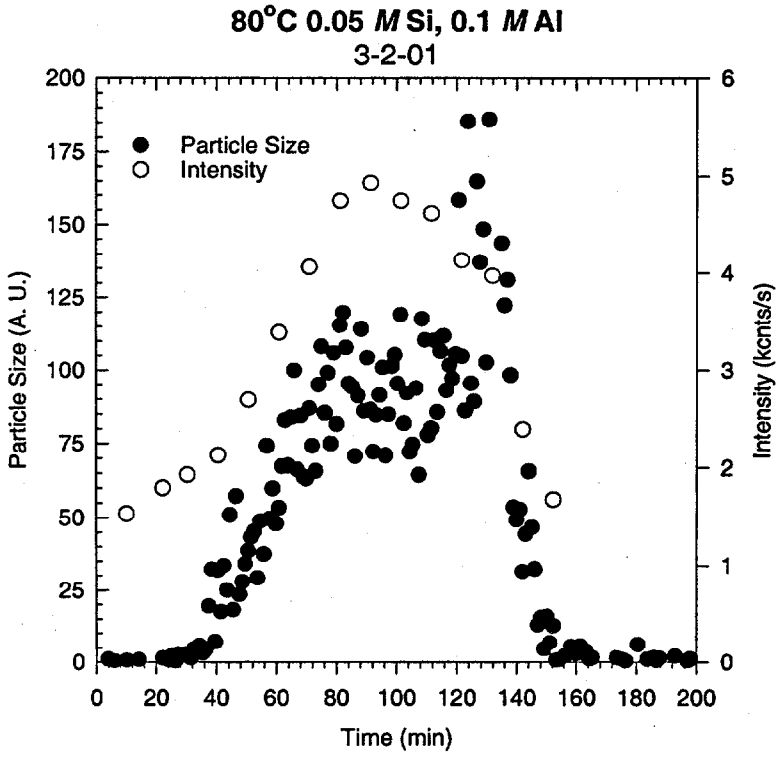
80°C 0.05 M Si, 0.1 M Al
3-2-01
Particle Size
Intensity
Particle Size (A. U.)
Intensity (kcnts/s)
Time (min)
0
25
50
75
100
125
150
175
200
0
1
2
3
4
5
6
0
20
40
60
80
100
120
140
160
180
200

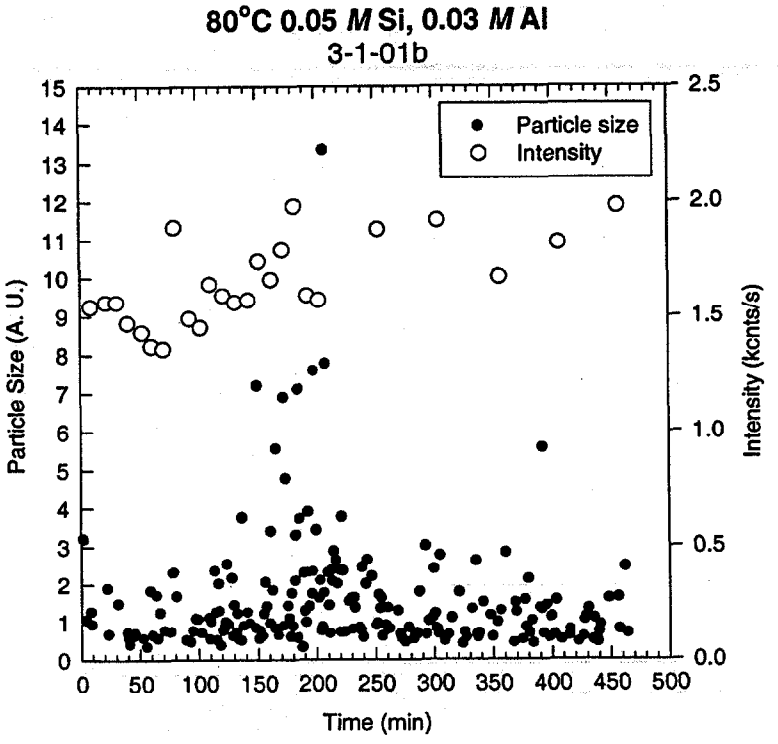
80°C 0.05 M Si, 0.03 M Al
3-1-01b
Particle size
Intensity
Particle Size (A. U.)
Intensity (kcnts/s)
Time (min)
0
1
2
3
4
5
6
7
8
9
10
11
12
13
14
15
0.0
0.5
1.0
1.5
2.0
2.5
0
50
100
150
200
250
300
350
400
450
500

V. DLS Data on Variation of [Si] at 105°C (with Fixed [Al] = 0.133 *M*)

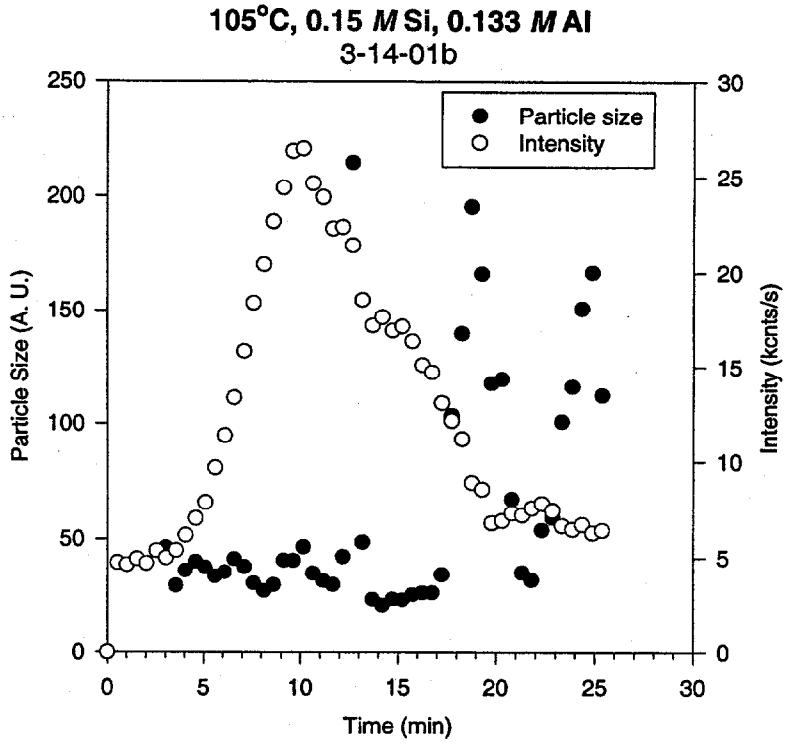

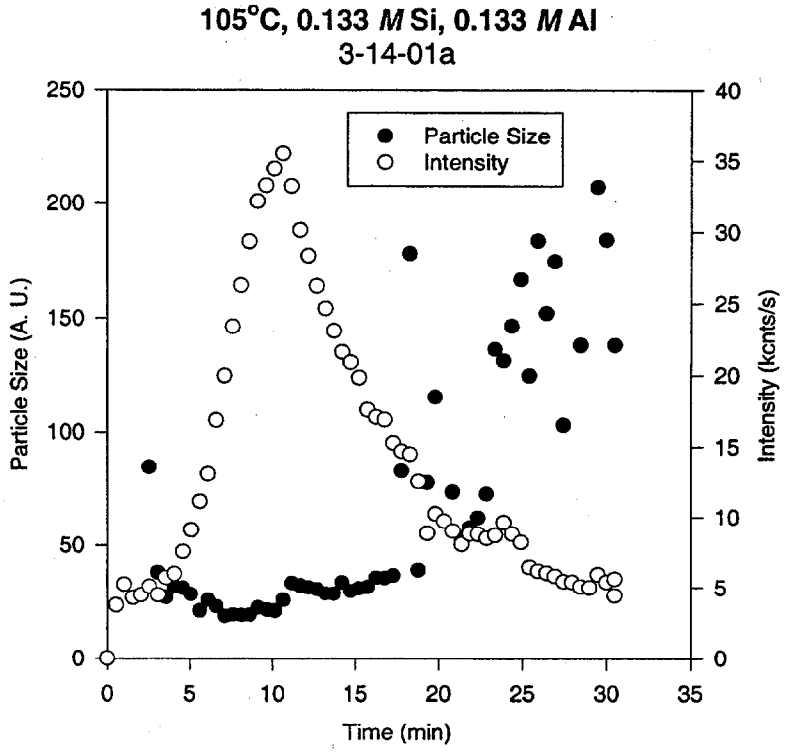

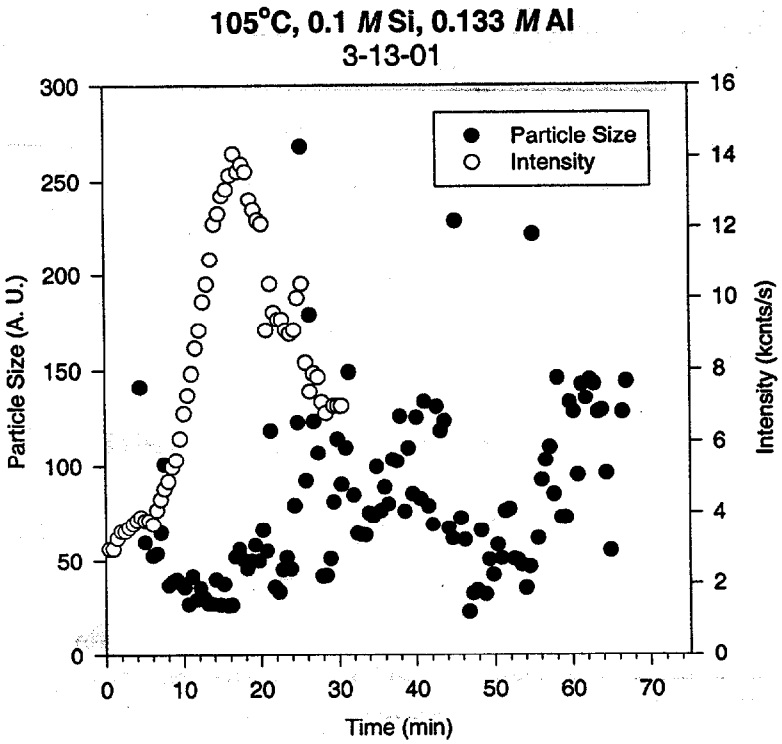
105°C, 0.1 M Si, 0.133 M Al
3-13-01
Particle Size
Intensity
Particle Size (A. U.)
Intensity (kcnts/s)
Time (min)
0
50
100
150
200
250
300
0
2
4
6
8
10
12
14
16
0
10
20
30
40
50
60
70

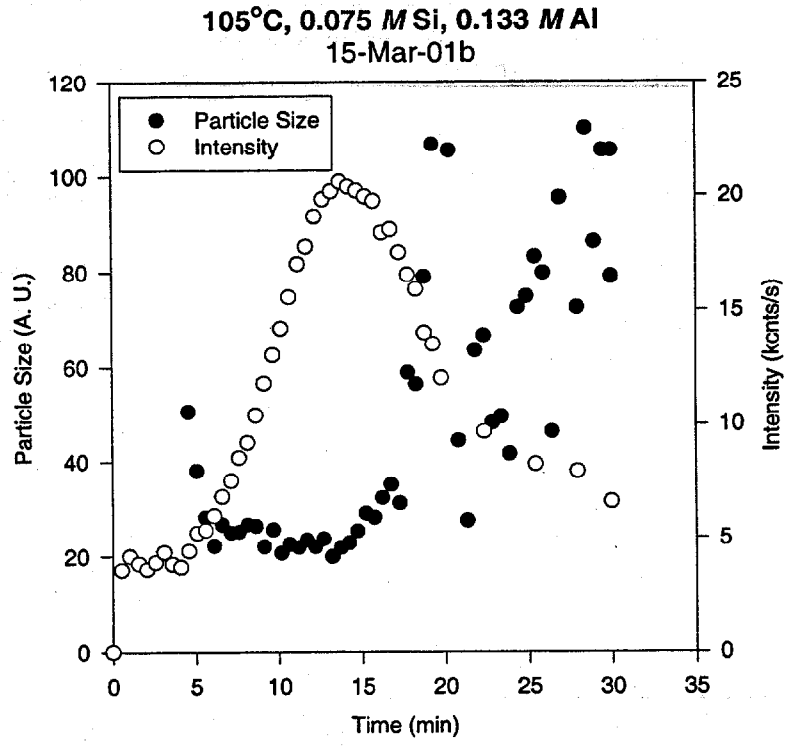
105°C, 0.075 M Si, 0.133 M Al
15-Mar-01b
Particle Size
Intensity
Particle Size (A. U.)
Intensity (kcnts/s)
Time (min)
0
20
40
60
80
100
120
0
5
10
15
20
25
0
5
10
15
20
25
30
35

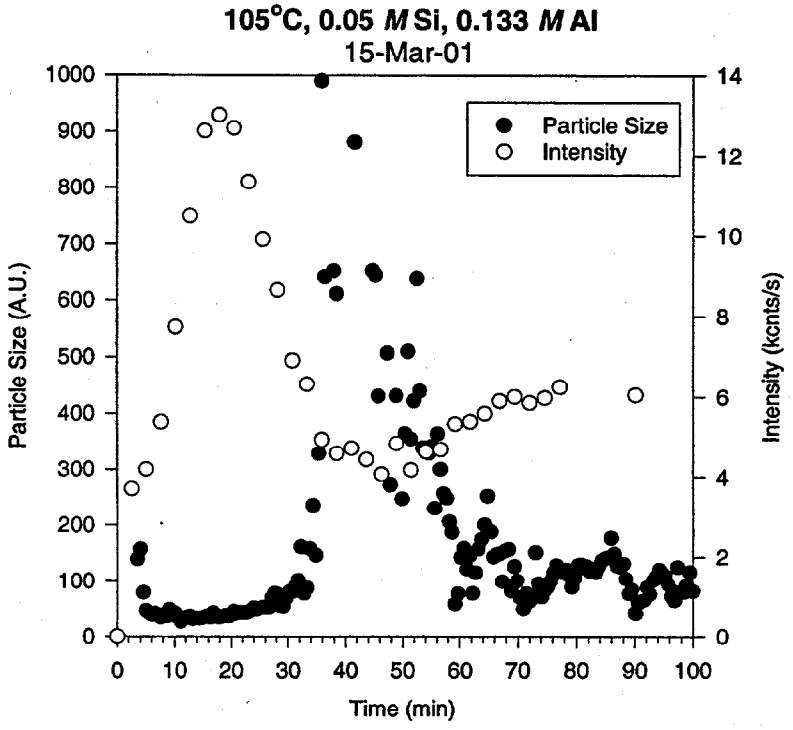
105°C, 0.05 M Si, 0.133 M Al
15-Mar-01
Particle Size
Intensity
Particle Size (A.U.)
Intensity (kcnts/s)
Time (min)
0
100
200
300
400
500
600
700
800
900
1000
0
2
4
6
8
10
12
14
0
10
20
30
40
50
60
70
80
90
100

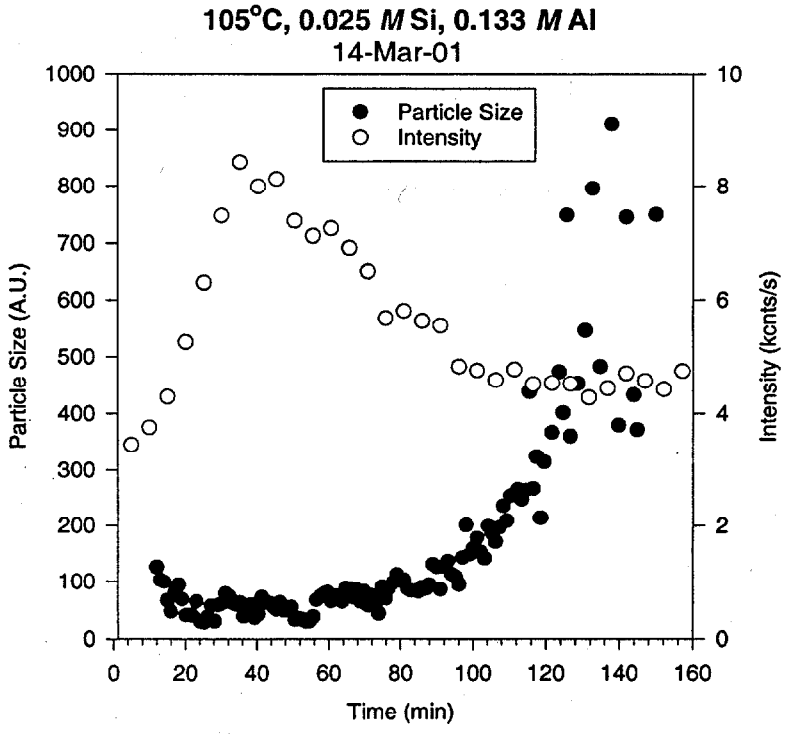
105°C, 0.025 M Si, 0.133 M Al
14-Mar-01
Particle Size
Intensity
Particle Size (A.U.)
Intensity (kcnts/s)
Time (min)
0
100
200
300
400
500
600
700
800
900
1000
0
2
4
6
8
10
0
20
40
60
80
100
120
140
160

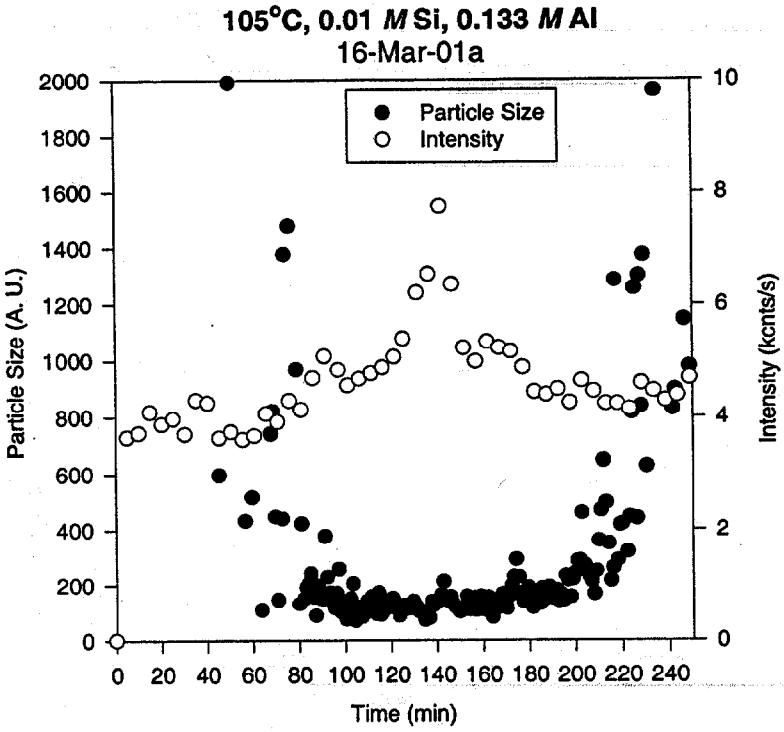
105°C, 0.01 M Si, 0.133 M Al
16-Mar-01a
Particle Size
Intensity
Particle Size (A. U.)
Intensity (kcnts/s)
Time (min)
0
200
400
600
800
1000
1200
1400
1600
1800
2000
0
2
4
6
8
10
0 20 40 60 80 100 120 140 160 180 200 220 240

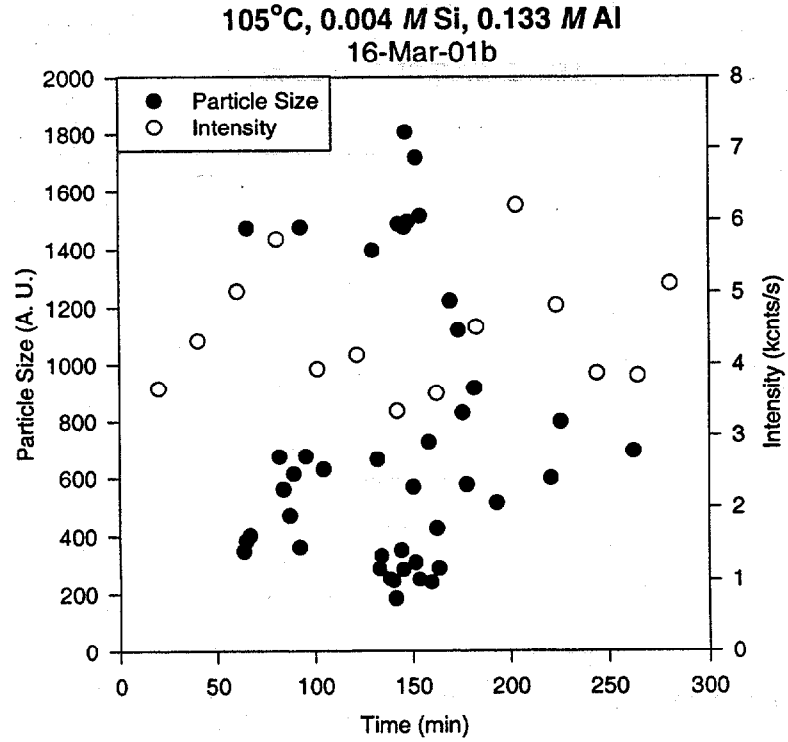
105°C, 0.004 M Si, 0.133 M Al
16-Mar-01b
Particle Size
Intensity
Particle Size (A. U.)
Intensity (kcnts/s)
Time (min)
0
200
400
600
800
1000
1200
1400
1600
1800
2000
0
1
2
3
4
5
6
7
8
0 50 100 150 200 250 300

VI. DLS Data on Variation of [Al] at 105°C with Fixed [Si] = 0.05 *M*

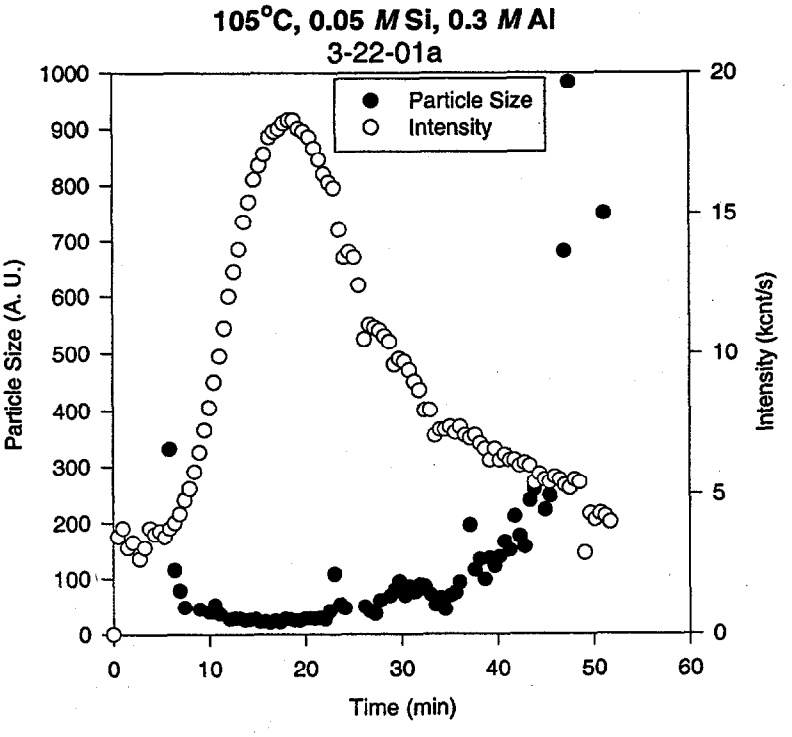

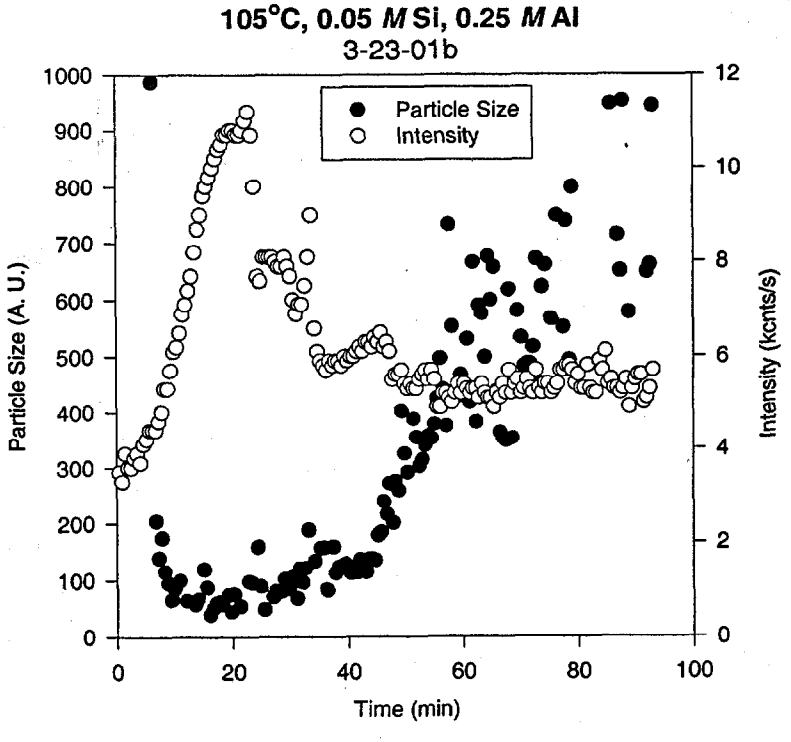

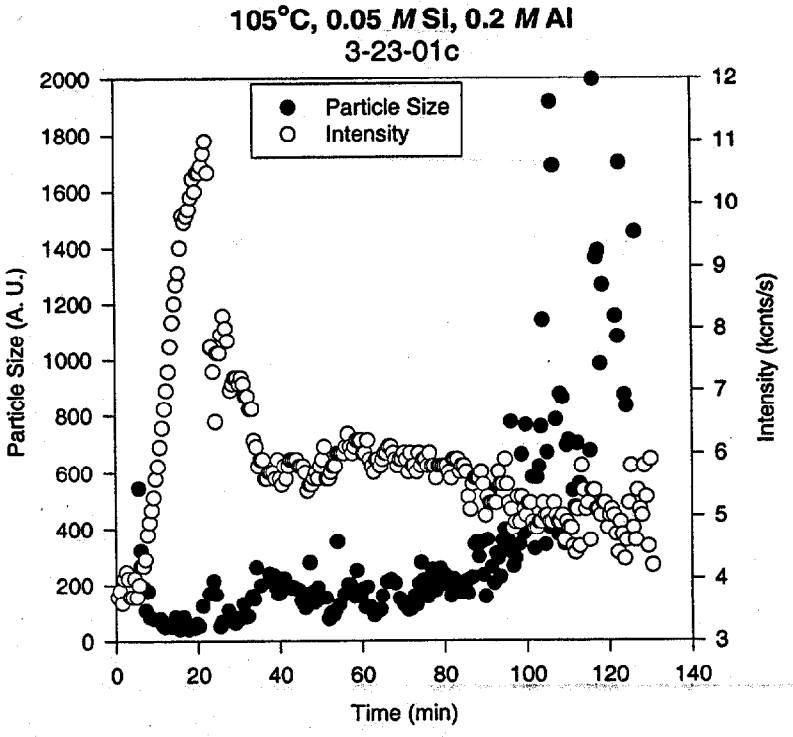
105°C, 0.05 M Si, 0.2 M Al
3-23-01c
Particle Size
Intensity
Particle Size (A. U.)
Intensity (kcnts/s)
Time (min)
0
200
400
600
800
1000
1200
1400
1600
1800
2000
3
4
5
6
7
8
9
10
11
12
0
20
40
60
80
100
120
140

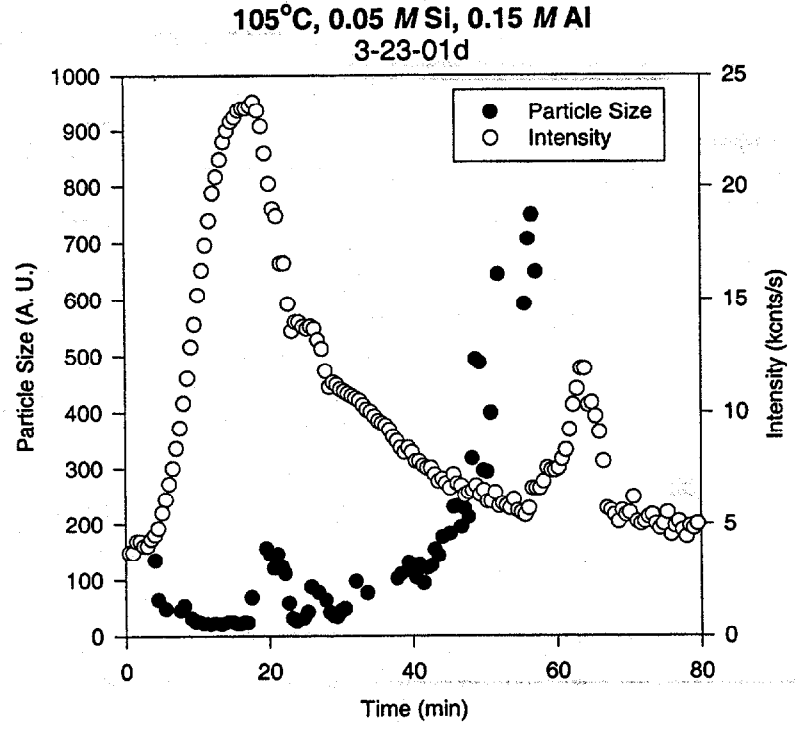
105°C, 0.05 M Si, 0.15 M Al
3-23-01d
Particle Size
Intensity
Particle Size (A. U.)
Intensity (kcnts/s)
Time (min)
0
100
200
300
400
500
600
700
800
900
1000
0
5
10
15
20
25
0
20
40
60
80

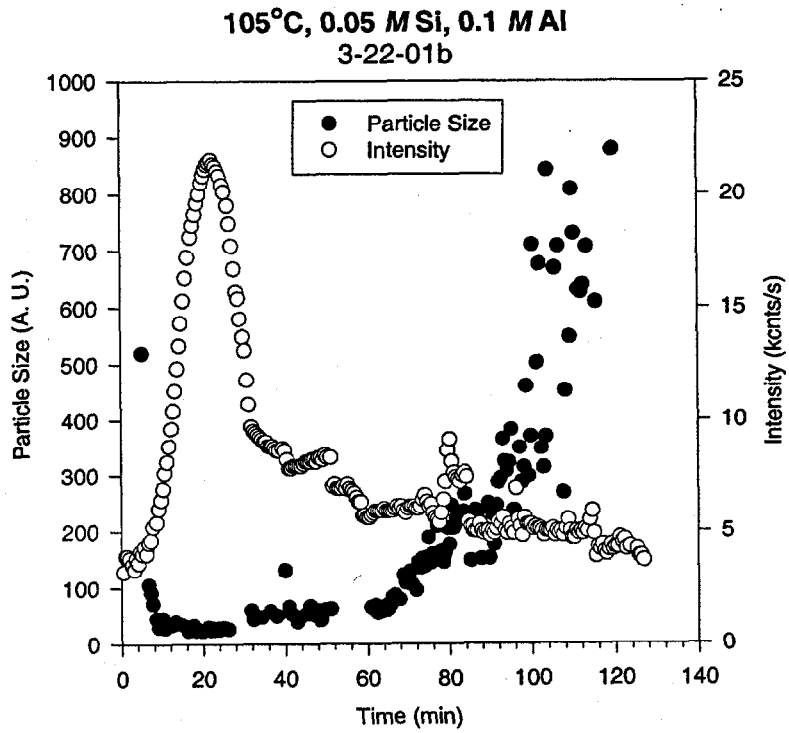
105°C, 0.05 M Si, 0.1 M Al
3-22-01b
Particle Size
Intensity
Particle Size (A. U.)
Intensity (kcnts/s)
Time (min)
0
100
200
300
400
500
600
700
800
900
1000
0
5
10
15
20
25
0
20
40
60
80
100
120
140

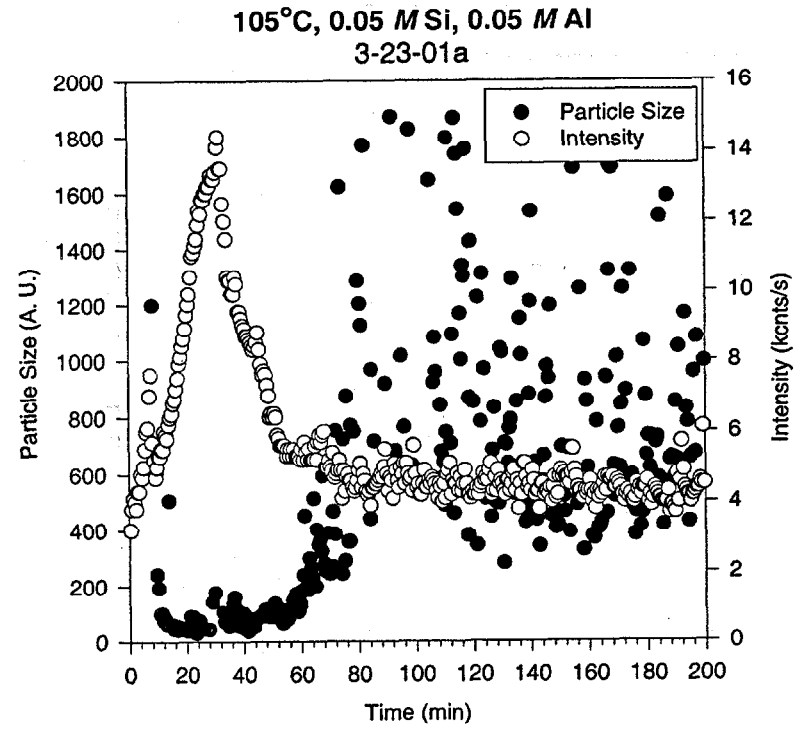
105°C, 0.05 M Si, 0.05 M Al
3-23-01a
Particle Size
Intensity
Particle Size (A. U.)
Intensity (kcnts/s)
Time (min)
0
200
400
600
800
1000
1200
1400
1600
1800
2000
0
2
4
6
8
10
12
14
16
0
20
40
60
80
100
120
140
160
180
200

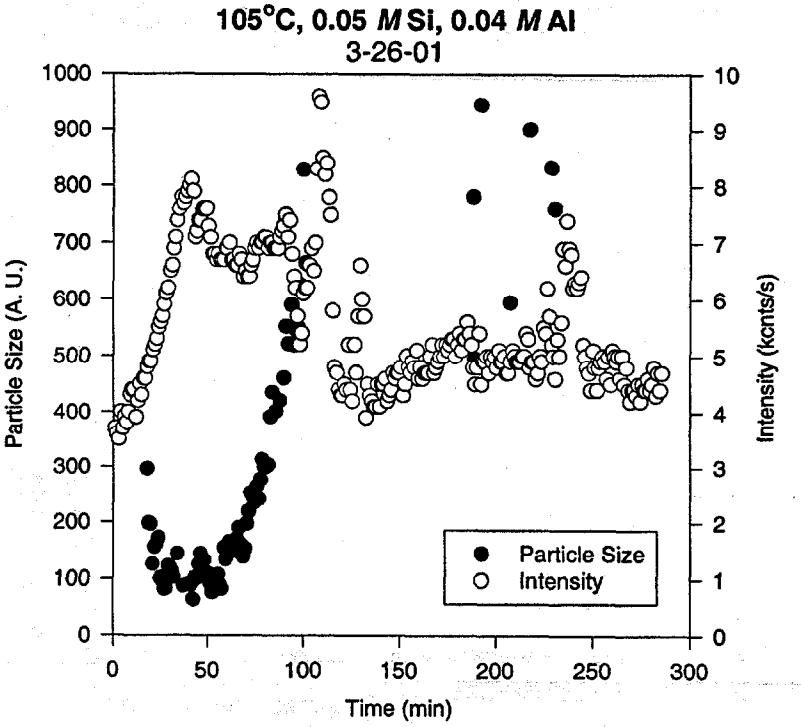
105°C, 0.05 M Si, 0.04 M Al
3-26-01
Particle Size (A. U.)
Intensity (kcnts/s)
Time (min)
Particle Size
Intensity
0
100
200
300
400
500
600
700
800
900
1000
0
1
2
3
4
5
6
7
8
9
10
0
50
100
150
200
250
300

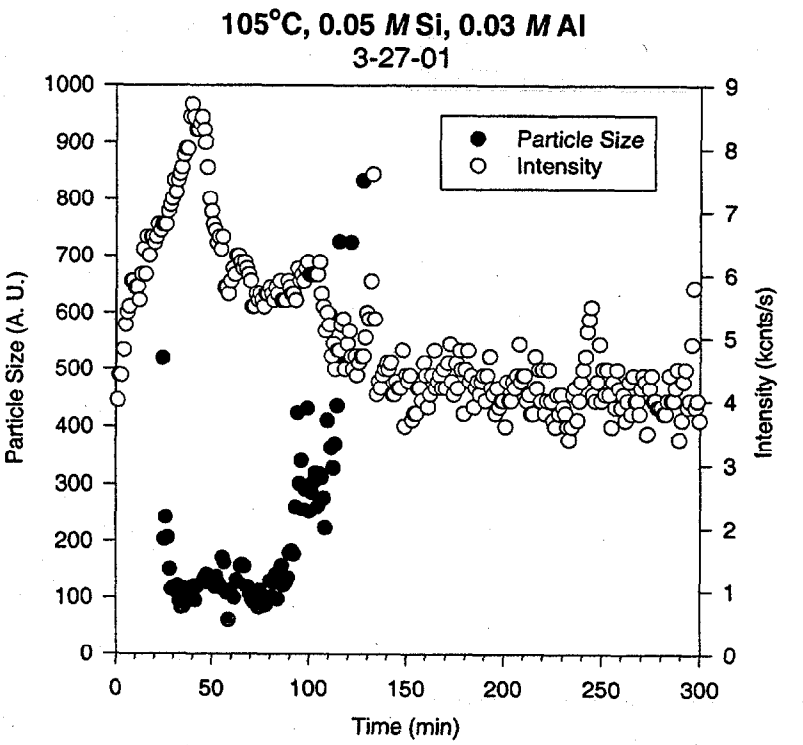
105°C, 0.05 M Si, 0.03 M Al
3-27-01
Particle Size (A. U.)
Intensity (kcnts/s)
Time (min)
Particle Size
Intensity
0
100
200
300
400
500
600
700
800
900
1000
0
1
2
3
4
5
6
7
8
9
0
50
100
150
200
250
300

VII. DLS Data at 107°C (near boiling point of 4 *M* NaOH solution)

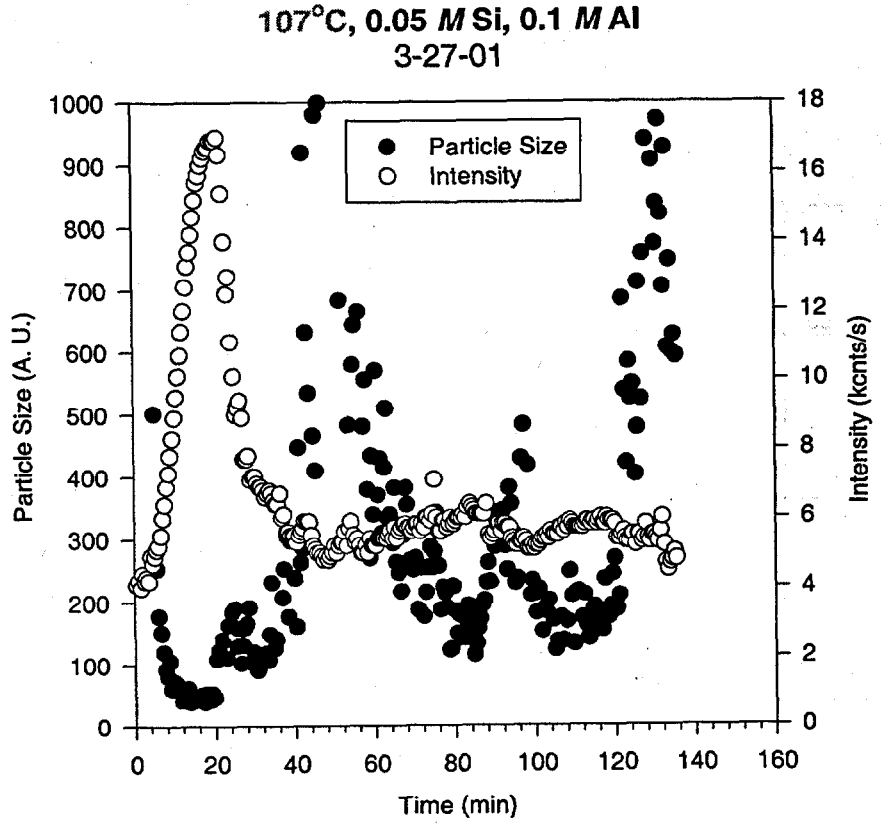

INTERNAL DISTRIBUTION

1. V. F. de Almeida
2–6. D. T. Bostick
7–11. D. W. DePaoli
12–16. M. Z. Hu
17. R. D. Hunt
18. R. T. Jubin
19. A. J. Mattus
20. C. P. McGinnis
21. L. E. McNeese
22. S. M. Robinson
23. C. Tsouris
24. J. S. Watson
25. C. Weber
26. T. D. Welch
27. Central Research Library
28. ORNL Laboratory Records—RC
29–30 ORNL Laboratory Records—OSTI

EXTERNAL DISTRIBUTION

31. C. S. Boley, Westinghouse Savannah River Company, Building 703-H, Room 137, Aiken, SC 29808

32. T. E. Britt, Westinghouse Savannah River Company, Building 703-H, Room 85, Aiken, SC 29808

33. L. D. Bustard, Sandia National Laboratories, P.O. Box 5800, MS: 0728, Albuquerque, NM 87185-5800

34. E. J. Cruz, U.S. Department of Energy, Richland Operations Office, P.O. Box 550, MSIN: H6-60, Richland, WA 99352

35. P. D. d'Entremont, Westinghouse Savannah River Company, Building 703-H, Room 97, Aiken, SC 29808

36. Kurt Gerdes, Tanks Focus Area Headquarters Program Lead, DOE Office of Science and Technology, 19901 Germantown Rd., 1154 Cloverleaf Building, Germantown, MD 20874-1290

37. P. W. Gibbons, Numatec Hanford Corporation, P.O. Box 1970, MS: H5-61, Richland, WA 99352

38. T. S. Gutmann, U.S. Department of Energy, Savannah River Operations Office, P.O. Box A, Aiken, SC 29802

39. E. W. Holtzscheiter, Westinghouse Savannah River Company, Savannah River Technology Center, Building 773-A, Room A-229, MS: 28, Aiken, SC 29802

40. J. O. Honeyman, Lockheed Martin Hanford Corporation, P.O. Box 1500, MS: G3-21, Richland, WA 99352

41. B. L. Lewis, Westinghouse Savannah River Company, Building 703-H, Room 99, Aiken, SC 29808

42. K. A. Lockie, U.S. Department of Energy, Idaho Operations Office, 750 DOE Place, MS: 1145, Idaho Falls, ID 83402

43. J. P. Morin, Westinghouse Savannah River Company, Savannah River Technology Center, Building

703-H, Aiken, SC 29808

44. J. R. Noble-Dial, U.S. Department of Energy, Oak Ridge Operations Office, P.O. Box 2001, Oak Ridge, TN 37830-8620

45. J. F. Ortaldo, Westinghouse Savannah River Company, Building 704-S, Room 13, Aiken SC 29808

46. Lynne Roeder-Smith, Tanks Focus Area Technical Team Communications, Pacific Northwest National Laboratory, P.O. Box 999, MSIN: K9-69, Richland, WA 99352

47. W. L. Tamosaitis, Savannah River Technology Center, Westinghouse Savannah River Company, Bldg.773-A, Room A-231, Aiken, SC 29808

48. M. T. Terry, Los Almos National Laboratory, P.O. Box 999, K9-69, Richland, WA 99352

49. T. R. Thomas, Lockheed Martin Idaho Technologies Company, P.O. Box 1625, MSIN: 3458, Idaho Falls, ID 83415-3423

50. J. H. Valentine, Bechtel BWXT Idaho, Inc., P.O. Box 1625, MS: 3211, Idaho Falls, ID 83415-3100

51. W. B. Van Pelt, Westinghouse Savannah River Company, Building 773-42A, Room 121, Aiken, SC 29808

52. W. R. Wilmarth, Westinghouse Savannah River Company, Building 773-42A, Room 153, Aiken, SC 29808

53. Tanks Focus Area Program Office, c/o T. Pietrok, U.S. Department of Energy, Richland Operations Office, P.O. Box 550, MS: K8-50, Richland, WA 99352

54. Tanks Focus Area Technical Team, c/o B. J. Williams, Pacific Northwest National Laboratory, P.O. Box 999, MSIN: K9-69, Richland, WA 99352